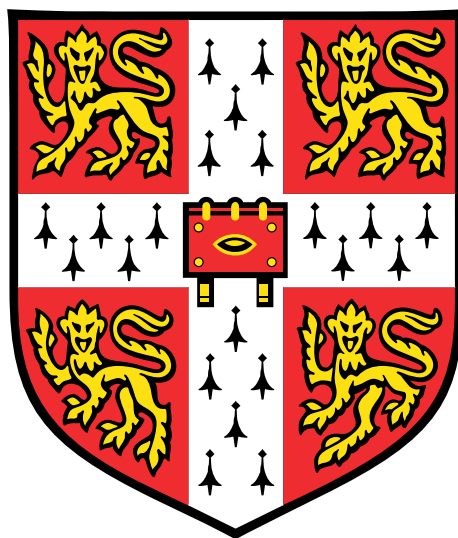


Spin Currents in Organic Semiconductors



Angela D. A. Wittmann

Department of Physics
University of Cambridge

This dissertation is submitted for the degree of
Doctor of Philosophy

Newnham College

September 2018

«C'est le temps que tu as perdu pour ta rose qui fait ta rose si importante.»

Antoine de Sait-Exupéry

Declaration

I hereby declare that this dissertation is the result of my own work and includes nothing which is the outcome of work done in collaboration except as specified in the text and Acknowledgements. It is not substantially the same as any that I have submitted, or, is being concurrently submitted for a degree or diploma or other qualification at the University of Cambridge or any other University or similar institution. I further state that no substantial part of my dissertation has already been submitted, or, is being concurrently submitted for any such degree, diploma or other qualification at the University of Cambridge or any other University or similar institution. Moreover, it does not exceed the prescribed word limit of 60'000 words including abstract, tables, footnotes and appendices.

Angela D. A. Wittmann
September 2018

Acknowledgements

There are many people without whom this work would not have been possible. I would, therefore, like to take this opportunity to express my sincere gratitude for their support, help and advice.

During the forming years of my undergraduate studies at ETH Zurich, Prof Klaus Ensslin first introduced me to the fascinating field of solid state physics in an introductory lecture. In addition to the insight into nanophysics he gave me, I am very grateful for the stimulating discussions on new developments in physics as well as career advice even after my time at ETH. One of the most fascinating lecture series I have attended was "Frontiers in Condensed Matter Physics" by Prof Bertram Batlogg. This series of seminars was the context in which I first learned about the work of Prof Henning Sirringhaus in the captivating field of organic semiconductors and also in which I became interested in spintronics.

I feel very privileged to have had the chance to pursue exactly my research interest and embark on a PhD project in organic spintronics under the supervision of Prof Henning Sirringhaus. I am greatly thankful for this opportunity and guidance throughout the project. Henning has taught me to conduct careful and thorough research, and I highly appreciate the freedom he is giving his students, which has allowed me to develop into a more independent researcher.

The inverse spin Nernst effect was initially proposed by Dr Joerg Wunderlich. He predominantly supervised the endeavours towards the observation of the effect. I am very grateful for numerous discussions in which my understanding of spintronics developed but also for teaching me about precise homodyne electrical detection during many late evenings of measurements.

I have greatly benefited from the training and mentoring by Prof Shun Watanabe at the beginning of my PhD. I am very grateful for having had the opportunity to visit him in the group of Prof Jun Takeya at the University of Tokyo in 2016, where the work on linewidth broadening started.

The continuation of this project in Cambridge was made possible with the help of Dr Guillaume Schweicher. His expertise in small molecules and active involvement in the project has been invaluable for the experiments on spin injection. His drive and passion for science have been inspirational.

Furthermore, I would like to thank Dr Deepak Venkateshvaran for continuous support and thorough training, especially on electron-beam lithography. Not only has he always been available for technical help but also been a wonderful mentor.

I would like to thank Dr Riccardo Di Pietro for sharing his understanding of charge transport in organic semiconductors and expertise in optics. His help with the optical spin injection experiments has been crucial. Moreover, I highly appreciate the help of Dr Keehoon Kang with the coplanar waveguide design, Prof Lang Jiang with the fabrication of the spin Seebeck devices and Sam Schott with the electron spin resonance setup. I am very grateful for the support in matters of fabrication and stability of organics of Dr Mark Nikolka, Dr Iyad Nasrallah and John Armitage.

I have enjoyed and benefited from interactions with members of the microelectronics group. I would especially like to thank Dr Andrew Ferguson and Dr Nicholas Lambert for their support and advice.

Many active collaborations have contributed to this work. I feel privileged to have been able to conduct this project as part of an ERC Synergy grant bringing together theoreticians, material chemists and experimental physicists, which has created an inspiring and interdisciplinary community. I am very thankful for numerous discussions and advice from all Synergy team members. In particular, I am very grateful for material synthesis and insight into organic chemistry provided by Cameron Jellett, Dr Mark Little and Adam Marks from the group of Prof Iain McCulloch. Furthermore, the theoretical support of the group of Prof Jairo Sinova has been very beneficial.

The collaborations have also reached outside the Synergy team. I would like to thank JProf Katharina Broch, Dr Jiri Novak, Dr Boseok Kang and Dr Hyoungju Ahn for structural characterisation and Vincent Lami and JProf Yana Vaynzof for ultraviolet photoelectron spectroscopy. Furthermore, I am thankful for high-quality Platinum films grown by Spencer Brennan in the group of Prof Russell Cowburn and thin YIG films grown by Dr Mario Amado in the group of Dr Jason Robinson and Dr Arpita Mitra in the group of Prof Bryan Hickey.

Construction of a new setup has been made possible by the very able help of Roger Beadle. He has taken time to discuss preliminary designs and to fabricate custom-made sample holders suitable for the specific needs of the experiments. Furthermore, the

assistance of Huw Prytherch with design and finishing the coplanar waveguide PCBs has been very helpful. I am also greatly indebted to Dr Radoslav Chakalov for his continuous help, support and advice.

I would like to acknowledge the financial support from the ERC Synergy grant, Hitachi Cambridge Laboratory and Newnham College for funding my studies and enabling me to pursue this project. Furthermore, I am very grateful for additional travel grants from IEEE Magnetics and IOP Magnetism for giving me the opportunity to deepen my understanding and broaden my view in the field of magnetism and to attend international conferences.

I have learned that we are nothing without the people we care about and who care about us and I am very grateful to have found such incredibly caring and supportive friends, who have made Cambridge feel like home. I would especially like to acknowledge Silvana Pesenti, Ran Huo, Spencer Brennan and Konrad Viebahn. I am greatly thankful for their support during the worst of times and am delighted for having shared the best of times. I highly appreciate that I have not only met brilliant colleagues in the lab but have also found wonderful friends including Kee, Iyad, Mark, Guillaume, Olia, Tudor, Sam, Deepak, John, Piotrek and Remington. I shall always cherish the happy memories from our skiing trips, climbing sessions and fun times in the cleanroom. Moreover, I would like to thank Cambyse Rouze and Joey for being very supportive company while writing this thesis.

Finally, I would like to express my heartfelt gratitude to Jakob Zwiener for his endless support, encouragement to chase my dreams and for being there for me, always. He has truly turned the last few years into the best time of my life. Last but not least, I would like to offer my special thanks to my parents. I highly appreciate that my father has nurtured my interest in scientific research and music from a young age. Furthermore, I am deeply grateful for having such an inspirational and empowering (little tiger) mother. I would not have been able to get as far as I have without their support and always pushing me to challenge myself.

Abstract

Organic semiconductors have recently been found to have a comparably large spin diffusion time and length. This makes them ideal candidates for spintronic devices. However, spin injection, transport and detection properties in organic materials have yet to be fully understood. This work studies spin injection from ferromagnets into organic semiconductors via spin pumping. Furthermore, work towards thermal spin injection, and detection is presented and discussed.

The first part of this thesis comprises the spin pumping experiments. Measuring linewidth broadening of the microwave absorption at ferromagnetic resonance due to increase in effective Gilbert damping by spin pumping from a ferromagnetic substrate into an adjacent non-magnetic semiconductor allows us to quantify the spin-mixing conductance. This technique is employed to demonstrate spin injection from a ferromagnetic metal, permalloy ($\text{Ni}_{81}\text{Fe}_{19}$), into organic small molecules and conjugated polymers as well as to quantify the spin injection efficiency. The results highlight the importance of structural properties of organic semiconductors at the interface to permalloy. Significant suppression of spin injection due to alkyl side-chains separating the core of the small molecules from the interface is exemplary for this finding. Furthermore, the spin-mixing conductance depends very sensitively on the charge carrier density within a certain range of doping level. This suggests a strong link between spin injection efficiency and spin concentration in the organic semiconductor at the interface to permalloy.

The second part of the thesis aims to explore spin caloritronic effects. We study spin injection into organic semiconductors by probing the spin Seebeck effect by making use of the inverse spin Hall effect for spin-to-charge conversion. Moreover, we present experimental work towards observation of a novel effect, the inverse spin Nernst effect, for thermal spin detection.

Contents

List of Figures	xvii
List of Tables	xix
Nomenclature	xxi
1 Introduction	1
2 Theoretical Background	7
2.1 Organic semiconductors	7
2.1.1 Charge transport in small molecules	8
2.1.2 Charge transport in polymers	9
2.2 Introduction to spin angular momentum	10
2.2.1 Spin	10
2.2.2 The concept of spin-current	10
2.3 Magnetisation dynamics and spin injection	13
2.3.1 Landau-Lifshitz-Gilbert equation and ferromagnetic resonance .	13
2.3.2 Magnetisation relaxation mechanisms	15
2.3.3 Thermal spin injection	20
2.3.4 Optical spin injection	23
2.4 Spin relaxation in non-magnetic materials	24
2.4.1 Spin relaxation and spin dephasing time	25
2.4.2 Elliott-Yafet mechanism	25
2.4.3 D'yakonov-Perel' mechanism	26
2.4.4 Bir-Aronov-Pikus mechanism	27
2.4.5 Hyperfine interaction	27
2.4.6 Spin relaxation in organic semiconductors	27
2.5 Spin detection via spin-to-charge conversion	28
2.5.1 Spin Hall effect	29

2.5.2	Electrically modulated inverse spin Hall effect	31
2.5.3	Proposal of thermal spin detection	32
3	Experimental Methods	33
3.1	Materials	33
3.1.1	Ferromagnetic materials	33
3.1.2	Organic semiconductors	35
3.1.3	Metallic spin sink materials	42
3.1.4	GaAs	42
3.2	Common sample fabrication techniques	42
3.2.1	Substrate cleaning	43
3.2.2	Photo-lithography	43
3.2.3	Electron-beam lithography on insulating substrates	44
3.3	Linewidth broadening experiments	44
3.3.1	Samples for linewidth broadening experiments	44
3.3.2	Electron spin resonance setup and linewidth broadening measurement	46
3.4	Thermal spin injection experiments	48
3.4.1	Spin Seebeck effect samples	48
3.4.2	Thermal spin injection setup and measurement	51
3.5	Thermal spin detection experiments	56
3.5.1	Inverse spin Nernst effect with spin injection via spin pumping	56
3.5.2	Inverse spin Nernst effect with optical spin injection	62
3.5.3	Electrically modulated inverse spin Hall effect	65
4	Quantifying Spin Injection by Measuring Linewidth Broadening	67
4.1	Optimisation of the linewidth broadening measurement	67
4.2	Characterisation of permalloy	68
4.3	Linewidth broadening in Py/Pt	69
4.4	Effects of solvents on permalloy	70
4.5	Conclusions	71
5	Spin Injection in Small Molecules	73
5.1	Spin injection into DNTT	73
5.2	Spin injection into three derivatives of DNTT	75
5.3	Effect of doping on spin injection in DNTT	80
5.4	Spin injection into derivatives of BTBT	81

5.5	Spin injection in small molecules with diradical character	82
5.6	Conclusions	85
6	Spin Injection in Polymers	87
6.1	Structural characterisation	87
6.2	Linewidth broadening experiments in polymers	88
6.3	Doping of P3HT	91
6.4	Thickness dependence of linewidth broadening	92
6.5	Conclusions	93
7	Thermal Spin Injection and Detection	95
7.1	Thermal spin injection via spin Seebeck effect	95
7.1.1	Initial measurements on YIG/Pt	95
7.1.2	Inorganic bilayer devices	98
7.1.3	Organic devices	99
7.1.4	Conclusions	100
7.2	Thermal spin detection via inverse spin Nernst effect	101
7.2.1	Towards inverse spin Nernst effect in YIG/Pt	101
7.2.2	Towards inverse spin Nernst effect in GaAs/Pt	105
7.2.3	Spin detection via electrically modulated inverse spin Hall effect	107
7.2.4	Conclusions	110
8	Conclusions and Outlook	111
Appendix A Temperature Dependence of Ferromagnetic Resonance in YIG		115
Appendix B GIWAXS Analysis of Polymer Films		117
References		119

List of Figures

1.1	Overview of materials in spintronics	2
1.2	Overview of spin injection into OSCs	3
2.1	Bonding orbitals of Ethene	8
2.2	Illustration of spin currents	11
2.3	Magnetisation dynamics	14
2.4	Spin pumping	18
2.5	Theory of SSE	21
2.6	Optical spin injection in GaAs	24
2.7	Spin relaxation mechanisms	26
2.8	Family of Hall effects	29
2.9	Mechanism of SHE	30
2.10	Electrically modulated ISHE	31
3.1	Chemical structure and packing of DNTT derivatives	35
3.2	Chemical structure and packing of BTBT derivatives	36
3.3	Chemical structure diradical molecules	37
3.4	Chemical structure polymers	40
3.5	Doping with F ₄ -TCNQ and GaAs substrate	41
3.6	LWB sample and ESR setup	45
3.7	Schematic of SSE device	50
3.8	Different SSE setups from literature	52
3.9	Schematic of SSE setup	53
3.10	CAD drawing of the SSE probe head	53
3.11	Images of SSE setup	54
3.12	Modifications to the SSE setup	55
3.13	Dose Test	57
3.14	ISNE device	58

3.15	CPW: from design to the actual PCB board	59
3.16	ISNE measurement configuration	61
3.17	Design of the optical ISNE sample	62
3.18	Schematic of optical setup	63
3.19	Electrically modulated ISNE	65
4.1	Angular dependence of FMR in Py	68
4.2	LWB in Py/Pt	69
5.1	LWB in DNTT	74
5.2	LWB in derivatives of DNTT	76
5.3	Structural characterisation of DNTT derivatives	77
5.4	Spin density maps of DNTT derivatives	78
5.5	Energetics of DNTT derivatives	79
5.6	LWB in doped DNTT	80
5.7	Spin density maps of BTBT derivatives	81
5.8	LWB in small molecules with different diradical character	83
5.9	XRR data of DX-IDF and DX-IDT	84
6.1	GIWAXS of P3HT, d-P3HT and IDT-BT	88
6.2	LWB in P3HT, d-P3HT, P3EHS and IDT-BT	89
6.3	LWB in doped P3HT	91
6.4	Thickness dependence of LWB in Polymers	93
7.1	SSE measurements on YIG/Pt	96
7.2	Comparison of SSE signal of materials with different spin Hall angle	98
7.3	SSE in YIG/P3HT/Pt	99
7.4	SSE in YIG/ delaminated (P3HT/Pt)	100
7.5	SSE signal in small out-of-plane magnetic fields due to high in-plane anisotropy of YIG	102
7.6	SNE measurements	103
7.7	GaAs Photodiode	105
7.8	Optical ISNE measurements	106
7.9	Current induced ISHE measurements	108
8.1	LWB in P3EHT and MASnI_3	112
A.1	Temperature dependence of FMR in YIG	116

List of Tables

3.1	Magnetic properties of permalloy, cobalt and iron at FMR	33
3.2	Spin Hall angle of several metals	42
3.3	Periodicity and phase shift of circular and linear component of the signal from the optical signal	65
4.1	Linewidth of permalloy absorption at different conversion times t_c . . .	68
4.2	Change in linewidth due to solvent treatment of thin permalloy films .	71
5.1	Change in linewidth, spin-mixing conductance and estimate of spin diffusion length for the three derivatives of DNTT	75
B.1	Summary of crystallographic information of three polymers	118

Nomenclature

Acronyms / Abbreviations

AC	Alternating current
AHE	Anomalous Hall effect
CPW	Coplanar waveguide
DC	Direct current
ERC	European Research Council
ESR	Electron spin resonance
FM	Ferromagnet
FMI	Ferromagnetic insulator
FMR	Ferromagnetic resonance
GIWAXS	Grazing-incidence wide-angle X-ray scattering
GIXD	Grazing-incidence X-ray diffraction
HFI	Hyperfine interaction
hh	Heavy holes
HOMO	Highest occupied molecular orbital
ICT	Information and communication technology
ISHE	Inverse spin Hall effect
ISNE	Inverse spin Nernst effect

lh	Light holes
LL	Landau-Lifshitz
LLG	Landau-Lifshitz-Gilbert
LPE	Liquid-phase epitaxy
LUMO	Lowest unoccupied molecular orbital
LWB	Linewidth broadening
NM	Non-magnetic material
OSC	Organic semiconductor
PCB	Printed circuit board
PEM	Photoelastic modulator
SHE	Spin Hall effect
SNE	Spin Nernst effect
SOC	Spin-orbit coupling
SSE	Spin Seebeck effect
UPS	Ultraviolet photoelectron spectroscopy
VRH	Variable range hopping
XRR	X-ray reflectivity

Materials

ACN	Acetonitrile
BTBT	[1]Benzothieno[3,2-b]benzothiophene
Co	Cobalt
Cr	Chromium
CYTOP	Amorphous perfluoropolymer, commonly used as dielectric
DFB1	Diindeno-fused bischrysene

DIADX	Di-indeno-anthracene-di-xylene
diF TES ADT	2,8-Difluoro-5,11-bis(triethylsilylethynyl)anthradithiophene
DNTT	Dinaphtho[2,3-b:2',3'-f]thieno[3,2-b]thiophene
DX-IDF	Di-xylene-indenofluorene
F ₄ -TCNQ	2,3,5,6-tetrafluoro-7,7,8,8-tetracyanoquinodimethane
Fe	Iron
GaAs	Gallium arsenide
GGG	Gadolinium gallium garnet
IDT-BT	Indacenodithio-phene–benzothiadiazole
IPA	Isopropanol
LSMO	La _{0.7} Sr _{0.3} MnO ₃
MA	Methylammonium
OTS	Octadecyltrichlorosilane
P3EHT	Poly(3-(2-ethyl)hexylthiophene)
P3HT	Poly(3-hexylthiophene)
PBTTT	Poly(2,5-bis(3-alkylthiophene-2-yl) thieno[3,2-b]thiophene)
Pt	Platinum
Py	Permalloy, Ni ₈₀ Fe ₂₀
THF	Tetrahydrofuran
TIPS pentacene	6,13-Bis(triisopropylsilylethynyl)pentacene
YIG	Yttrium iron garnet

Physical Variables

α	Gilbert damping parameter
α_0	Intrinsic Gilbert damping of a FM

ΔH	Linewidth of FMR absorption
$\Delta\alpha$	Increase in Gilbert damping due to spin pumping
$\delta\Delta H$	Change in linewidth due to spin pumping
γ	Gyromagnetic ratio
\mathbf{H}	Magnetic field
\mathbf{M}	Magnetisation
\mathcal{H}	Hamiltonian
ω	Microwave frequency
E_g	Bandgap
$g^{\uparrow\downarrow}$	Spin-mixing conductance
M_s	Saturation magnetisation
t_{FM}	Thickness of the FM
y	Diradical character
T_1	Spin relaxation time
T_2	Spin decoherence time

Chapter 1

Introduction

Information and communication technology (ICT) is a rapidly progressing and expanding field today. Its challenges and potential have attracted considerable attention over the last few years, especially in R&D. As a result, over 20% of researchers were working in the ICT sector in the European Union in 2015 [1]. Currently, most technology is based on a binary system, where either the electronic state of a semiconductor device or the relative orientation of ferromagnets (FM) represent the "on" and "off" state. Hard disk drives and magnetic random access memories are prominent examples of applications we use in our everyday life, which are based on this working principle. However, the development of charge-based devices is fast approaching its limits according to the Moore's law-driven International Technology Roadmap for Semiconductors [2]. Spintronics is among the most frequently mentioned promising alternatives. The rapidly developing field is bringing together relativistic quantum physics, materials science and nanoelectronics. Its paradigm changing nature lies in encoding information in all three fundamental properties of electrons, mass, charge and spin. Adding spin to the game is much more than merely completing the triangle. In contrast to the scalar quantities, mass and charge, spin is a vector. The directionality brings in unique and novel phenomena and functionalities, which are intrinsically non-volatile and robust against charge perturbations.

Research in spintronics has predominantly focused on metals and inorganic semiconductors, where charge transport is well described by band-transport theory. In the past few years, there has been a growing interest in investigating spin properties in organic materials. From a fundamental point of view, the attraction lies in understanding the underlying mechanisms and coupling between charge and spin, as charge transport is mediated by inherently different mechanisms. Due to disorder and thermal inter-

and intramolecular vibrations, the picture of Bloch-waves travelling through a periodic crystal does not apply for organic semiconductors (OSCs). Hence, conventional band-transport theory breaks down and is replaced with the concept of hopping transport, where localised charge carriers move in molecular orbitals.

Charge transport properties have been studied extensively and have led to OSC-based applications in many technological sectors including field-effect transistors [3], organic light emitting diodes [4], photovoltaics [5] and thermoelectrics [6]. The benefits of OSCs over their inorganic counterparts include flexibility, large-area solution-processability and the vast parameter space for tuning properties by molecular design.

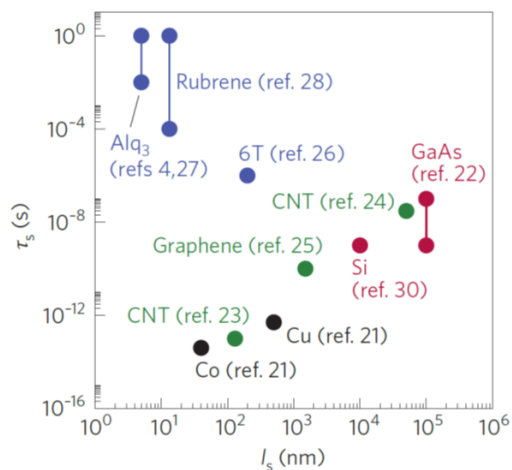


Fig. 1.1 Map of spin-diffusion length (l_s) and spin-diffusion time (τ_s) of different materials used in spintronics. Organic materials are shown in blue (reproduced from [7]).

Owing to the composition of light chemical elements of OSCs, spin relaxation is expected to be rather inefficient due to small spin-orbit coupling. This implies a long spin lifetime and diffusion length, which is very attractive for spintronic devices. A map of spin-diffusion length l_s versus spin-diffusion time τ_s of various materials is shown in figure 1.1. The OSCs included in this graph (blue circles) indeed show a comparably long spin-diffusion time. However, the spin-diffusion length is significantly shorter than in common inorganic semiconductors such as Silicon (Si) and Gallium Arsenide (GaAs, shown in red). This suggests that the spin diffusion length might be limited by the low mobility of charge carriers in organic materials.

The first experiments probing spin properties in organics include the observation of organic magnetoresistance [8] and reports of spin transport in OSCs in spin-valve structures [9, 10]. However, recent findings suggest, that the interpretation of the latter experimental results is not straightforward [11]. In a conventional spin-valve structure, the OSC is sandwiched between two ferromagnetic contacts and the spin-signal is given by the change in resistance across the FM/OSC/FM junction depending on the relative orientation of the ferromagnetic electrodes. A commonly used FM in organic spin-valves is $\text{La}_{0.7}\text{Sr}_{0.3}\text{MnO}_3$ (LSMO). However, the complex magnetic anisotropy of LSMO gives rise to the so-called tunnelling anisotropic magnetoresistance. This effect manifests itself in magnetic switching characteristics, which are analogous to

the signal measured in LSMO/OSC/FM spin-valves, in comparable device structures with only one LSMO electrode and a normal metal contact. Therefore, careful control measurements are necessary for observing a true spin-valve signal.

Moreover, spin injection and transport in OSCs have been studied in trilayer architectures [12]. In these experiments, a pure spin-current was injected in a conjugated polymer from a ferromagnet by spin pumping and detected in a heavy metal layer via the inverse spin Hall effect.

Recent developments in ICT have brought awareness to the crucial importance of interfacial properties for nano-scale devices. Owing to the unique tunability of organic materials, studying spin effects at the interface brings forth great potential [7, 13]. A powerful example of these *spinterface* effects is a recent report of magnetism induced in intrinsically non-magnetic materials by molecular coupling [14].

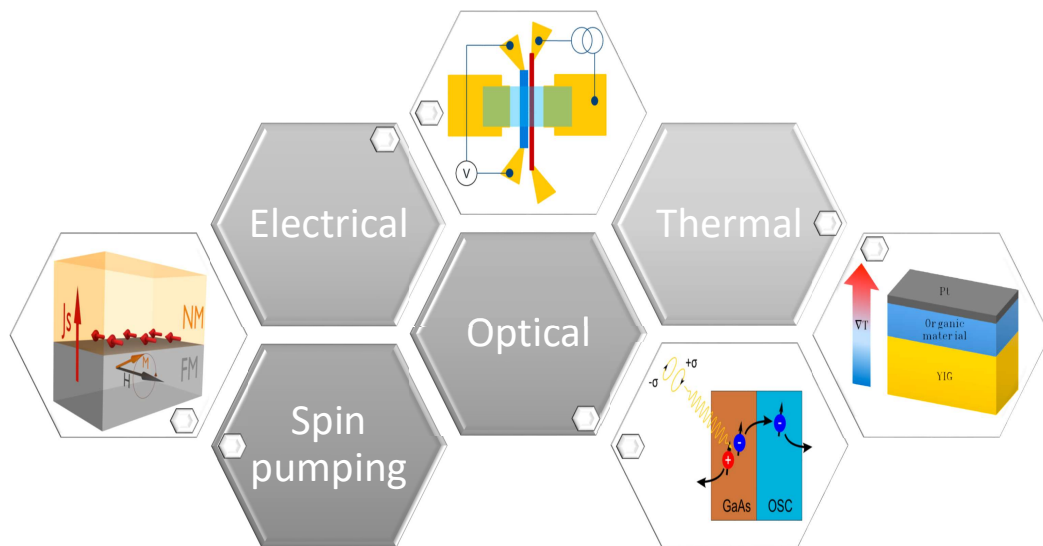


Fig. 1.2 Overview of different techniques for spin injection into OSCs. The insets show schematics of the sample structures for electrical, optical and thermal spin injection and spin pumping.

This work is part of an ERC Synergy project on organic spintronics bringing together device physicists at the University of Cambridge and Hitachi Cambridge Laboratory from the groups of Prof Henning Sirringhaus and Dr Joerg Wunderlich, theoreticians at the Johannes Gutenberg Universität Mainz, Germany, from the group of Prof Jairo Sinova and materials chemists at Imperial College London from the group

of Prof Iain McCulloch. The aim is to approach the open questions on spin injection, transport and detection in OSCs in a broad and interdisciplinary manner.

In order to get a deeper and more general insight into spin injection in OSCs, the project explores four different mechanisms, electrical, optical and thermal spin injection and spin pumping. An overview of the mechanisms including schematics of the device structures is shown in figure 1.2.

Dr Deepak Venkateshvaran has studied electrical spin injection in various spin-valve structures and material systems [15]. The experimental results imply that current spreading effects are dominant. Furthermore, the measurements are limited by $1/f$ -noise from the OSC, making it challenging to detect a spin signal in conventionally used architectures. Based on these results, we have shifted our focus on methods of spin injection, which are not as heavily impeded by the large conductivity mismatch. Dr Riccardo Di Pietro is investigating optical spin injection from GaAs into an n -type polymer. For this, the spins are oriented in GaAs with circularly polarised light, accelerated into the OSCs by applying a bias voltage and measured in a heavy metal layer using an anomalous Hall effect like detection.

Following on from the initial work on spin pumping in trilayer architectures lead by Dr Shun Watanabe [12], Shu-Jen Wang and Dr D. Venkateshvaran have studied spin pumping from a ferromagnetic metal into different polymers and inverse spin Hall detection in a heavy metal stripe in a lateral structure. In addition to the benefit from well-controlled interfaces, the lateral design is also less prone to artefacts from pinholes or thermal effects for example. The extracted spin diffusion length for a conjugated polymer (P3HT) exceeds $1 \mu\text{m}$ [15], bringing us closer to the top right corner of the map in figure 1.1. Furthermore, they observed a strong dependence of the spin signal on the doping level of the polymer, implying a strong link between charge transport and spin properties.

So far, spin detection in organic devices has always relied on a secondary effect or even a separate inorganic detection layer introducing another interface. The aim of the first part of this project is to go back to the most basic and simple bilayer structure and directly measure the spin injection efficiency from a ferromagnetic metal into OSCs. For this, we extract the linewidth broadening of the microwave absorption due to spin pumping at ferromagnetic resonance. We demonstrate that this effect is a direct manifestation of spin injection under well-controlled circumstances and allows to extract the spin-mixing conductance. This technique allows us to study the material, structure and charge density dependence of spin injection directly.

The second part of this work aims to explore spin caloritronics in OSCs. The generality of the concept of spin-mixing conductance implies the equivalence of spin injection by spin pumping and by the spin Seebeck effect (thermal spin injection) [16]. As a consequence, successful spin pumping experiments suggest that thermal spin injection might be efficient in OSCs as well. Therefore, we built a measurement setup for spin Seebeck effect experiments and investigated thermal spin injection in device structures similar to the trilayer spin pumping architecture.

The inverse spin Hall effect is the most commonly employed mechanism for spin detection via spin-to-charge conversion [17]. However, the spin Hall angle, which is a measure of the efficiency of spin-to-charge interconversion, has recently been determined to be very small in OSCs due to the small spin-orbit coupling [18]. As a result, inverse spin Hall effect measurements in organics are very challenging. Based on the exceptional thermoelectric properties of OSCs, we were inspired to explore thermal spin detection. Dr Joerg Wunderlich proposed the idea of accelerating an out-of-plane spin accumulation with a thermal gradient. Spin-dependent scattering then results in a transverse electrical voltage, which allows detecting the spin accumulation. The inverse effect, the spin Nernst effect, which describes the generation of a spin accumulation due to a thermal gradient, has recently been experimentally observed [19]. This has encouraged our experimental endeavours towards observation of the inverse spin Nernst effect, which are presented in the final part of this work.

Chapter 2

Theoretical Background

In this chapter, we shall visit the fundamental concepts underlying the work of this thesis. The first section serves as an introduction to organic semiconductors. In organic materials, charge transport does not follow the same mechanisms as for conventional inorganic materials. This also implies exciting and novel properties of spin currents in organic semiconductors, which had not yet been studied thoroughly. After a brief introduction to spin angular momentum and spin currents, we shall present the mechanisms of spin injection, relaxation and detection used in this work with a focus on spin pumping at ferromagnetic resonance.

2.1 Organic semiconductors

Organic semiconductors (OSCs) are subclassified into two categories, small molecules and polymers. They are constructed from organic, carbon-based materials, and hence consist mainly of carbon, hydrogen and optionally of heteroatoms, such as oxygen, nitrogen and sulfur.

The first step towards understanding electronic properties of the OSCs is to examine carbon-carbon bonds. For this, let us consider the most fundamental molecule, Ethene, which consists of two carbon atoms connected with a double bond. Neutral atomic carbon has four valence electrons in a $2s^2 2p^2$ configuration [20]. When forming a double bond, however, it is energetically favourable to form three sp^2 hybridised orbitals in-plane and only one remaining p_z orbital out-of-plane (see illustration in figure 2.1a). The sp^2 orbitals form a strongly directional and highly localised σ -bond, which ensures stability in carbon chains, sheets and branched structures. The anti-bonding orbital σ^* lies at much higher energy and is therefore not occupied in the ground state. The edge overlap of the p_z orbitals forms delocalised bonding π and anti-bonding π^*

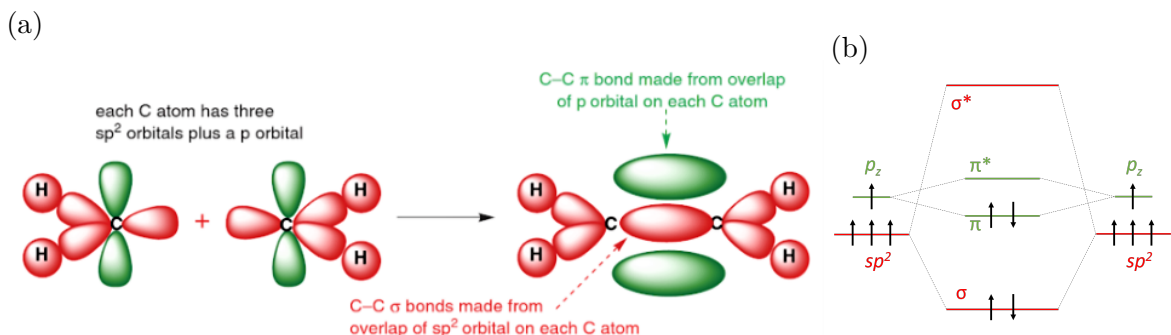


Fig. 2.1 (a) Illustration of molecular orbitals of two carbon atoms with three sp^2 orbitals and one p_z orbital each (left) and the bonding orbitals for a carbon-carbon double bond (right) in Ethene (reproduced from [20]). (b) Energy levels of bonding orbitals.

orbitals. The difference in energy between π and π^* is smaller compared to σ/σ^* ; it is however again energetically favourable to only occupy the bonding π orbital. The energy gap E_g between the highest occupied molecular orbital (HOMO) and the lowest unoccupied molecular orbital (LUMO) is akin to the band-gap in conventional inorganic semiconductors.

When we extend the length of the carbon chain, the π/π^* orbitals planarize the molecule and allow delocalisation over many carbon atoms. This process is known as *conjugation*. In OSCs, charge transport occurs through these delocalised π -orbitals, which are approximated by Hückel theory [21]. When the conjugation length is increased, the ensemble of hybrid states is broadened into quasi-continuous bands, and the energy gap E_g decreases. Peierls instability, however, ensures a finite gap even in infinitely long chains due to fundamental electronic instability in low dimensional systems.

When the p_z orbitals of neighbouring molecules overlap, the delocalisation can expand into several layers of molecules. This so-called $\pi - \pi$ stacking highlights the importance of structural properties of OSCs for charge transport.

2.1.1 Charge transport in small molecules

In the solid phase, organic small molecules arrange in a periodic crystal structure. Hence, following the theory developed for inorganic semiconductors, induced charges can be viewed as Bloch waves suggesting band-like charge transport. However, in contrast to inorganic semiconductors, the organic crystals are not static but fluctuate on the same timescale as carrier motion.

The model of Fratini *et al.* includes the modulation of states due to thermal motion of the molecules [22]. The interaction between the molecules is mediated by weak Van der

Waals forces, allowing large intermolecular vibrations. Assuming a narrow, band-like intermolecular π -orbital, these distortions in the lattice act as a source of dynamic disorder. As a consequence, the electronic wavefunction is no longer given by a periodic Bloch-state, but rather by localised states that are fluctuating on the timescale of the intermolecular vibrations in the THz range. Hence, due to the intrinsically low mobility in OSCs, the basic assumptions underlying band transport theory break down, and we cannot describe this phenomenon using semi-classical Boltzmann theory.

The alternative transport mechanism mentioned above is known as *transient localisation* and has been shown to agree well with experimental results in optical spectroscopy, field-effect transistor and Hall effect measurements [23, 24, 25, 26].

2.1.2 Charge transport in polymers

Polymers exhibit varying degrees of crystallinity, ranging from amorphous to semi-crystalline. As a consequence, the picture of band-like charge transport completely breaks down.

The delocalisation of the charges in the π -orbitals is limited due to spatial disorder, defects and impurities in the organic materials and lattice vibrations forming traps, which confine and localise the charge carriers. The localisation of charges due to static disorder and presence of strong electron-phonon interaction promotes formation of polarons, quasi-particles that mediate charge transport in OSCs [27]. The charge carriers travel through the material via hopping from one localised site to another site. This hopping transport is thermally activated, implying an increase in mobility with increasing temperature. This is in contrast to transport in conventional inorganic semiconductors, where charge transport in the band is impeded by phonons, and therefore the mobility decreases with increasing temperature.

There are several approaches to describe the thermally activated mechanism of charge transport in OSCs including the Variable Range Hopping (VRH) model by Vissenberg and Matters [28] and an adaptation of the VRH model for two dimensional charge transport in field-effect transistors by Brondijk *et al.* [29]. Furthermore, the model by Fornari *et al.* [30] describes the importance of structural disorder and electron-phonon coupling for mobility of conjugated polymers.

2.2 Introduction to spin angular momentum

Spintronics is a broad field in solid state physics exploring the properties of the spin degrees of freedom in condensed matter. It ranges from manipulation and control of single localised spin to studying spin transport and spin dynamics in macroscale systems [31]. The theoretical concepts of the latter shall be introduced in the following.

2.2.1 Spin

Spin is an intrinsic angular momentum, which is a purely quantum mechanical property [32, 33]. It is described by a Hermitian operator $\hat{\mathbf{S}} = (\hat{S}_x, \hat{S}_y, \hat{S}_z)$. The components satisfy the angular momentum commutation relations:

$$[\hat{S}_i, \hat{S}_j] = i\hbar\epsilon_{ijk}\hat{S}_k. \quad (2.1)$$

In the case of spin-1/2 particles, such as electrons, the spin operators are given by the Pauli matrices, $\hat{\mathbf{S}} = \hbar/2\boldsymbol{\sigma}$, which form the fundamental representation of the special unitary group SU(2). Analogously to orbital angular momentum, the eigenvalues of \hat{S}_z for a spin- s particle are given by $m_s = -\hbar s, -\hbar(s+1), \dots, \hbar(s-1), \hbar s$, where s has to be either an integer or half-integer.

2.2.2 The concept of spin-current

A conventional charge current describes the flow of charge by charge carriers such as electrons or holes. Analogously, a spin-current can be defined as a flow of angular momentum. Similarly to charge current, which is defined in terms of the charge conservation law, the spin-current density tensor $\overline{\overline{\mathbf{j}}}_s$ can be introduced in the context of spin angular momentum conservation. We note that $\overline{\overline{\mathbf{j}}}_s$ is not a vector but a second-rank tensor as the spin current has two orientations, the spatial flowing orientation and the spin orientation. In general, spin angular momentum is not conserved due to spin relaxation. Hence, denoting the local magnetisation with \mathbf{M} , the modified continuity equation reads

$$\frac{d\mathbf{M}}{dt} = -\text{div}\overline{\overline{\mathbf{j}}}_s + \mathbf{T}. \quad (2.2)$$

The additional term \mathbf{T} represents the change in angular momentum due to spin relaxation or spin generation.

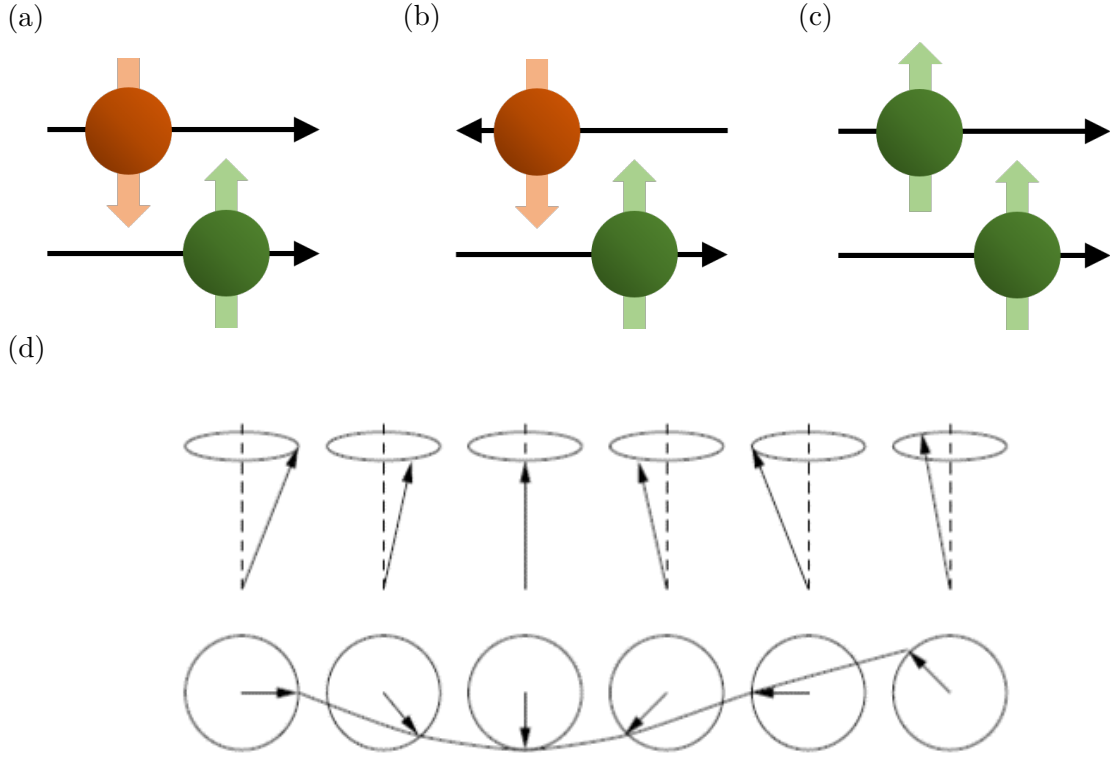


Fig. 2.2 Illustration of (a) a charge current, (b) a pure spin current and (c) a spin-polarised current. Charge carriers are marked by coloured spheres. The direction of the spin is indicated by the coloured arrows. The black arrows show the propagation direction of the charge carriers. (d) Shows an illustration of low-energy magnon spin-wave excitations from the spin-polarised ground state (taken from [34]).

In order to get an intuitive understanding of spin currents, let us first consider a simplified two-channel model system in which conduction electrons are charge carriers, and there is no spin relaxation. Let J_c and J_s denote charge and spin-current respectively and J_\uparrow (J_\downarrow) particle-current of spin-up (spin-down) electrons. Then, a charge current can be written as a sum of spin-up and spin-down electron currents

$$J_c = -e(J_\uparrow + J_\downarrow), \quad (2.3)$$

where $-e$ denotes the elementary charge of an electron. An illustration of this charge current in the spin-dependent two-channel model is shown in figure 2.2a. The spin magnetic moment of electrons is given by $\pm\hbar/2$. Similarly, a pure spin-current, a flow of spin-angular momentum without net charge current is therefore given by

$$J_s = -\frac{\hbar}{2}(J_\uparrow - J_\downarrow), \quad (2.4)$$

which is illustrated in figure 2.2b. In the case of a spin-polarised current (figure 2.2c) the majority of electrons are spin-polarised such that the charge current is accompanied by a spin-current.

Moreover, a spin-current does not necessarily need to be coupled to charge carriers, but can also be carried by spin-waves, known as magnons. This is most important for spin transport in ferromagnetic insulators, where no intrinsic charge carriers are present. Spin waves are most straightforwardly described in the one-dimensional Heisenberg model. The Hamiltonian of exchange interaction in a spin chain with N spins can be written

$$\mathcal{H} = -J \sum_m \hat{\mathbf{S}}_m \cdot \hat{\mathbf{S}}_{m+1}, \quad (2.5)$$

where we require the exchange coefficient $J > 0$ and $\hat{\mathbf{S}}_m$ denotes the quantum mechanical spin operator at lattice site m [34]. Thus, it is energetically favourable for neighbouring spins to be aligned in the same direction. The ground state of this system is highly degenerate due to a global rotation symmetry. One ground state is given by a chain of spins which are all aligned in the z -direction for example. Formally, this can be written as $\otimes_m |S_m\rangle$ with $\hat{S}_m^z |S_m\rangle = S |S_m\rangle$. The Goldstone theorem predicts a gapless excitation from the ground state due to the global symmetry. In fact, these spin-wave excitations from the spin polarised ground state are magnons. In a semi-classical picture, where $S \gg 1$, the spin fluctuations are negligibly small, and the rotation of the spins around their ground state position becomes similar to the rotation of a classical magnetic moment. An illustration of these spin-waves is shown in figure 2.2d. Making use of this approximation and the Holstein-Primakoff transformation, the Hamiltonian can be rewritten as

$$\mathcal{H} = -JNS^2 + \sum_k^{B.Z.} \omega_k a_k^\dagger a_k + \mathcal{O}(S^0). \quad (2.6)$$

The dispersion relation is given by $\omega_k = 2JS(1 - \cos ka)$, where a denotes the lattice constant. It is of course considerably more complicated in real ferromagnetic systems. However, the basic semi-classical idea of precessing magnetic moments still holds and gives an intuitive understanding of magnons.

2.3 Magnetisation dynamics and spin injection

2.3.1 Landau-Lifshitz-Gilbert equation and ferromagnetic resonance

As seen in the previous section, the exchange interaction between spins can be described with Heisenberg's Hamiltonian shown in equation 2.6. This expression can be generalised to three-dimensional lattices by allowing summation over all combinations of nearest neighbouring spins. The energy is minimised when the spins align parallel. When the reduction in energy due to alignment is larger than the thermal fluctuations, a ferromagnetic state can appear, where the matter exhibits finite magnetisation even in the absence of an external magnetic field. The alignment of the magnetisation \mathbf{M} to the external magnetic field \mathbf{H} due to Zeeman interaction can be described with the Hamiltonian

$$\mathcal{H} = -\mathbf{M} \cdot \mathbf{H}_{eff}, \quad (2.7)$$

where \mathbf{H}_{eff} denotes the effective magnetic field and \mathbf{M} satisfies the commutation relation of angular momentum mentioned in equation 2.1. The dynamics of the magnetisation \mathbf{M} are given by the Heisenberg equation of motion. Using the commutation relations, we obtain the Landau-Lifshitz (LL) equation

$$\frac{d\mathbf{M}}{dt} = -\gamma \mathbf{M} \times \mathbf{H}_{eff}, \quad (2.8)$$

where γ denotes the gyromagnetic ratio [35]. This describes the dynamics of an isolated spin undergoing constant precession around the effective magnetic field. Figure 2.3a shows an illustration of the precessional motion of \mathbf{M} . Due to interaction of the spin with the environment, however, the spin can relax towards the precession axis \mathbf{H}_{eff} minimising the energy of the system. This relaxation is taken into consideration by adding the Gilbert damping term to the aforementioned LL equation [36]. The equation of motion is finally given by the Landau-Lifshitz-Gilbert (LLG) equation

$$\frac{d\mathbf{M}}{dt} = -\gamma \mathbf{M} \times \mathbf{H}_{eff} + \frac{\alpha}{M_s} \mathbf{M} \times \frac{d\mathbf{M}}{dt}, \quad (2.9)$$

where α denotes the Gilbert damping parameter and M_s the saturation magnetisation. Figure 2.3b shows an illustration of the interplay of the different components giving rise to a damped precessing system. The relaxation mechanism and the origin of the

phenomenological Gilbert damping parameter α shall be discussed in the following section 2.3.2.

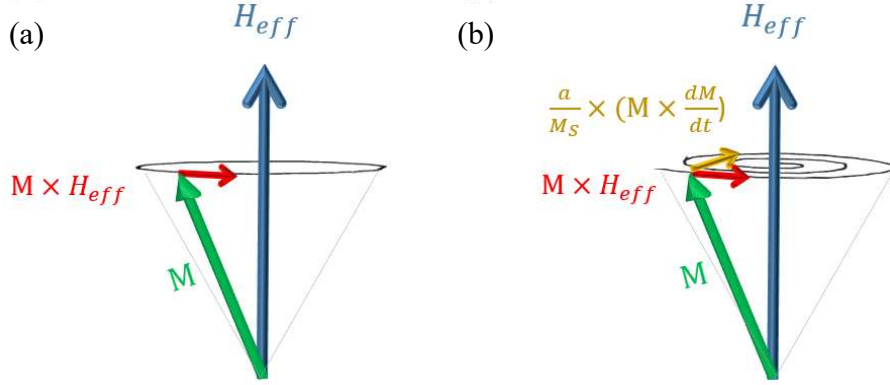


Fig. 2.3 (a) Illustration of precession of magnetisation around the effective magnetic field according to the LL equation. (b) Precessional motion including relaxation due to the Gilbert damping term following the LLG equation (illustrations reproduced from [37]).

This coherent precession of magnetisation in a ferromagnetic film can be driven with an external AC magnetic field at microwave frequency. The resonance condition for this ferromagnetic resonance (FMR) is given by the Kittel formula

$$\frac{\omega}{\gamma} = \sqrt{H_{FMR}(H_{FMR} + 4\pi M_{eff})}, \quad (2.10)$$

where ω denotes the frequency of the microwave magnetic field, H_{FMR} is the external DC magnetic field at resonance and M_{eff} is the effective magnetisation [38]. When the external magnetic field is at an out-of-plane angle of θ_H , the equation generalises to

$$\frac{\omega}{\gamma} = (H_{FMR}\cos(\theta_M - \theta_H) - 4\pi M_s\cos 2\theta_M)(H_{FMR}\cos(\theta_M - \theta_H) - 4\pi M_s\cos^2\theta_M), \quad (2.11)$$

where θ_M denotes the angle of the magnetisation, which can differ from the external magnetic field due to magnetic anisotropy.

The lineshape of the microwave absorption as a function of magnetic field H at a fixed frequency is given by a linear combination of a symmetric (S) and anti-

symmetric (A) Lorentzian [39]:

$$L = S \frac{\Delta H^2}{(H - H_{FMR})^2 + \Delta H^2} + A \frac{-2\Delta H(H - H_{FMR})}{(H - H_{FMR})^2 + \Delta H^2}. \quad (2.12)$$

The FMR linewidth ΔH (full width at half maximum) can be expressed in terms of the Gilbert damping parameter as [40, 41]

$$\Delta H = \Delta H_{ih} + \frac{\omega}{\gamma} \alpha. \quad (2.13)$$

The frequency independent term ΔH_{ih} is commonly called *inhomogeneous broadening* and can be related to the variation in the magnitude of the anisotropy throughout the film. In this work we shall presume that ΔH_{ih} depends only on the FM film and is not significantly altered by deposition of any NM on the FM.

In FM/NM bilayers, the Gilbert damping constant can be decomposed into two components $\alpha = \alpha_0 + \Delta\alpha$, where α_0 denotes the intrinsic damping of the FM and $\Delta\alpha$ the additional damping due to spin pumping. The intrinsic damping α_0 has been shown to depend as $1/t_{FM}^2$ on the thickness of the ferromagnetic layer t_{FM} due to momentum-nonconserving two-magnon scattering at the interface [41]. In contrast, the additional damping due to spin pumping $\Delta\alpha$ is inversely proportional to the thickness t_{FM} . This $1/t_{FM}$ dependence has also been shown experimentally [42, 43, 44]. It is not an intrinsic property but rather due to the fact that a reduced total magnetisation is more sensitive to a given spin-current loss at the interface.

2.3.2 Magnetisation relaxation mechanisms

There are several relaxation mechanisms, which contribute to Gilbert damping. They can be subdivided into intrinsic, material system dependent effects and extrinsic effects, such as sample structure and measurement geometry. We shall briefly introduce the most relevant mechanisms in the following sections starting with three intrinsic effects succeeded by extrinsic effects. In the last subsection, we shall focus on spin pumping and extraction of the spin-mixing conductance from linewidth broadening.

Magnon-electron interactions

The dominating intrinsic relaxation mechanism in metallic ferromagnets is based on magnon-electron interaction. There are two models that describe magnon scattering with itinerant electrons. The first theoretical approach makes use of the $s - d$ exchange

interaction [45, 46]. In this model, the interaction between the spin of the itinerant electrons and the spin of the localised electrons, which can be treated classically as magnetisation, is studied. The spin waves, which are created at FMR, mediate the spin torque on the magnetisation dynamics and introduce spin-flip scattering leading to relaxation of magnetisation. The second model is known as *breathing Fermi surface* [47]. When the magnetisation varies in time, the spins of the conduction electrons tend to follow the direction of the magnetisation with a time delay. This phase lag dissipates energy and hence leads to relaxation of the magnetisation.

Magnon-phonon interactions

In addition to the intrinsic mechanism mentioned in the preceding paragraph, magnon-phonon interactions can cause relaxation. Let us consider a lattice with spins sitting on each site. When a spin is precessing, it exerts an alternating attractive and repulsive force on its neighbouring spins. This periodic modulation results in phonons in the lattice. Due to time-reversal symmetry, propagating phonons will reciprocally cause spin decoherence. This phenomenon is commonly referred to as the *phonon-drag* [48]. However, it has been shown experimentally that the dissipation of energy during this process is negligibly small compared to the magnitude of intrinsic Gilbert damping [49, 50].

Eddy currents

Another source of intrinsic damping can arise from eddy currents in the metallic ferromagnetic films. The interaction between the conduction electrons and the microwave excitation field can cause damping of magnetisation. This effect is highly dependent on the material. The metallic ferromagnetic material we are focusing on in this work is permalloy, where damping due to Eddy currents only need to be taken into account for when the thickness of the metal surpasses 100 nm [49]. As our experiments require thin films on the order of 10 nm, we do not have to pay much consideration to this damping mechanism.

Two-magnon scattering

The first extrinsic relaxation mechanism we discuss here is two-magnon scattering. In FMR it involves coupling between the uniform mode and spin waves over a range of wave vectors which are degenerate with the microwave pump [51]. The uniform precession or FMR magnon is destroyed due to scattering at an inhomogeneity, and

a spin wave magnon is created. This process leads to damping of the precession of the magnetisation. This effect contributes significantly to damping in films which are magnetised in the film plane and depends strongly on interfacial roughness [52, 53]. Furthermore, it scales with the square of the film thickness.

Slow-relaxer

The mechanism of slow-relaxing impurities was initially developed to explain the additional damping in rare earth doped Yttrium Iron Garnet, a ferrimagnetic insulator, and in exchange bias systems [54, 55]. In permalloy, this mechanism only becomes significant, when the metal is doped with rare earth impurities. This introduces anisotropy in the exchange interaction between the $4f$ magnetic moments and the conduction band [56]. At FMR, the precession of the $4f$ magnetic moments is slowed down by the spin-lattice relaxation of the impurities, which leads to a relaxation of the magnetisation.

Magnetic inhomogeneities

Surface anisotropy, for example, due to roughness, leads to local variation of the effective magnetic field [57]. This causes the spins to precess along local axes with different orientation. The nonuniformity of the precession results in additional damping, which is highly dependent on the surface morphology.

Eddy currents in adjacent non-magnetic films

In multi-layer structures, where the ferromagnetic material is brought into direct contact with a conductive layer, the microwave excitation field can generate Eddy currents in the non-magnetic material. These Eddy currents can create a feedback magnetic field at radio frequency, which leads to decoherence of the precession of the magnetisation of the ferromagnet [58]. This effect manifests itself by altering the lineshape of the microwave absorption signal. As the conductivity of the OSCs we are studying in this work is comparably low, we can safely neglect the contribution of this relaxation mechanism.

Spin pumping

Let us consider a bilayer structure where a nonmagnetic material (NM) is directly adjacent to a ferromagnetic material (FM). When FMR is excited in the FM, the precession of magnetisation creates an excess of spin angular momentum, which is

emitted into the NM [59, 60, 61]. Hence, this *spin pumping* process injects a spin current consisting of an AC and a DC component from the FM into the NM. An illustration of this effect is shown in figure 2.4. Due to the loss of spin angular momentum into the NM, the Gilbert damping is increased. When the thickness of the NM is on the order of the spin diffusion length, the injected spin cannot be dissipated fully. The spin accumulation in the NM creates a backflow of spin into the FM, which again decreases the damping. A theoretical description of spin pumping in the context of parametric pumping shall be discussed in the following.

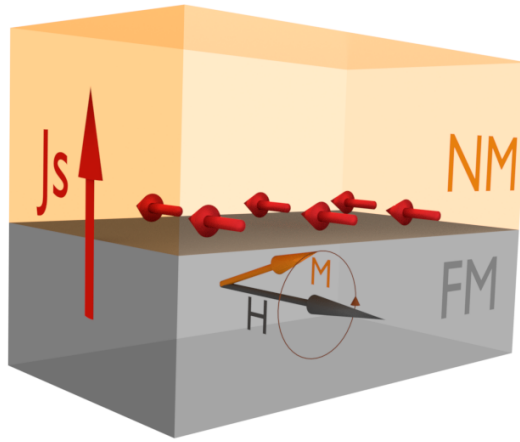


Fig. 2.4 Illustration of spin pumping. A spin current J_s is injected from the FM into the NM at FMR.

Following the work of Tserkovnyak *et al.* [62, 59], we consider an FM sandwiched between two NMs. We can write the operator \hat{I} for the charge and spin current in the l -th lead (l denoting the left (L) or right (R) NM) expressed in terms of operators $a_{\alpha m, l}(E)$ [$b_{\alpha m, l}(E)$] that annihilate a spin- α electron with energy E leaving [entering] the l -th lead through the m -th channel as

$$\hat{I}_l^{\alpha\beta}(t) = \frac{e}{\hbar} \sum_m \int dE dE' e^{i(E-E')t/\hbar} [a_{\beta m, l}^\dagger(E) a_{\alpha m, l}(E') - b_{\beta m, l}^\dagger(E) b_{\alpha m, l}(E')]. \quad (2.14)$$

Assuming that the scattering matrix of the FM varies slowly compared to the time scale of electronic relaxation in the system, an adiabatic approximation for spin pumping is justified. We can identify the azimuthal angle of the magnetisation direction in the plane perpendicular to the precession axis as the single time-dependent parameter. Following the derivation of the scattering approach to parametric pumping of Brouwer [63], we can show that the charge current indeed vanishes and the pure spin current due to

spin pumping takes the expression of

$$\mathbf{I}_s = \mathbf{I}_s^{\text{pump}} - \mathbf{I}_s^{\text{back}}, \quad (2.15)$$

where the injected spin current, expressed in terms of the complex spin pumping conductance $A = A_r + iA_i$, is given by

$$\mathbf{I}_s^{\text{pump}} = \frac{\hbar}{4\pi} (A_r \mathbf{M} \times \frac{d\mathbf{M}}{dt} - A_i \frac{d\mathbf{M}}{dt}) \quad (2.16)$$

and the backflow of spin current as a function of the complex spin-mixing conductance $g^{\uparrow\downarrow} = g_r^{\uparrow\downarrow} + ig_i^{\uparrow\downarrow}$ is given by

$$\mathbf{I}_s^{\text{back}} = \frac{\hbar}{4\pi} (g_r^{\uparrow\downarrow} \mathbf{M} \times \frac{d\mathbf{M}}{dt} - g_i^{\uparrow\downarrow} \frac{d\mathbf{M}}{dt}). \quad (2.17)$$

We note that the real part of the net injected spin current $\mathbf{I}_s^{\text{pump}} + \mathbf{I}_s^{\text{back}}$ adopts the dependency on the magnetisation dynamics as the Gilbert damping term from equation 2.9. Therefore, assuming that the imaginary parts are negligible and that the precession frequency ω is smaller than the spin-flip scattering rate $\omega \ll \tau_{SF}^{-1}$, we can rewrite the additional Gilbert damping constant $\Delta\alpha$ due to spin pumping as a function of the ratio of thickness t_{NM} of the NM to spin diffusion length λ_{SD} as

$$\Delta\alpha = \left[1 + g^{\uparrow\downarrow} \frac{\tau_{SF} \delta_{SD} / \hbar}{\tanh(t_{NM} / \lambda_{SD})} \right]^{-1} \frac{g_L g^{\uparrow\downarrow}}{4\pi\mu}, \quad (2.18)$$

where g_L is the g -factor, μ is the total magnetic moment of the film and δ_{SD} denotes the effective energy-level spacing of the states participating in the spin-flip scattering events. This model has been developed for metals with large spin-flip probability. The precession frequency in our experiments is given by $\omega \sim 10^{10} \text{ s}^{-1}$ while the spin-flip rate in OSCs has been determined to be on the order of $10^4 - 10^8 \text{ s}^{-1}$ [64]. Therefore, the assumption that $\omega \ll \tau_{SF}^{-1}$ does not strictly apply to our material systems. In this *spin battery* regime, the spin accumulation is expected to be reduced due to slow spin relaxation, which causes a larger backflow of spin current implying less net spin injection [60]. However, the qualitative dependence on the film thickness from the aforementioned model for metals still holds.

In a perfect spin sink, where there is no backflow of spin current, we can express the increase in the Gilbert damping constant in terms of the increase in linewidth from the pristine FM (ΔH_{FM}) to the linewidth with the additional adjacent NM (ΔH_{NM})

as

$$\Delta\alpha = \frac{\gamma}{\omega}(\Delta H_{NM} - \Delta H_{FM}). \quad (2.19)$$

Using this, we can get a straightforward estimate for the effective spin-mixing conductance $g_{eff}^{\uparrow\downarrow}$ in terms of the linewidth broadening (LWB) due to spin pumping from the FM into the NM

$$g_{eff}^{\uparrow\downarrow} = \frac{4\pi M_s t_{FM}}{\hbar\omega}(\Delta H_{NM} - \Delta H_{FM}). \quad (2.20)$$

We note that the apparent dependence on the thickness of the FM and the resonance frequency in this equation is compensated by the dependence of the linewidth on these parameters making $g_{eff}^{\uparrow\downarrow}$ a pure measure of the spin pumping efficiency across the FM/NM interface.

Broadening of the FMR linewidth has been used in various studies in literature to investigate spin injection from FM into NM via spin pumping and has been proven to be a sensitive and straightforward method for quantifying the spin-mixing conductance [65, 16, 66, 67, 42, 41, 68]. The extracted values of spin injection efficiency vary between different experimental findings as it depends strongly on the interface. For spin pumping into the standard spin-sink layer, platinum, from YIG and permalloy, the reported spin mixing conductance lies in a range of $g^{\uparrow\downarrow} = 10^{18} - 10^{20} \text{ m}^{-2}$ and the theoretically predicted scaling of the Gilbert damping constant α with thickness of the FM and NM films has been confirmed.

2.3.3 Thermal spin injection

Thermal spin injection is based on the spin Seebeck effect (SSE). Two different theoretical models are trying to explain the underlying mechanism of the SSE. The first one was developed by S. Rezende *et al.* [69]. They assume that a spin current is generated in the bulk of the ferromagnetic insulator (FMI) due to the thermal gradient across the FMI, which is then injected into the adjacent normal metal (NM). J. Xiao *et al.*, on the other hand, developed a microscopic model proposing that it is a pure interface effect [70]. In this case, the spin current is thought to be due to the difference in effective temperature between magnons in the FMI and conduction electrons in the NM. A summary of both models is presented in the following.

The theoretical model of S. Rezende *et al.* [69] relies on the generation of a spin-current carried by magnons in the bulk of the FMI and not only on the interface. However, it does require contact with the normal metal for continuity of the spin flow

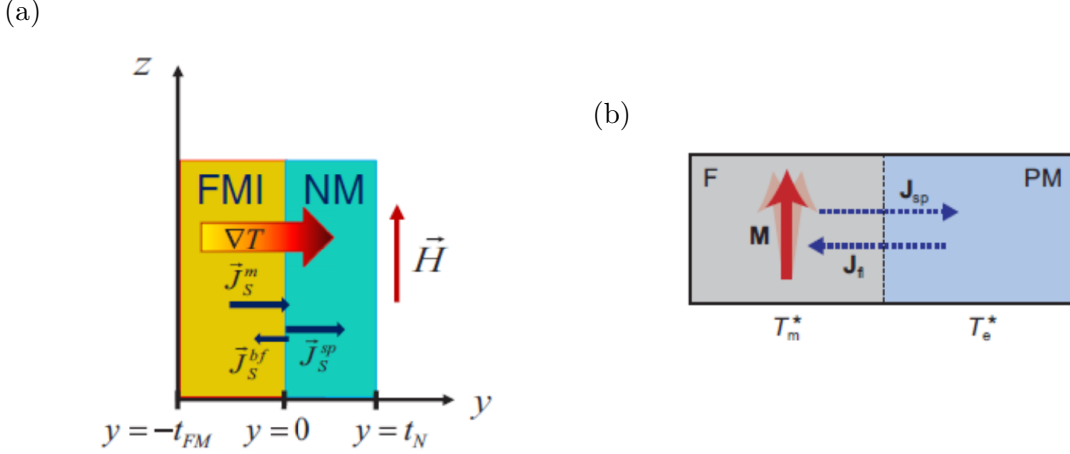


Fig. 2.5 (a) FM/NM bilayer structure that was investigated by Rezende *et al.* with a magnetic field along and temperature gradient perpendicular to the interface (taken from [69]). (b) Bilayer structure used to study the SSE by Xiao *et al.* with the ferromagnet (F) on the left with effective magnon temperature T_m^* and a metal (PM) on the right-hand side with effective electron temperature T_e^* (taken from [71])

across the interface. The structure investigated, and the choice of coordinate system is shown in figure 2.5a. Let n_k denote the number of magnons with wavenumber k in the FMI. The number of magnons in thermal equilibrium n_k^0 is then given by the Bose-Einstein distribution $n_k^0 = 1/(\exp(\hbar\omega_k/k_bT) - 1)$. Considering a FMI/NM bilayer structure as shown in figure 2.5a, the magnon spin-current density with polarisation z can be written as

$$\mathbf{J}_S^z = \frac{\hbar}{(2\pi)^3} \int d^3k \mathbf{v}_k (n_k - n_k^0) \quad (2.21)$$

where \mathbf{v}_k is the k magnon velocity. Making use of the Boltzmann transport equation, one can show that the spin current can be written as a sum of two contributions, $\mathbf{J}_S^z = \mathbf{J}_{S\nabla T}^z + \mathbf{J}_{S\delta n}^z$. Here, $\mathbf{J}_{S\nabla T}^z$ is due to the thermal gradient and $\mathbf{J}_{S\delta n}^z$ is due to the spatial distribution of the magnon accumulation. By expanding and evaluating both terms separately, the following expression for the total y component of the z -polarised magnon spin-current density in the FMI is obtained:

$$J_S^z(y) = -S_S^z \nabla_y T + \hbar \frac{D_m}{l_m} A \sinh((y + t_{FM})/l_m) + \hbar \frac{D_m}{l_m} B \cosh((y + t_{FM})/l_m). \quad (2.22)$$

In the first term, S_S^z can be interpreted as the spin analogue of the Seebeck coefficient. It depends on the average temperature and the normalised magnon energy $\hbar\omega_k/k_bT$. The constants D_m and l_m denote the diffusion parameter and diffusion length respectively, and t_{FM} is the thickness of the FMI. The coefficients A and B are determined by

boundary conditions. The flow of angular momentum through the FMI/NM interface has to be conserved. This means that the spin current has to be continuous across the interface. We impose two boundary conditions. At the substrate/FMI interface $\mathbf{J}_S^z(y = -t_{FM}) = 0$ and at the FMI/NM interface the spin current is continuous, i.e. $\mathbf{J}_S^z(y = 0^-) = \mathbf{J}_S^z(y = 0^+)$. In YIG/Pt bilayer structures the spin density at the interface becomes approximately

$$\mathbf{J}_S^z(0) = -\frac{bg_r^{\uparrow\downarrow}\rho}{a}S_S^z\nabla T \quad (2.23)$$

where a and b are constants, and $g_r^{\uparrow\downarrow}$ denotes the real part of the spin-mixing conductance. Furthermore, ρ accounts for the effect of the finite layer thickness of the FMI which is given by

$$\rho = \frac{\cosh(t_{FM}/l_m) - 1}{\sinh(t_{FM}/l_m)}. \quad (2.24)$$

It follows that in this model direct contact of the NM and FMI layer is crucial and the generated spin-current is proportional to the spin-mixing conductance and linearly dependent on the temperature gradient.

J. Xiao *et al.* assume that the SSE is generated in the interface between the FMI and the NM [70, 71]. Starting with the macrospin approximation, there is a spin-current noise \mathbf{I}_{SP} injected from the FM into the NM at finite temperature,

$$\mathbf{I}_{SP}(t) = \frac{\hbar}{4\pi}(g_r^{\uparrow\downarrow}\mathbf{m}(t) \times \dot{\mathbf{m}}(t) + g_i^{\uparrow\downarrow}\dot{\mathbf{m}}(t)) \quad (2.25)$$

where $g_r^{\uparrow\downarrow}$ and $g_i^{\uparrow\downarrow}$ are the real and imaginary part of the spin-mixing conductance respectively and \mathbf{m} a unit vector in the direction of the magnetisation. This spin-pumping current is proportional to the effective magnon temperature T_m in the FM. The term including the real part of the spin-mixing conductance is of the same form as the Gilbert damping term in the Landau-Lifshitz-Gilbert equation (2.9). According to the fluctuation-dissipation theorem, thermal fluctuations of the spin accumulation in the NM emit a spin-current \mathbf{I}_{fl} , also known as Johnson-Nyquist spin-current noise, back from the NM into the FM, which is proportional to the effective electron temperature T_e in the NM. This can be represented by a random magnetic field \mathbf{h}_r acting on the magnetisation:

$$\mathbf{I}_{fl}(t) = -M_S V \mathbf{m}(t) \times \mathbf{h}_r(t). \quad (2.26)$$

Here, M_S denotes the saturation magnetisation, and V is the total volume of the FM. The total spin-current across the interface \mathbf{I}_S can now be written as the sum of the spin pumping current and the Johnson-Nyquist spin-current noise: $\mathbf{I}_S = \mathbf{I}_{SP} + \mathbf{I}_{fl}$. By taking the time average, the dc component of the spin-current is determined to be proportional to the real part of the spin-mixing conductance and the difference of the effective temperatures:

$$\mathbf{I}_S \propto g_r^{\uparrow\downarrow}(T_m - T_e). \quad (2.27)$$

A more intuitive description and explanation of the SSE is given by H. Adachi *et al.* [72]. In the longitudinal spin Seebeck effect both, the FM and NM layer, are in contact with the heat bath. Most of the heat-current is carried by phonons in FM/NM systems at room temperature. Assuming that the interaction between conduction electron spins in the NM and phonons is much stronger than between magnons and phonons, the effective electron and magnon temperature will be different at the interface. Hence, a spin-current in the NM is generated.

Surprisingly, the resulting expressions for the spin current are very similar for both theoretical models presented above, even though the initial assumptions are very different. They come to the conclusion that the spin-current is proportional to the spin-mixing conductance and the temperature gradient.

The SSE has been first shown experimentally by K. Uchida *et al.* in 2008 [73] and thoroughly since in YIG/Pt bilayer structures [74, 75, 76, 77].

2.3.4 Optical spin injection

In addition to spin pumping and thermal spin injection, photoexcitation is an alternative way of injecting spin-polarized electrons in nonmagnetic semiconductors. Due to characteristic transition rules in direct band-gap semiconductors, spin polarised electron-hole pairs can be excited with circularly polarised light [78, 79]. For this, the energy $h\nu$ of the photons needs to be on the order of the band gap E_g .

A commonly used material is GaAs, which was studied in this work as well [80]. The band structure around the Γ -point in the centre of the Brillouin zone is shown in figure 3.5b. The $S_{1/2}$ state in the conduction band (cb) is separated from the $P_{3/2}$ states in the valence band for heavy holes (hh) and light holes (lh) by an energy gap of $E_g = 1.43$ eV at room temperature. The $P_{1/2}$ state in the split-off band lies at an

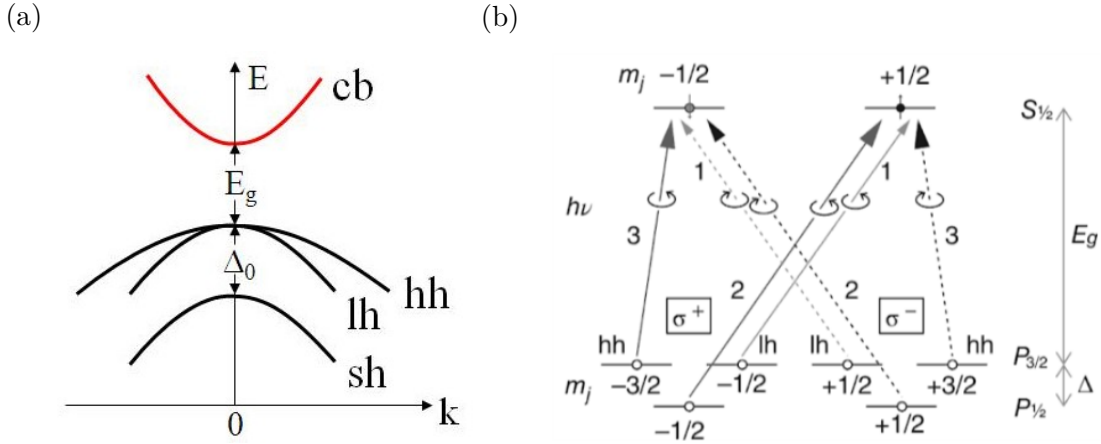


Fig. 2.6 (a) Schematic band structure of GaAs around the centre of the Brillouin zone. The energy gap between the conduction band (cb) and the valence band for heavy holes (hh) and light holes (lh) is denoted as E_g . The split-off band (sh) is lower in energy by Δ_0 due to spin-orbit splitting (reproduced from [78]). (b) Schematic of weighted transitions for right (σ^+ , solid lines) and left (σ^- , dashed lines) polarised light in GaAs (taken from [79]).

energy $\Delta_0 = 0.34$ eV below $P_{3/2}$. The selection rule for optical excitation is $\Delta m_j = +1$ for circularly right (σ^+) and $\Delta m_j = -1$ for circularly left (σ^-) polarised light. The allowed transitions are shown in figure 2.6b. The numbers near the arrows indicate the relative transition probabilities. When $h\nu = E_g$, three times more spins are excited from the hh than the lh with circularly polarised light. Consequently, the maximum spin polarisation is expected to be 50% in theory. Due to practical limitations, the maximum spin polarisation observed experimentally is $\sim 40\%$ [81]. For $h\nu > E_g + \Delta_0$ the lh and hh states start to mix with the sh band. This interband absorption reduces the spin polarisation due to spin-orbit interaction.

2.4 Spin relaxation in non-magnetic materials

Materials in which spin-encoded information can be retained over long times and distances are of great importance for technological applications [82]. Therefore, studying the relaxation of spin, the process of randomisation and equilibration of spin, is crucial in spintronics. After introducing the spin relaxation and spin dephasing times T_1 and T_2 , we will discuss the four major mechanisms for spin relaxation in metals and inorganic semiconductors and focus on spin relaxation in OSCs in the last section.

2.4.1 Spin relaxation and spin dephasing time

Spin precession, decay and diffusion of electronic magnetisation are traditionally defined with the Bloch-Torrey equations [83, 84]. The magnetisation \mathbf{M} in an externally applied magnetic field $\mathbf{B}(t) = B_0\hat{\mathbf{z}} + \mathbf{B}_1(t)$, where \mathbf{B}_1 is oscillating perpendicular to $\hat{\mathbf{z}}$, can be expressed in terms of the spin relaxation time T_1 and spin decoherence time T_2 using

$$\frac{d\mathbf{M}}{dt} = \gamma\mathbf{M} \times \mathbf{B} - \frac{M_x\mathbf{e}_x}{T_2} - \frac{M_y\mathbf{e}_y}{T_2} - \frac{(M_z - M_0)\mathbf{e}_z}{T_1} + D\nabla^2\mathbf{M}, \quad (2.28)$$

where γ denotes the electron gyromagnetic ratio, D is the scalar diffusion coefficient (for simplicity we assume an isotropic medium) and $M_0 = \chi B_0$ is the thermal equilibrium magnetisation with susceptibility χ of the model system. Even though real systems can be very complicated, T_1 and T_2 are a very robust measure for quantifying processes of magnetisation dynamics. The spin relaxation time T_1 is the characteristic time it takes for the spin population to reach thermal equilibrium with the lattice. This process is usually mediated by phonons. The spin decoherence time T_2 is the time it takes for an ensemble of initially in phase precessing spins to lose their relative phase due to spatial and temporal fluctuations of the precession frequencies.

2.4.2 Elliott-Yafet mechanism

Elliott found a spin-flip mechanism where electron spins can relax via momentum scattering if the lattice ions induce spin-orbit coupling (SOC) in the electron wavefunction [86]. When spin-orbit interaction is present in a periodic lattice, the eigenstates of $\hat{\sigma}_z$ are no longer given by single-electron Bloch wave functions but rather a mixture of the Pauli spin-up $|\uparrow\rangle$ and spin-down $|\downarrow\rangle$ states. Momentum scattering is typically caused by impurities at low temperature and phonons at high temperature. Combining SOC and momentum scattering, the spin-up and spin-down states can couple, which leads to spin relaxation. Yafet introduced an additional spin-flip scattering mechanism which is induced by phonons [87]. The periodic spin-orbit interaction due to the lattice ions is modified by phonons. This effect can directly couple the Pauli spin-up and spin-down states. Combining these two effects, we obtain phonon-induced spin relaxation due to spin-flip scattering. The higher the momentum scattering rate is, the stronger the spin relaxation will be. An illustration of the Elliott-Yafet mechanism can be found in figure 2.7a.

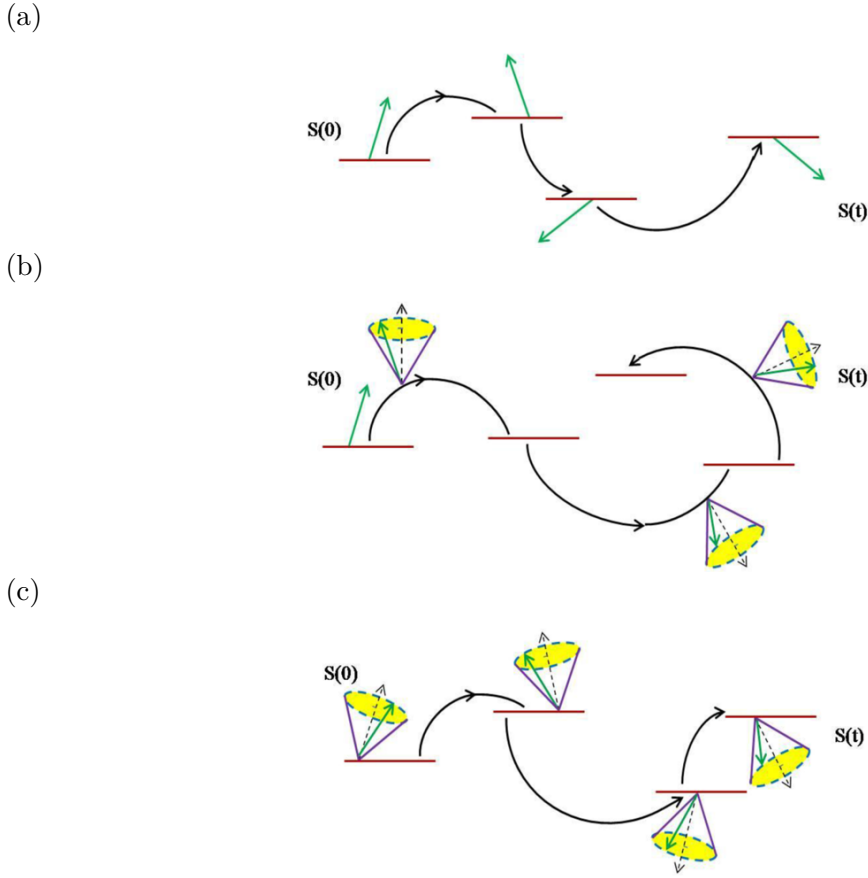


Fig. 2.7 Illustration of three different spin relaxation mechanisms, (a) Elliott-Yafet mechanism, (b) D'yakonov-Perel' mechanism and (c) Hyperfine interaction (illustrations are taken from [85]).

2.4.3 D'yakonov-Perel' mechanism

In lattices without inversion symmetry, the spin-orbit interaction lifts the degeneracy of the momentum states of the spin-up and spin-down electrons [88]. The asymmetry results in effective electrostatic potential gradients that a charge carrier moving at speed v experiences. Taking the Lorentz transformation, this corresponds to an effective internal magnetic field $\mathbf{B}_i(\mathbf{k})$, which is proportional to v and around which the electron spins precess. The corresponding Hamiltonian of the precessing conduction band electrons is given by $H(\mathbf{k}) = \frac{1}{2}\hbar\sigma(e/m)\mathbf{B}_i(\mathbf{k})$, where e and m denote the elementary charge and mass of an electron respectively. The combination of momentum-dependent spin precession and momentum scattering leads to spin dephasing (see figure 2.7b). We note that spin relaxation is more efficient in high mobility materials, as $\mathbf{B}_i(\mathbf{k})$ is proportional to speed v of the electron. Therefore, in contrary to the Elliott-Yafet

mechanism, D'yakonov-Perel' mechanism is inversely proportional to the momentum scattering rate.

2.4.4 Bir-Aronov-Pikus mechanism

The Hamiltonian describing the interaction between electrons and holes is given by $H = AS \cdot J\delta(\mathbf{r})$, where A is a constant proportional to the exchange integral between the conduction and valence states, \mathbf{S} and \mathbf{J} denote the electron and hole spin operator respectively, and \mathbf{r} is the distance between the electron and hole. Due to the strong spin-orbit interaction in the valence band, the holes have a high probability for spin-flips. As a result of the coupling, the electron spin is then flipped as well, which leads to spin-relaxation of electrons [89]. As this effect requires significant overlap of the electron and hole wave function, this is dominant in bipolar semiconductors.

2.4.5 Hyperfine interaction

The hyperfine interaction (HFI) is the interaction between the spin angular momentum of the electrons and the nuclei. This interaction can induce ensemble spin dephasing and single-spin decoherence of localised electrons due to the effective magnetic fields created by the nuclear spins [90]. It is the dominant cause for spin relaxation in systems where charge carriers are strongly localised in space and have no resultant momentum, hence are quasi-static. An illustration of the spin relaxation due to the nuclear fields experienced at every dwelling-site is shown in figure 2.7c.

2.4.6 Spin relaxation in organic semiconductors

There have been only few theoretical studies on spin relaxation in organic semiconductors so far [85, 91, 92, 93, 94]. Even though the aforementioned spin relaxation mechanisms have been developed for the framework of metals and inorganic semiconductors, we can expand the concepts and will discuss their relevance in OSCs in this section.

At low temperature, the hopping frequency of the charge carriers is small, implying a long dwell time at each site, where the spins experience and precess around a local magnetic field. The variation in local field between sites is given by different HFI and by spin-orbit fields originating from a spread in g-tensor orientations. With sufficiently long dwell time, the Larmor frequency of the spin changes according to the change in local field. This effect is commonly known as *Motional Relaxation*. As the temperature

increases, the dwell time reduces, and the effect of the change in local fields from site to site is decreased. This *motional narrowing* is akin to the D'yakonov-Perel' mechanism, which we introduced in section 2.4.3.

There are two spin relaxation mechanisms, which come into play at higher temperatures. When a charge carrier is localised at a site, it experiences a fluctuating magnetic field due to modulation of SOC and HFI fields by molecular vibrations. However, this *intra-site relaxation* requires Raman-like multi-vibron processes and is therefore expected to be weaker than the competing spin relaxation mechanisms [95].

As mentioned in section 2.1, the charge carrier wave functions are quasi-localised over the molecules or segments of the polymer backbone, and polarons are transported via incoherent hopping from site to site, in the organic systems we are studying in this work. The phonon-induced incoherent hopping allows mixing of the spin-up and spin-down states allowing hopping events, where the spin is not conserved. The polaronic nature of charge transport implies that the concept of Elliott-Yafet-type spin relaxation can be applied in our material systems as well [96].

Seeing that the organic materials we are studying in this work are unipolar, the Bir-Aronov-Pikus mechanism is not expected to play an important role. It might, however, play a more significant role in spin-based organic light emitting diodes based on bipolar semiconductors.

The OSCs constitute mainly of Carbon and Hydrogen. The most abundant isotope of Carbon, ^{12}C , has zero nuclear spin, while the common Hydrogen atoms, ^1H , carry a nuclear spin of $1/2$. Consequently, the hyperfine interaction mainly originates from the Hydrogen atoms. Deuterium, ^2H , has a much weaker hyperfine coupling strength than ^1H . This allows studying the effect of hyperfine interaction on spin relaxation by employing deuterated OSCs.

2.5 Spin detection via spin-to-charge conversion

There are many measurement instruments that one can employ to measure a charge current or voltage directly. However, detecting a spin current or spin accumulation is unfortunately not as straightforward. Apart from the technique of measuring the increase in damping due to spin injection described above, there are several commonly used methods including optical and electrical spin detection. In this section, we shall focus on mechanisms, which are based on the spin Hall effect.

2.5.1 Spin Hall effect

The conventional *Hall effect* describes the creation of an electromotive force transverse to a charge current in a perpendicular magnetic field due to the Lorentz force [97]. Figure 2.8a shows an illustration of this effect. An effect akin to the conventional Hall effect can be observed in ferromagnetic materials, where a charge current perpendicular to the magnetisation direction creates a transverse voltage. This so-called *anomalous Hall effect* (AHE) originates from spin-orbit interaction causing spin-dependent scattering of conduction electrons (see figure 2.8b) [98]. The strong imbalance in the charge current between spin-up (majority) and spin-down (minority) electrons gives rise to a transverse voltage due to the spin-asymmetric scattering. A similar effect, the *spin Hall effect* (SHE, figure 2.8c) can also be observed in nonmagnetic materials with strong spin-orbit coupling [17]. Here, a charge current gives rise to a transverse spin current that creates spin accumulation with opposite spin polarisation at opposite boundaries.

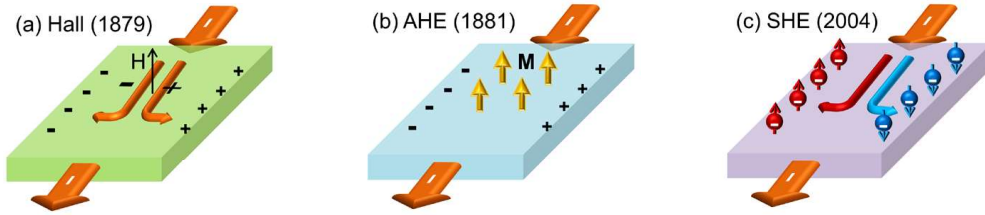


Fig. 2.8 Schematic of (a) Hall effect, (b) anomalous Hall effect and (c) spin Hall effect (illustrations are reproduced from [99]).

The SHE was first predicted by Dyakonov and Perel in 1971 [100] and later rediscovered by Hirsch in 1999 [101]. There are three different mechanisms based on spin-orbit interaction, which have been identified as the origin of the SHE. In vacuum, the Hamiltonian for SOC can be written in the following form

$$\mathcal{H} = -\eta_{SO}\sigma[\mathbf{k} \times \nabla V_{vac}(\mathbf{r})], \quad (2.29)$$

where $\eta_{SO} = (\hbar/2mc)^2$, with the mass of the electron m and speed of light c , $V_{vac}(\mathbf{r})$ is the potential acting on an electron with momentum $\mathbf{p} = \hbar\mathbf{k}$ and σ denotes the Pauli matrices. We can decompose the potential into a periodic potential $V_L(\mathbf{r})$ and a non-periodic term $V(\mathbf{r})$, which represents the impurities, boundaries and externally applied fields.

Let us first consider the non-periodic part of the potential, which gives rise to the

extrinsic SHE mechanisms. The relativistic SOC causes the velocity and coordinate operators and hence also the scattering cross-section to become spin-dependent. As a result, spin-up and spin-down electrons will scatter at different angles from impurities. An illustration of this so-called *Mott-skew scattering* is shown in figure 2.9a.

If there is a momentum transfer during the scattering event, the electron is displaced laterally by $\delta\mathbf{r}$ depending on its spin-state. This *side-jump* mechanism is illustrated in figure 2.9b.

Let us now treat the periodic potential. The intrinsic SHE mechanism is illustrated in figure 2.9c. We can rewrite the effective interaction in the form

$$\mathcal{H}_{SO,int} = -\frac{1}{2}\sigma\mathbf{B}(\mathbf{k}), \quad (2.30)$$

where $\mathbf{B}(\mathbf{k})$ is an effective magnetic field. Here, \mathbf{k} denotes the crystal wavevector. Due to the \mathbf{k} -dependence of \mathbf{B} , the effective magnetic field experienced by an electron depends on its momentum. When an electric field is applied in x -direction, the Fermi surface is shifted by $\delta\mathbf{k}$, which forces the electrons out of alignment with $\mathbf{B}(\mathbf{k})$. This creates an effective torque that results in a spin current in the y -direction.

Experimental evidence for the extrinsic SHE was demonstrated first by Kato *et al.* in 2004 [102]. Simultaneously, Wunderlich *et al.* have experimentally verified the intrinsic SHE [103].

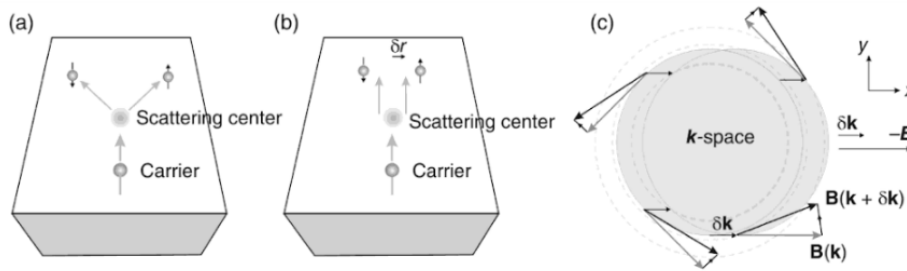


Fig. 2.9 Illustration of three different mechanisms for spin Hall effect. (a) Mott-skew scattering, (b) side-jump and (c) intrinsic SHE mechanism (illustrations are taken from [79]).

Given by time-reversal symmetry, the inverse effect, the *inverse spin Hall effect* (*ISHE*) describes the generation of an electromotive force transverse to a spin current. This effect is commonly used for electrical detection of a spin current. The generated charge current \mathbf{J}_c can be expressed in terms of the spin current \mathbf{J}_s and spin polarisation σ

as

$$\mathbf{J}_c \propto \theta_{SH} \mathbf{J}_s \times \boldsymbol{\sigma}, \quad (2.31)$$

where the spin Hall angle θ_{SH} is a measure of the spin-to-charge conversion efficiency of the material. The first experimental observation of the ISHE has been made in a permalloy/platinum bilayer stack by Saitoh *et al.* [39]. A spin current is injected into the heavy metal from permalloy via spin pumping at FMR and is converted into a transverse ISHE voltage in platinum.

2.5.2 Electrically modulated inverse spin Hall effect

The previously discussed inverse spin Hall effect requires a geometry, where the spin polarisation has a component perpendicular to the direction of the spin current in order to create a transverse voltage. As a result, when the spin polarisation is colinear with the direction of spin injection, we cannot detect a spin signal from ISHE. Therefore, in order to detect spins with spin polarisation parallel to the direction of movement, we have to modify the detection mechanism.

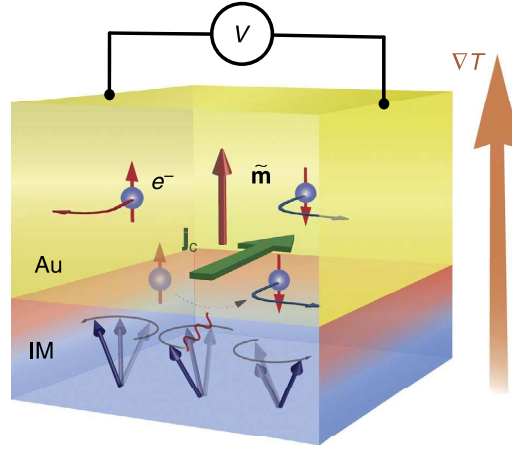


Fig. 2.10 Schematic of the electrically modulated ISHE. An out-of-plane spin polarisation is injected from an insulating ferromagnet (FM) into gold (Au) either due to a thermal gradient or spin pumping. The spins are then accelerated by a drift current (\mathbf{j}_c , green arrow) resulting in a transverse ISHE signal (taken from [104]).

Olejník *et al.* have demonstrated that an additional drift current can modulate the ISHE signal in GaAs [105]. In our geometry, we can use a transverse drift current to accelerate the spins perpendicular to their polarisation. This creates an effective spin current, which is non-colinear with the direction of spin polarisation. As a result, an electrically modulated ISHE voltage signal that depends linearly on the drift current is

induced.

It has been experimentally verified that this allows detecting an out-of-plane spin polarisation, which is injected normal to the interface via thermal spin injection as well as spin pumping, in a YIG/gold bilayer structure [104]. Figure 2.10 shows a schematic of this method of spin detection using the electrically modulated ISHE.

2.5.3 Proposal of thermal spin detection

Following on from the electrically modulated and drift current induced ISHE, we propose the idea to use a thermal gradient as the driving force for spins to induce the ISHE spin detection. This effect shall here be referred to as the *inverse spin Nernst effect (ISNE)* in this work. The heat-current \mathbf{J}_h can be written in terms of the temperature gradient ∇T as

$$\mathbf{J}_h = -\kappa \nabla T, \quad (2.32)$$

where κ denotes the thermal conductivity. Analogously to equation 2.31, we can express the charge current \mathbf{J}_c created by the ISNE as

$$\mathbf{J}_c \propto \theta_{SN} \nabla T \times \boldsymbol{\sigma}, \quad (2.33)$$

where θ_{SN} denotes the spin Nernst angle.

The inverse effect, the spin Nernst effect (SNE), which describes the creation of a spin accumulation due to a transverse temperature gradient, has recently been measured successfully [19].

Chapter 3

Experimental Methods

This chapter is dedicated to introducing the experimental details. The first section presents the materials studied in this work, followed by the techniques used for fabricating the samples. The last section focuses on the experimental setups and measurement procedures.

3.1 Materials

3.1.1 Ferromagnetic materials

Permalloy

There are several metallic ferromagnetic materials which are commonly used in spin pumping experiments. We have compared three metals, cobalt (Co), iron (Fe) and permalloy (Ni 81% Fe 19%, 99.99% purity, Py) to find a suitable material for the linewidth broadening study. Reproducibility of magnetic properties of metallic films for different samples and batches of evaporation was the primary criterion.

The average of four samples each of the in-plane resonance field H_{FMR} and linewidth ΔH of the microwave absorption at FMR are listed in table 3.1 for the three materials at an excitation of 9 GHz. Both, the variation of the resonance field as well as the linewidth are smallest for permalloy. The small intrinsic damping in Py stems from

Table 3.1 Magnetic properties of permalloy, cobalt and iron at FMR

	Permalloy	Cobalt	Iron
H_{FMR} (G)	1121 ± 2	656 ± 5	683 ± 5
ΔH (G)	33.7 ± 0.1	65 ± 3	69 ± 9

the low anisotropy and small magnetoelastic coupling [106]. As a consequence, spin pumping from Py has shown to be very efficient in comparison with other FMs and is a promising candidate for our experiments [65].

Furthermore, the resonance field at out-of-plane magnetic field of cobalt and iron exceed the maximum magnetic field we can apply in the Electron Spin Resonance setup (1.5 T), while $H_{FMR}^{90^\circ}$ lies at 1.1 T for permalloy. This allows doing a full angular dependent characterisation of the Py films, from which we can extract the saturation magnetisation and gyromagnetic ratio of the ferromagnet. For these reasons, this work is focusing on permalloy as ferromagnetic material.

YIG

When doing spin pumping experiments on ferromagnetic metals, there are many effects such as the Anomalous Hall Effect and Anomalous Nernst Effect causing a spurious electromotive force, which superimposes on the ISHE signal from the spin detection layer. One way of circumventing this problem is to use an insulating magnetic material. The most commonly used material in spintronics is Yttrium Iron Garnet ($Y_3Fe_2(FeO_4)_3$, YIG), a ferrimagnetic insulator.

Two types of YIG substrates have been used in this work in the section on thermal spin injection and detection, a 2 μm film and 100 nm film purchased from Innovent and Matesy respectively. The films were grown on Gadolinium Gallium Garnet ($Gd_3Ga_5O_{12}$, GGG) by liquid phase epitaxy (LPE). GGG is commonly used as a substrate for YIG due to its similar lattice constant, which aids the formation of the preferred magnetic crystal structure of YIG. During the deposition process, both sides of the GGG substrate are coated. In order to avoid inaccuracy in the microwave absorption measurements, YIG has been removed from one side. The thin films of YIG were produced by polishing a μm -thick film down to 100 nm. Similarly to the FM metals discussed above, the ferromagnetic resonance of YIG lies in the GHz range.

Due to the $1/t_{FM}$ scaling of the linewidth broadening effect, very thin films of YIG are necessary to study the spin injection via Gilbert damping. For this, YIG has to be deposited via sputtering. We received films with a thickness ranging from $\sim 10 - 20$ nm from Dr M. Amado from the group of Dr J. Robinson in the Department of Materials Science & Metallurgy at the University of Cambridge and A. Mitra from the group of Prof B. Hickey in the School of Physics and Astronomy at the University of Leeds. The advantage of YIG over permalloy is that exposure to ambient conditions during the measurements does not change the magnetic properties. This allowed taking temperature dependent measurements of the linewidth, which were conducted over

the course of several days (more details in appendix A). However, the FMR spectra of the thin YIG films usually showed multiple FMR peaks due to inhomogeneity of the magnetic films, making precise extraction of the linewidth difficult. Furthermore, the availability of samples was highly limited by the complex deposition of YIG films. Due to these reasons, in this work, the linewidth broadening experiments investigating spin injection into organic semiconductors have been conducted using permalloy as the ferromagnetic material.

3.1.2 Organic semiconductors

DNTT derivatives

The first group of small molecule organic semiconductors this work is focusing on is a set of three derivatives of dinaphtho[2,3-b:2',3'-f]thieno[3,2-b]thiophene (DNTT). DNTT is one of the best performing small molecule so far [107, 108]. DNTT is altered by addition of phenyl rings and alkyl side-chains on both ends of the core of the molecule forming diPh-DNTT and C₈-DNTT respectively. Figure 3.1 shows the chemical structure of (a) DNTT, (b) diPh-DNTT and (c) C₈-DNTT. These derivatives are commonly deposited by thermal evaporation and are known to adopt herringbone packing and align edge-on with their long axis perpendicular to the substrate [108]. Experimental verification and a more detailed discussion of the structural properties

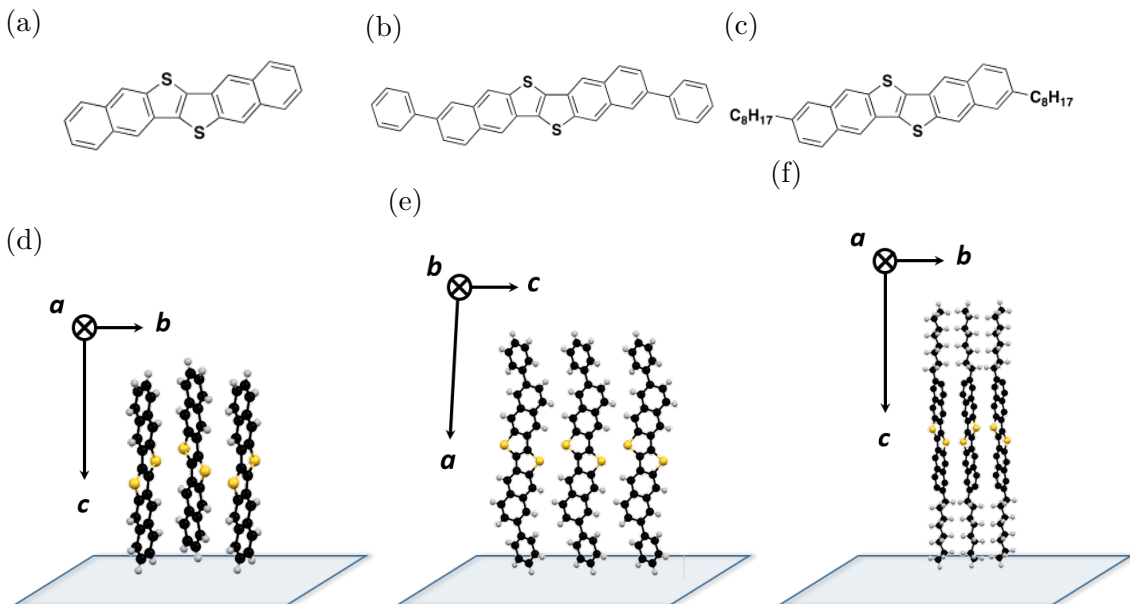


Fig. 3.1 Chemical structure of (a) DNTT, (b) diPh-DNTT and (c) C₈-DNTT. Their crystal packing with respect to the substrate is illustrated in (d)-(f).

is presented in section 5.2. The electronics properties have been studied in thin-film transistor architectures. The characteristics show typical p-type behaviour and the extracted mobilities range from 2 to 3 $\text{cm}^2\text{V}^{-1}\text{s}^{-1}$.

BTBT derivatives

In order to study the generality of the side groups of molecules on spin injection, we investigated another material system, [1]Benzothieno[3,2-b]benzothiophene (BTBT). The molecular structure, as well as the packing of BTBT and C_8 -BTBT, are shown in figure 3.2. In contrast to DNTT, BTBT is commonly solution processed. The mobility extracted from thin-film transistor measurements are comparable to DNTT [109]. The structural and electrical similarities with DNTT makes BTBT an ideal system for a comparative study [110].

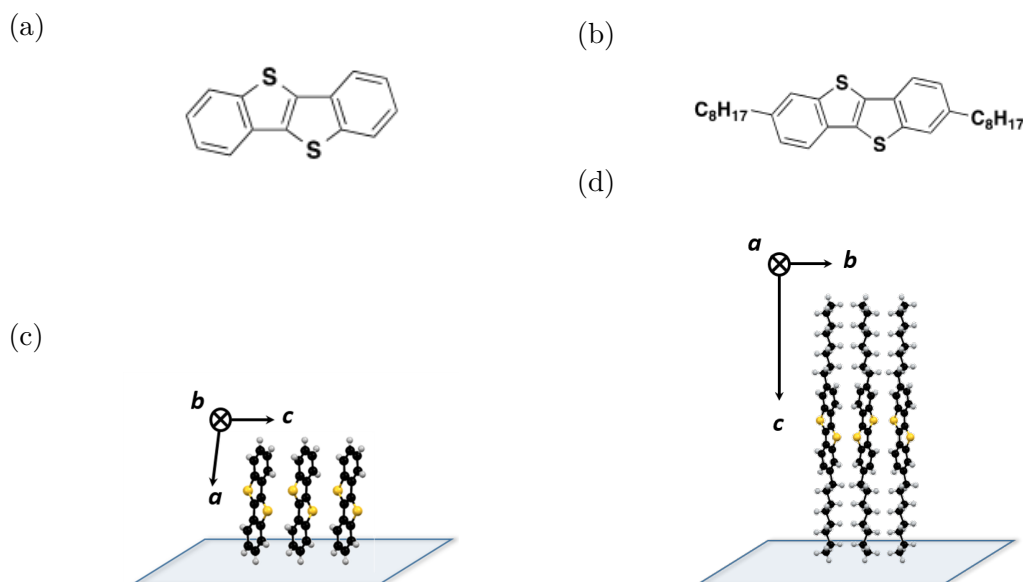


Fig. 3.2 Chemical structure of (a) BTBT and (c) C_8 -BTBT and their crystal packing with respect to the substrate shown in (c) and (d) respectively.

Small molecules with diradical character

The charge carrier density in pristine organic small molecule semiconductors is very low, and for most materials, the HOMO level is too deep for the molecules to be efficiently doped in ambient conditions. Therefore, we can presume that spin injection based on the coupling of the spin angular momentum from the FM with the charge carriers present in the small molecule film is limited by the small charge and hence spin concentration

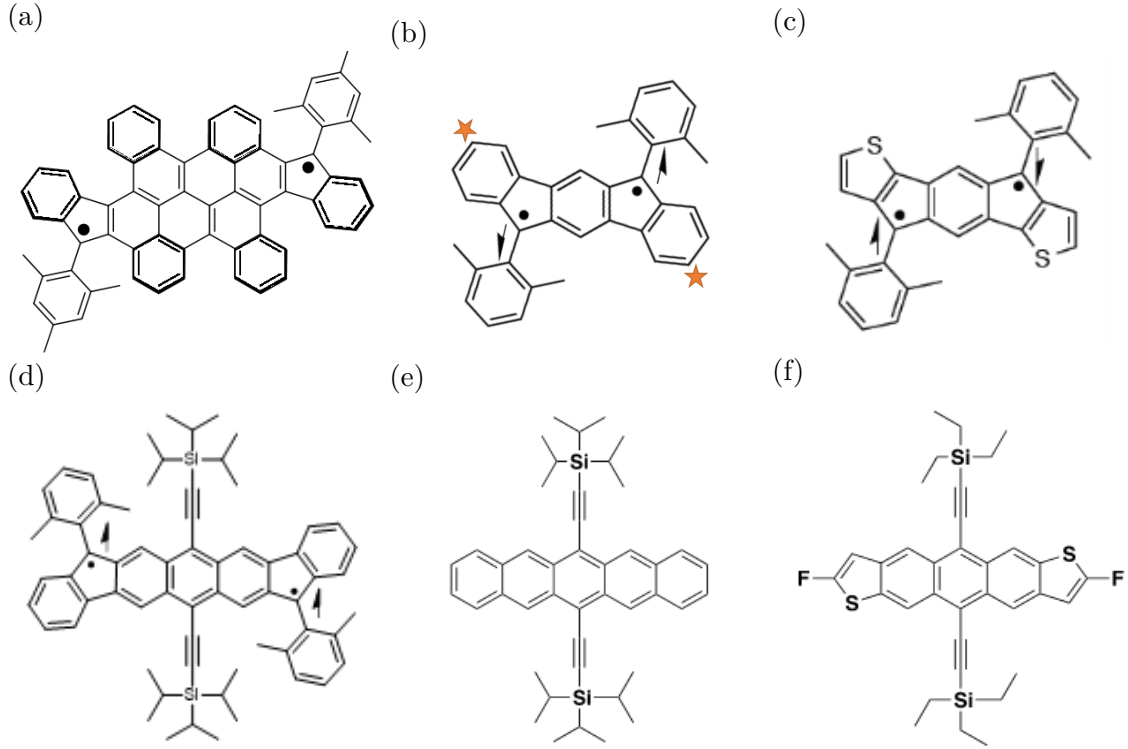


Fig. 3.3 Chemical structure of (a) DFB1, (b) DX-IDF, where the stars indicate the positions for halogenation, (c) DX-IDT, (d) DIADX, (e) TIPS pentacene and (f) diF TES ADT.

induced by charge injection at the interface to the metal contact or unintentional doping. One idea for designing OSCs with enhanced spin-sink characteristics was to make use of the intrinsic spin character of diradical molecules. In these materials the spin parallel triplet level is very close to the spin-paired singlet level allowing thermal population of the spin $S = 1$ triplet state. The index y is a measure of biradical character, ranging from $y = 0$ for purely closed shell systems to $y = 1$ for purely biradical systems. An experimentally accessible definition of y was developed by K. Kamada *et al.* [111], where y is expressed in terms of singlet and triplet energy levels as

$$y = 1 - \sqrt{1 - \left(\frac{E_{S_{1u}, S_{1g}} - E_{T_{1u}, S_{1g}}}{E_{S_{2g}, S_{1g}}} \right)^2}. \quad (3.1)$$

Here, $E_{S_{1u}, S_{1g}}$ denotes the excitation energy from the ground state of the molecule (singlet of gerade symmetry, S_{1g}) to the first ionic singlet state with ungerade symmetry (S_{1u}). Similarly, $E_{S_{2g}, S_{1g}}$ denotes the energy difference between the ground state and the second ionic singlet state with gerade symmetry (S_{2g}). Moreover, $E_{T_{1u}, S_{1g}}$ is given

by the excitation energy from the ground state to the first neutral triplet state (T_{1u}) and is commonly measured in electron spin resonance and superconducting quantum interference device experiments.

Recently, the synthesis of diindeno-fused bischrysene (DFB 1), which exhibits an open-shell singlet biradical structure in the ground state with a narrow optical energy gap of 0.92 eV has been reported in literature [112]. The chemical structure of DFB 1 is shown in figure 3.3a. In addition to the biradical character, the material has been shown to be stable under ambient conditions, making it a very promising candidate for a spin-sink material. Dr J. Liu from the group of Prof X. Feng at Technische Universität Dresden in Germany kindly supplied us with some material for the LWB experiments.

In the context of the ERC Synergy collaboration, Dr M. Little, C. Jellett and A. Marks from the group of Prof I. McCulloch at Imperial College London, designed and synthesised several promising materials aiming for a strong biradical character.

The first set of molecules were based on Indenofluorene (IDF), which is known to have a biradical character [113, 114]. Furthermore, this backbone shows high stability and chemical manipulability, making it a suitable starting point for our investigations. The first molecule developed from IDF was DX-IDF. The chemical structure of DX-IDF and its analogue with Sulfur substitution DX-IDT is shown in figure 3.3b and 3.3c respectively. From DFT calculations of the energy levels of the singlet and triplet state, the biradical character y was determined to be $y = 0.24$ and $y = 0.19$ for DX-IDF and DX-IDT respectively. The morphology of thin films of DX-IDF and IX-IDT was studied with X-ray techniques, which will be discussed in section 5.5. In order to investigate the influence of higher spin-orbit coupling due to the inclusion of heavier atoms in the molecules on spin injection, a halogenation series of DX-IDF was developed. Two Iodide and Bromide atoms have been attached to the core of the molecule at the positions marked with stars in figure 3.3b to form Di-Iodo-DX-IDF and Di-Bromo-DX-IDF respectively.

Moreover, there has been a recent report of a stable open-shell molecule based on the diindeno[b,i]anthracene framework [115]. Starting from this, a similar Anthracene derivative Di-Indeno-Anthracene-Di-Xylene (DIADX) has been developed. The chemical structure of DIADX is shown in figure 3.3d. From DFT calculations the biradical character is expected to be $y = 0.55$.

In order to have a comparison with similar molecules with closed-shell character, we

have also investigated spin injection into 6,13-Bis(triisopropylsilylethynyl)pentacene (TIPS pentacene) and 2,8-Difluoro-5,11-bis(triethylsilylethynyl)anthradithiophene (diF TES ADT), which are both commercially available from Sigma Aldrich. Their chemical structure is shown in figure 3.3e and 3.3f respectively. Due to the bulky TIPS and TES side groups, these molecules arrange in brick-wall style stacking [116, 26].

P3HT derivatives

In addition to the small molecules, we have also investigated spin injection into several conjugated polymers. The choice of material was limited by the strict criterion of solubility in a particular solvent, THF, as discussed later in section 4.4.

The first polymer in this study was poly(3-hexylthiophene) (P3HT), which has previously been thoroughly characterised and studied [3]. The chemical structure of P3HT is shown in figure 3.4a. The backbones of the polymer adopt a lamella structure with two-dimensional conjugated sheets formed by interchain stacking. Structural characterisation of the P3HT thin films on permalloy substrates will be discussed in section 6.1. C. Jellett has kindly provided us with the material and repurified the polymer, which allowed us to exclude significant contribution of impurities to the LWB measurements. The molecular weight was determined to be 23 kDa, which ensured good solubility in THF.

The HOMO of P3HT lies at ~ -4.9 eV [117]. As a consequence, the polymer is easily unintentionally doped with oxygen by exposure to air, which significantly increases the charge carrier concentration [118].

In order to investigate the influence of the hyperfine field interaction on spin injection, we have also studied LWB in deuterated P3HT (d-P3HT). In d-P3HT the spin- $1/2$ Hydrogen atoms of conventional P3HT have been substituted with spin- 1 Deuterium atoms (shown in figure 3.4b). The change in nuclear spin induces a change in the hyperfine field, which is expected to be reflected in the spin relaxation in the OSC as mentioned in section 2.4.6.

The strength of SOC in the polymer can be increased by heavy element substitution. Stronger SOC results in more efficient spin relaxation in the OSC. Consequently, the backflow of spin current due to the interfacial spin accumulation is reduced, leading to a higher spin injection efficiency. In order to test this hypothesis, Dr M. Little has synthesised P3EHS, an analogue to P3HT, where the Sulfur atom was substituted with Selenium. Here, the alkyl side-chains have been replaced by branched 2-ethylhexyl groups to ensure good solubility in THF.

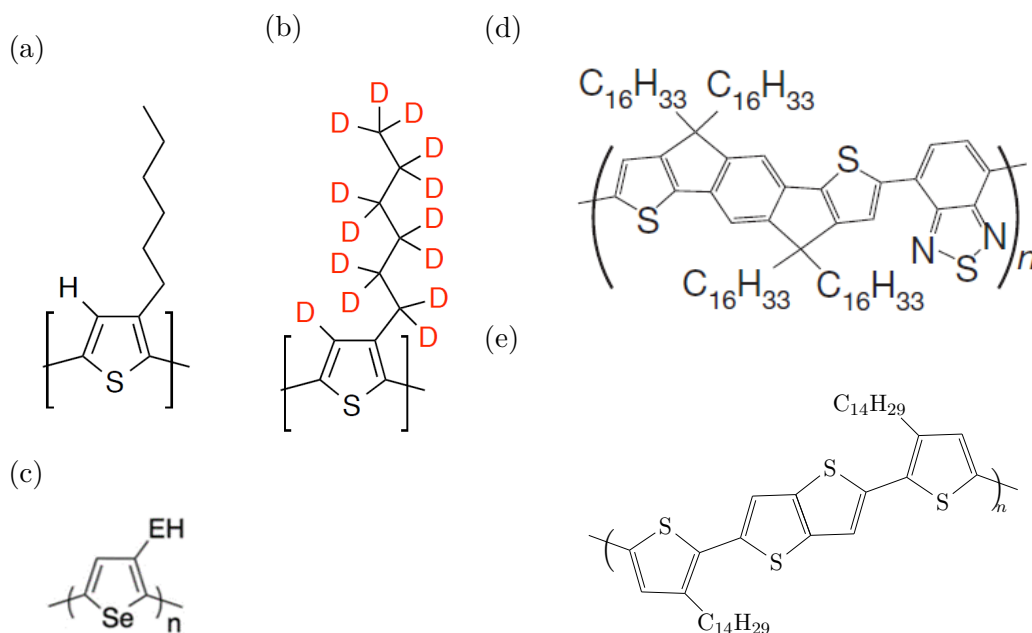


Fig. 3.4 Chemical structure of (a) P3HT, (b) deuterated P3HT (c) P3EHS, (d) IDT-BT and (e) PBTTT.

PBTTT

Previous studies of spin pumping in OSCs a trilayer structure were performed on poly(2,5-bis(3-alkylthiophene-2-yl)thieno[3,2-b]thiophene) (PBTTT, chemical structure shown in figure 3.4e) [12]. The morphology of PBTTT is more ordered than P3HT resulting in superior electronic performance [119]. Unfortunately, this polymer is not soluble in Tetrahydrofuran, which is the solvent used for the linewidth broadening studies, even with longer side-chains. Nevertheless, PBTTT has been investigated in the thermal spin injection experiments.

IDT-BT

Another commonly used polymer in the field of organic electronics is indacenodithiophene–benzothiadiazole (IDT-BT). It is a highly soluble, high mobility donor-acceptor type copolymer, which shows stable performance in ambient conditions [6]. In contrast to P3HT, the structure of the material is nearly amorphous. A more detailed discussion of the structural properties will follow in section 6.1. The HOMO of IDT-BT lies at ~ -5.3 eV, which is significantly lower than in P3HT. This implies that it cannot be doped as efficiently with oxygen resulting in a lower number of charge carriers [120].

Doping with F₄-TCNQ

A common stable dopant for small molecules and polymers is 2,3,5,6-tetrafluoro-7,7,8,8-tetracyanoquinodimethane (F₄-TCNQ, chemical structure shown in the inset of figure 3.5a) [121]. Due to its high electron affinity of 5.24 eV, F₄-TCNQ can act as an electron acceptor. Consequently, it can efficiently *p*-dope OSCs and increase the conductivity by several orders of magnitude. A schematic of the relative energy levels of P3HT and F₄-TCNQ is shown in figure 3.5a. The alignment of the HOMO of P3HT with the LUMO of F₄-TCNQ allows electrons to completely transfer from P3HT to the acceptor F₄-TCNQ, where they remain strongly localised. The associated holes in P3HT are either Coulombically bound to the F₄-TCNQ anion or move freely in the P3HT polymer.

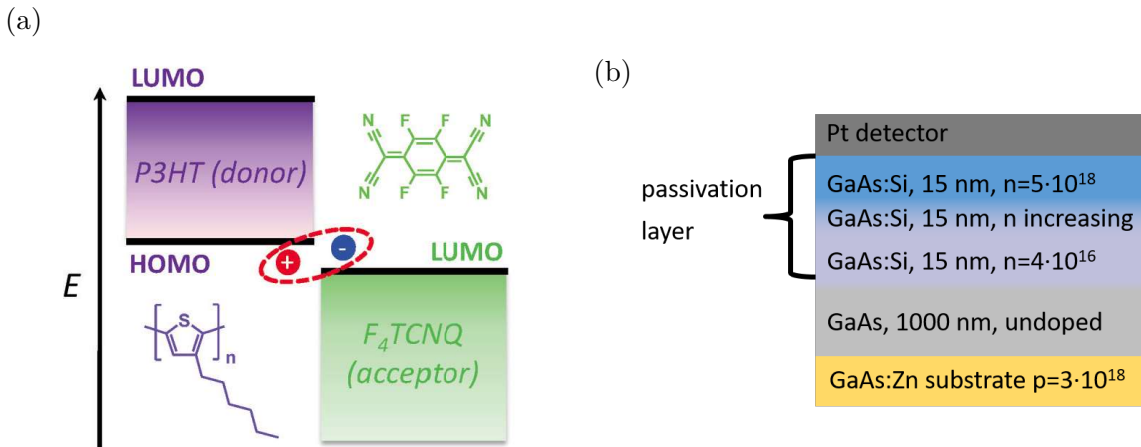


Fig. 3.5 (a) Schematic of the energetics of doping P3HT with F₄-TCNQ (reproduced from [121]). The insets show the chemical structure of P3HT (purple) and F₄-TCNQ (green) (b) Structure of the GaAs substrate. The intrinsic GaAs is sandwiched between a *p*-doped substrate and a *n*-doped passivation layer at the surface

In this work, the small molecule and polymer films have been doped with F₄-TCNQ dispersed in an orthogonal solvent following the recipe of Fujimoto *et al.* [122]. For this, the small molecule (polymer) films were immersed in a solution of F₄-TCNQ in Acetonitrile (ACN) at a concentration of 2 mg/ml for 2 minutes (30 minutes) and subsequently annealed at 70°C (80°C) for 20 minutes in a nitrogen atmosphere. These recipes were previously developed in our group. For this, the time for which the OSC films are dispersed in the orthogonal solvent had to be optimised to ensure maximum penetration of the dopant into the OSC while still retaining the original structure.

3.1.3 Metallic spin sink materials

There have been many studies on spin-to-charge conversion in heavy metals. Often the spin Hall angle is determined in spin pumping experiments, in which a pure spin current is injected from an FM into the NM layer. The spin-mixing conductance and spin Hall angle of the NM can be determined either by the increase in damping or by measuring the inverse spin Hall effect voltage. The spin Hall angle θ_{SH} largely varies as Z^4 , where Z denotes the atomic number of the NM material [123]. Platinum is a heavy element and highly unreactive, making it an ideal spin sink layer.

Additional heavy metals have been studied as spin sink layers, and the Z^4 dependence of the spin Hall angle has been verified [123, 124, 125]. The values of the extracted spin Hall angle for the metallic spin-sink materials studied in this work are listed below.

Table 3.2 Spin Hall angle of several metallic spin-sink layers extracted from literature

	Platinum	Gold	Palladium	Chromium
θ_{SH}	0.10 ± 0.01	0.084 ± 0.007	0.01	-0.051 ± 0.005

3.1.4 GaAs

Gallium Arsenide (GaAs) is a III-V semiconductor with a direct bandgap and adopts a Zink-blende crystal structure. A schematic of the doping profile of the sample is shown in figure 3.5b. As described in section 2.3.4, charge carrier can be spin polarised in intrinsic GaAs with circularly polarised light. The intrinsic GaAs layer is sandwiched between a Silicon (Si) doped and a zinc (Zn) doped layer. The p -doped substrate serves as a back-contact for the photodiode by extracting the photoexcited holes from the intrinsic GaAs. The n -doped layer at the surface acts as a passivation layer, which prevents spin decoherence at the interface due to surface traps. By applying a bias voltage between the back-contact and the Pt detector, the electrons are injected into platinum creating an out-of-plane spin polarisation.

3.2 Common sample fabrication techniques

There are several common fabrication techniques, which have been used for sample fabrication throughout this work. The standard procedures are discussed in the following sections.

3.2.1 Substrate cleaning

It is crucial that the interface between a substrate and any film deposited on top is cleaned thoroughly before deposition to allow coupling across the interface and ensure good quality of the film. The common cleaning procedure is as follows:

1. 10 min ultrasonic bath in Acetone
2. 10 min ultrasonic bath in Isopropyl Alcohol (IPA)
3. 10 min Oxygen plasma at 250 W

3.2.2 Photo-lithography

A common technique for patterning structures on a substrate is photolithography. For this, thin films of lift-off resist and a UV-sensitive resist are deposited on the substrate. The sample is then exposed to UV-light through a mask and the UV-sensitive resist is cross-linked in the exposed areas, which are removed by developing the sample. The undercut in the bi-layer resist allows for higher resolution down to around $2\ \mu\text{m}$ and expedites removal after the patterning process. In the last step, the desired layer is deposited, and the remaining resist stripped off. The details of the process are as follows:

1. Common substrate cleaning procedure
2. Lift-off resist LOR B:
 - Spin-coat at 6000 rpm for 40 s
 - Anneal at 180°C for 5 min
3. Photo-resist S1813:
 - Spin-coat at 6000 rpm for 40 s
 - Anneal at 120°C for 2 min
4. Expose desired areas to UV light for 12 s through photo-mask
5. Develop in MF319 for 35-45 s
6. Deposit Material
7. Lift-off in 1-methyl-2-pyrrolidone (NMP) overnight

3.2.3 Electron-beam lithography on insulating substrates

The minimum dimensions we can resolve with photo-lithography are set by the wavelength of the UV-light. When we have to write smaller structures, we have to resort to other means of patterning. A highly developed tool for this is electron-beam (e-beam) lithography, which allows resolving structures on the nanometre scale. When doing e-beam lithography on insulating substrates, a conductive layer has to be deposited as a discharge layer on top of the resist. Here, we use a thin layer of Au, which can be etched after exposure without interfering with the pattern in the resist. The general procedure for e-beam lithography is described in the following:

1. Usual substrate cleaning procedure
2. E-beam resist: 495 PMMA A8
 - Spin-coat at 6000 rpm for 30 s
 - Anneal at 180°C for 5 min
3. Thermally evaporate 6 nm of Au
4. Expose the desired area using Crestec CABL-2000 electron beam lithography system
5. Dip in Au etchant for 10 s and rinse with DI-water
6. Develop in IPA:MIBK (3:1) solution for 30 s and rinse in IPA for 30 s
7. Deposit Material
8. Lift-off in Acetone overnight

3.3 Linewidth broadening experiments

3.3.1 Samples for linewidth broadening experiments

The material and dimensions of the substrates for the linewidth broadening experiments were determined by the properties of the electron spin resonance (ESR) setup. As Silicon substrates are conductive, they absorb microwave magnetic fields considerably, and thereby lower the quality factor of the cavity significantly. Consequently, we have used borosilicate thin glass substrates (D263 T, purchased from Präzisions Glas & Optik GmbH) with a thickness of 0.4 mm for the LWB measurements. The dimensions

of the substrate were set to $3 \text{ mm} \times 5 \text{ mm}$, in order to comply with the inner diameter of the sample tube (3.2 mm).

In order to have a well-defined area of the magnetic film and ensure that it is within the uniform magnetic field and minimum of the electric field, the permalloy film has been patterned by a shadow-mask to a square with a side length of 2 mm. An illustration of the sample is shown in figure 3.6a. During the thermal evaporation of permalloy, maintaining a rate of 0.3 nm/s is crucial to ensure the correct composition of 81% Nickel and 19% Iron in the magnetic film. As the broadening of the linewidth is inversely proportional to the thickness of the magnetic film, we want to minimise the film thickness while maintaining reliable and reproducible magnetic characteristics. We have found a film thickness of 9 nm to satisfy both criteria well.

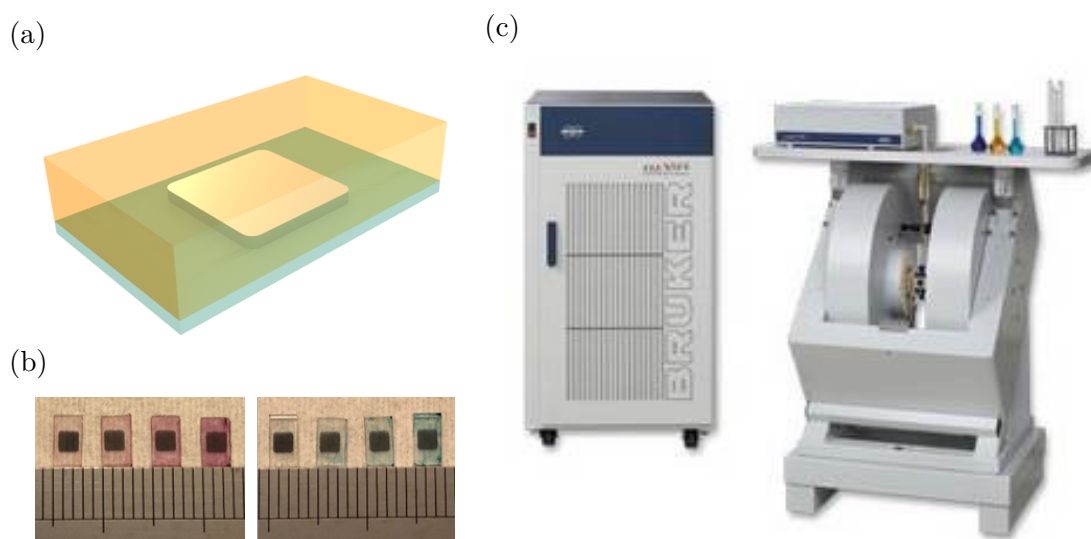


Fig. 3.6 (a) Illustration of a sample used for LWB experiments. A $2 \text{ mm} \times 2 \text{ mm}$ box of permalloy (shown in metallic grey) is deposited on a glass substrate (blue layer). Organic semiconductors (orange) are then deposited on the entire substrate. (b) LWB samples with different thickness of the P3HT (left) and IDT-BT (right) films. (c) Picture of the ESR setup (taken from Bruker manual)

Depending on the organic materials, we used three different methods of depositing the NM layers on the substrates. The processing of the OSC was conducted inside a glovebox under nitrogen atmosphere. The preferred method of deposition for small molecules is thermal evaporation in vacuum, as this does not influence the magnetic properties of the substrates. The OSCs were evaporated at a rate of 0.2 \AA/s by Dr Guillaume Schweicher in an evaporator dedicated to organic materials, which was cleaned thoroughly before every evaporation to avoid cross-contamination. We have

used this method for studying spin injection into three derivatives of DNNT.

For the processing of the small molecules discussed in this work, apart from the derivatives of DNNT, the method of drop-casting has been used. For this, the small molecule is dissolved in tetrahydrofuran (THF) at a concentration of 5 mg/ml. A droplet of 4 μ l solution is deposited on the substrate and let to dry. The sample is annealed in vacuum for 5 min to remove excess solvent from the film.

The third way of depositing a thin film of an OSC is to spin-coat from a solution. When the parameters of spin-coating and the amount of solution are fixed during processing, the thickness of the film depends linearly on the concentration of the solution [126]. Hence, in order to control the thickness and uniformity of the organic films, the polymers discussed in section 3.1.2 have been spin-coated. Solutions with a concentration of 0.5, 1, 1.5 and 2 mg/ml of the polymers in THF were spun on the substrates at 5000 rpm for 60 s. The samples with IDT-BT were dried at 45°C for 5 min. The films of P3HT were annealed at 110°C for 30 min to allow reorientation of the polymer chains into a favourable structure. The difference in film thickness with concentration of the polymer solutions is shown in figure 3.6b for P3HT and IDT-BT.

The samples for the structural and energetic characterisation measurements were fabricated alongside with the samples for the linewidth broadening experiment. For these measurements, the substrates were required to be of the size 15 mm \times 15 mm, and the magnetic films were not patterned but deposited on the entire glass substrate.

3.3.2 Electron spin resonance setup and linewidth broadening measurement

In order to measure the FMR absorption accurately, the spectra have been recorded with a Bruker E500 X-band spectrometer with a microwave cavity (Bruker ER 4122SHQE). A picture of the setup is shown in figure 3.6c. The microwave frequency was tuned to the resonance of the cavity at \sim 9.4 GHz. The standing waves inside the microwave cavity provide the AC magnetic field exciting the magnetisation precession while the electromagnet supplies the external magnetic field. Additional coils are used to modulate the external magnetic field at a frequency of 100 kHz. Measuring the lock-in signal with reference to the modulation of the external magnetic field results in a Lorentzian derivative signal around FMR. The exact settings for the measurements are discussed in section 4.1.

At first, the samples with pristine magnetic films were fixed on a Teflon sample holder, which ensured precise and reproducible positioning of the sample, and inserted into a quartz glass tube. The tube was then lowered into the cavity. In-plane orientation of the magnetic field was ensured by rotating the sample to a position where the resonance field H_{FMR} was minimised. After recording the FMR signal, the sample was removed from the substrate holder. Subsequently, the organic films were deposited on the magnetic substrates and the FMR spectra re-recorded. There is some heat dissipation during FMR due to phonons in Py. An additional organic layer will alter this power dissipation. However, given the low magnetoelastic coupling and small intrinsic Gilbert damping of Py, this effect is negligible.

The linewidth ΔH and resonance field H_{FMR} were extracted by fitting a Lorentzian derivative to the obtained data, and the change in damping was determined for each sample. The fitting function is given by the derivative of a symmetric and anti-symmetric Lorentzian (cf. equation 2.12):

$$dL/dH = \bar{S} \frac{(H - H_{FMR})\Delta H^2}{((H - H_{FMR})^2 + \Delta H^2)^2} + \bar{A} \frac{\Delta H((H - H_{FMR})^2 - \Delta H^2)}{((H - H_{FMR})^2 + \Delta H^2)^2} + \bar{C}, \quad (3.2)$$

where \bar{S} , \bar{A} and \bar{C} denote fitting constants.

When the thickness of the NM is smaller or on the same order of the spin diffusion length of the NM, the backflow of spin affects linewidth broadening. The gradual increase of the change in linewidth as a function of thickness of the NM has been described theoretically in equation 2.18. In order to simplify the extraction of the saturated change in linewidth $\delta\Delta H_{sat}$ in the limit of large thickness, we have rewritten this expression as

$$\delta\Delta H(t_{NM}) = \delta\Delta H_{sat} \frac{1 + \xi}{1 + \xi/\tanh(t_{NM}/\lambda_{SD})}, \quad (3.3)$$

where ξ denotes a material dependent fitting parameter. Using this function, we can fit our obtained data and extract the saturation value of the linewidth broadening $\delta\Delta H_{sat}$ and the spin diffusion length λ_{SD} .

As the linewidth of permalloy can vary considerably between substrates, the experimental procedure requires recording the absorption spectrum for each sample before and after the deposition of the OSC. In order to increase accuracy and to get an estimate of the error in the measurement, the results of multiple samples (at least four) were averaged after renormalising the change in linewidth to a linewidth of the

pristine permalloy film of $\Delta H = 21$ G. The marginally varying conditions for the thermal evaporation of permalloy and the exposure of the samples to air during the ESR measurements can cause slight differences in spin injection properties between different batches of substrates. In order to account for these differences and to make an accurate comparison between the different materials we have studied in this work, we have normalised the obtained data in the following way.

The thickness dependence was recorded on one batch of substrates for each material. Using the fitting to equation 3.3 as described above we have determined the saturation values of the linewidth broadening $\delta\Delta H_{sat}$ and spin diffusion length λ_{SD} for the three materials. The relative magnitude of the linewidth broadening of the derivatives of DNTT has been measured on one separate batch of permalloy substrates. For this, the thickness of the OSC was chosen to be 75 nm, which is significantly larger than the spin diffusion lengths we extracted. The data for the thickness dependence has then been adapted by renormalising the saturation values of $\delta\Delta H_{sat}$ with the relative magnitudes from the comparative measurement.

3.4 Thermal spin injection experiments

3.4.1 Spin Seebeck effect samples

The choice of material for measuring the SSE is crucial. In order to exclude any contributions from different effects, such as the conventional Seebeck or Nernst effect, from the ferromagnetic material, it has to be electrically insulating. YIG is a good candidate as it has a low magnetisation damping and a very low coercive field [127]. As the non-magnetic material is used for detecting the spin current via the ISHE, a sizeable spin-Hall angle and resistivity are favourable for the material. Therefore, heavy metals with strong SOC, such as platinum, are ideal candidates.

Bilayer samples

In order to test and compare the newly built set-up, the first samples were simple YIG/ Pt bilayer structures. YIG samples of a size of about 5×5 mm² were cut out using a mechanical scribe. A clean interface between YIG and platinum is crucial for measuring the SSE [128, 129]. Therefore, the samples have to be cleaned very carefully. First, the samples were cleaned with Acetone and IPA for 10 minutes each in a sonication bath. This was followed by treatment with oxygen plasma for 10 minutes. In order to ensure that no organic components remain on the surface of YIG and

to remove the magnetic dead-layer on the surface of YIG, the samples were etched with piranha ($\text{H}_2\text{SO}_4:\text{H}_2\text{O}_2$ in a ratio of 7:3), rinsed with deionised water and the oxygen plasma treatment was repeated. Subsequently, a 5 nm layer of platinum was sputtered on to the YIG samples. Apart from platinum, bilayer devices with a 5 nm thick layer of palladium and chromium, which can both be thermally evaporated, have been fabricated.

Trilayer samples with an organic semiconductor

In contrast to the straightforward sample fabrication of bilayer samples, it is much more complicated when organic semiconductors are involved. The basic idea is to fabricate a trilayer device with YIG as the source of spin current, an OSC into which the spin current is injected and a normal metal layer on top of the OSC, where the propagated spin current is converted to an electromotive force using the ISHE. A schematic of this structure is shown in figure 3.7a.

Unlike many inorganic materials, organic semiconductors are relatively soft. This poses a problem for the deposition of the top metallic layer, which generally has to be either thermally evaporated or sputtered. Platinum in particular usually has to be sputtered. The high energy of the individual atoms during these deposition methods cause them to penetrate into the organic layer. This can give rise to pinholes or even complete penetration through the entire organic film and a dead layer at the interface between the OSC and the metallic film. It is, however, crucial to have a clean and well-defined interface for efficient spin current transmission [130].

Despite being aware of the possible complications with the OSC and metal interface, the first try was to straightforwardly fabricate trilayer devices by spin-coating the organic material onto YIG and sputtering Pt on top. The two polymers P3HT and PBTTT were selected for this experiment as previous spin pumping experiments have been successful with these materials [12, 131].

In the first step, the YIG samples were cleaned as described in the previous section. The OSCs were then spin-coated from a solution in 1,2-Dichlorobenzene (DCB) at a concentration of 10 mg/ml in air using different spinning speed, varying from 3000 rpm to 5000 rpm, which corresponds to a film thickness of approximately 30 nm to 60 nm. The samples with PBTTT and P3HT were annealed in a nitrogen atmosphere for 20 minutes at 180°C and 110°C respectively. The metal layer was then deposited following the same procedure as for the bilayer samples.

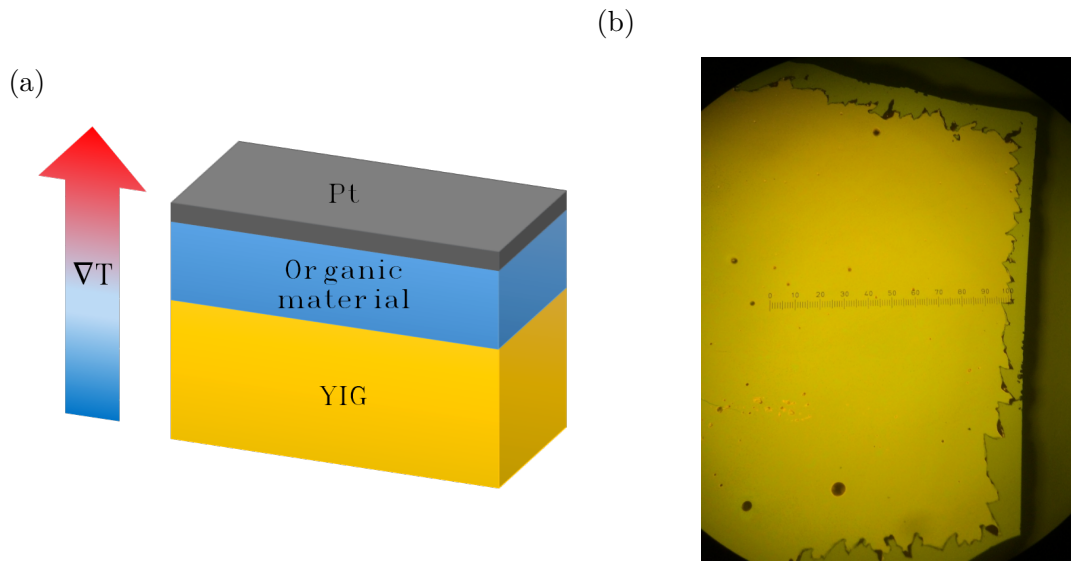


Fig. 3.7 (a) Trilayer structure for SSE devices with an organic semiconductor layer between YIG and platinum. (b) Microscope image of a transferred CYTOP/Pt/P3HT film (bright yellow) on a YIG substrate (grey substrate, approximately $4 \times 4 \text{ mm}^2$).

An additional method of device fabrication has been tested in order to improve the interface between the OSC and the top metal layer. For this, the metal layer and afterwards the OSC were deposited on a separate substrate and only then brought into contact with YIG. This method was developed by Prof L. Jiang. The general idea is to delaminate platinum with the OSC from a substrate and place the freestanding film on to YIG. For this, first, the Si/SiO₂ substrates had to be modified using an octadecyltrichlorosilane (OTS) treatment of the surface. CYTOP was spin-coated at 2000 rpm on to the substrates in a nitrogen atmosphere. The OTS treatment leads to poor adhesion of the CYTOP film to the substrate. Platinum and subsequently the OSC were deposited on top of the CYTOP film. Using a plastic mask, the entire film was peeled off from the substrate and transferred to a cleaned YIG sample (approximately $4 \times 4 \text{ mm}^2$). Using sharp tweezers, the film was carefully detached from the mask at the edges of the YIG substrate. Due to electrostatic forces, the film adheres to YIG, which ensures good contact between the OSC and YIG. A successfully transferred CYTOP/Pt/P3HT on YIG is shown in figure 3.7b.

3.4.2 Thermal spin injection setup and measurement

Spin Seebeck effect setup

The general idea is to simultaneously apply a temperature gradient perpendicular to the interface of the sample and an in-plane magnetic field. The difference in voltage due to the SSE, which is perpendicular to the direction of the magnetic field, can then be measured. Several different techniques have been shown to be successful. K. Uchida *et al.* [71] use a Peltier element and a heat bath to induce a temperature gradient, as shown in figure 3.8a. B. Youssef *et al.* [127] patterned the detection layer into a Hall bar shape on top of the ferromagnetic insulator. The structure was then covered with an insulating layer of Al_2O_3 and a platinum stripe heater deposited on top. An image of a sample is shown in figure 3.8b. The detection layer in the sample in the work of M. Schreier *et al.* [132] consists of a Hall bar structure as well. However, they use the same Hall bar as the heater simultaneously and measure the SSE voltage perpendicularly with a lock-in amplifier. A schematic of this sample structure is shown in figure 3.8c. A completely different way was introduced by M. Weiler *et al.* [133]. Here, a laser beam is used to locally heat up the structure, as shown in figure 3.8d.

It is not straightforward to compare these different methods quantitatively. The sample geometry, most importantly the distance between the voltage probing points, and layer thickness of the FMI and metal influence the signal strength. However, the main problem lies in the determination of the magnitude of the temperature gradient across the sample. While the setup by K. Uchida *et al.* allows the temperature to be measured using thermocouples, the temperature can only be estimated from simulations in the other experiments. Even though the absolute SSE voltage cannot be compared, studying the voltage normalised by the saturation voltage allows investigating the noise level of the different techniques. From a comparative study by M. Schreier *et al.* [75], it is apparent that the noise to signal ratio is the smallest using the setup described by K. Uchida in the group of Prof E. Saitoh at the Tohoku University in Sendai, Japan. Additionally, the comparably straightforward setup requires only a very simple layer structure of the samples. For these reasons, we decided to design our system based on this setup.

A schematic of the first version of the new setup for SSE measurements is shown in figure 3.9. The sample is placed on top of a Peltier element, which allows to either heat or cool one side of the sample. The Peltier element (2.9 W, ET-017-08-15-RS) is connected to a power source (Keithley 2200-30-5). Using two T-type thermocouples

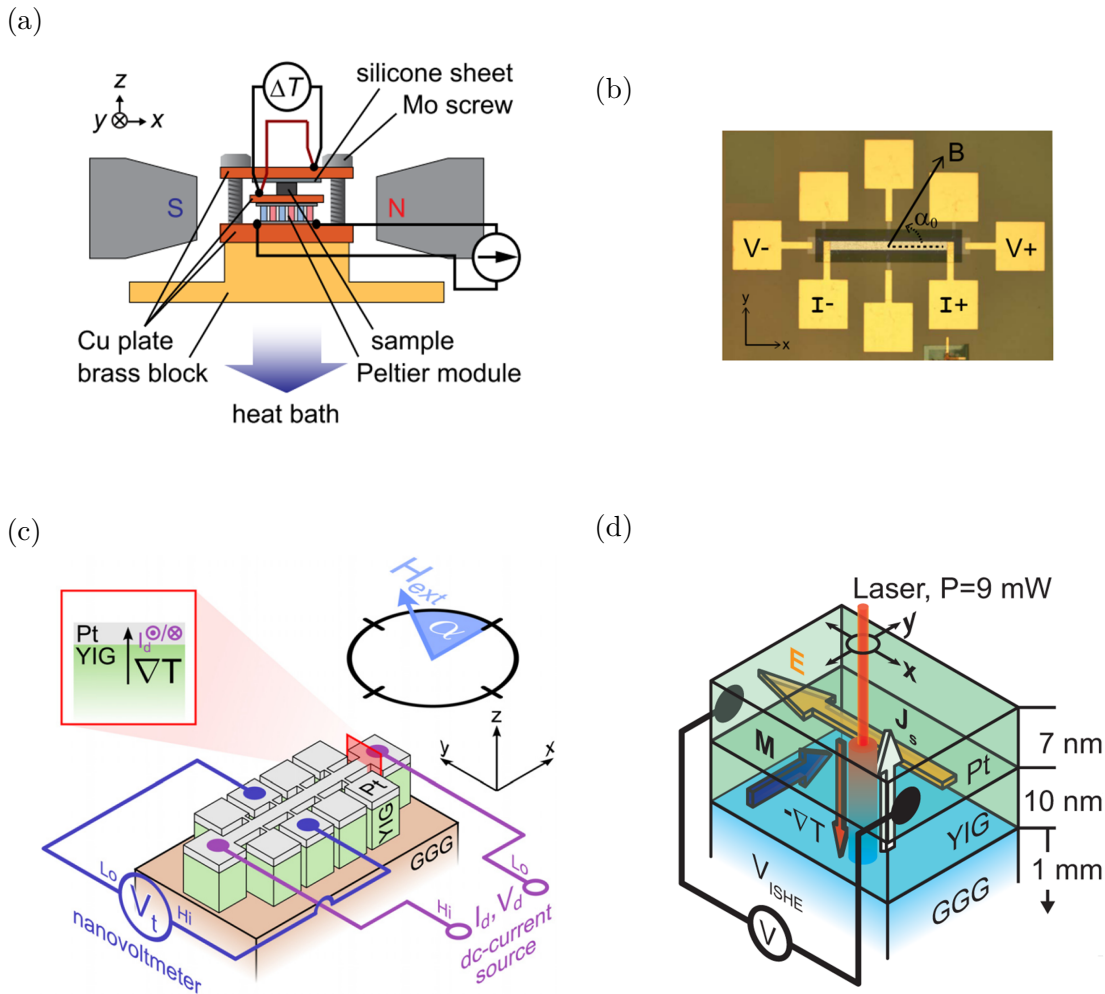


Fig. 3.8 (a) Schematic illustration of the SSE setup by K. Uchida *et al.* using a Peltier element to create the temperature gradient (from [71]) (b) Image of the sample used by B. Youssef *et al.* The outer pads, labelled with V_- and V_+ , are connected to the underlying Pt Hall-bar. The darker square is the insulating layer, and a Pt heater is patterned on top (from [127]). (c) Coincident SEE detector Hall bar and heater designed and used by Schreier *et al.* (from [132]) (d) Schematic of how a laser beam is used to generate a local temperature gradient (Weiler *et al.*, from [133]).

connected to a thermocouple monitor (Stanford Research SR630), the temperature on either side of the sample is measured. The SSE voltage across the sample is then measured perpendicular to the external magnetic field with a nanovoltmeter (Keithley 2182A). The magnetic field is generated by an electromagnet (GMW 3472-70), which is powered using a bipolar power supply (Kepco BOP-20-20ML).

First, a probe head had to be designed and manufactured. The CAD drawings for the first version of the sample holder are shown in figure 3.10. The exterior material

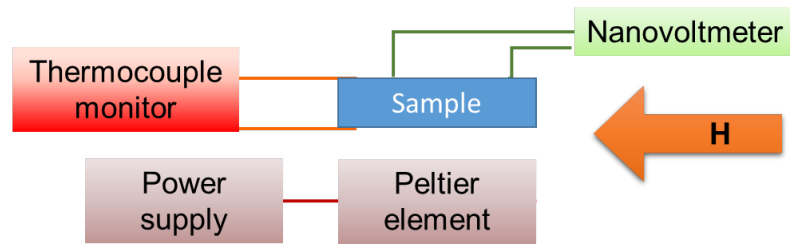
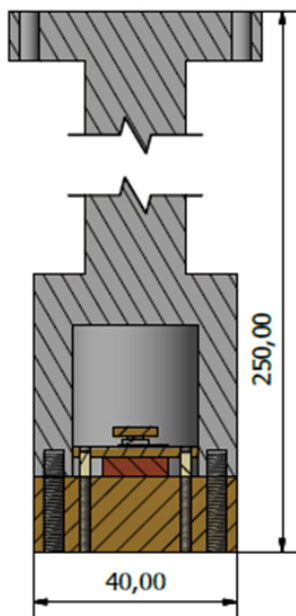


Fig. 3.9 Schematic of the first version of the new SSE setup. An electromagnet generates an in-plane magnetic field H . The temperature difference across the sample is applied with a Peltier element and measured with two thermocouples. The SSE voltage is then measured with a nanovoltmeter.

(a)



(b)

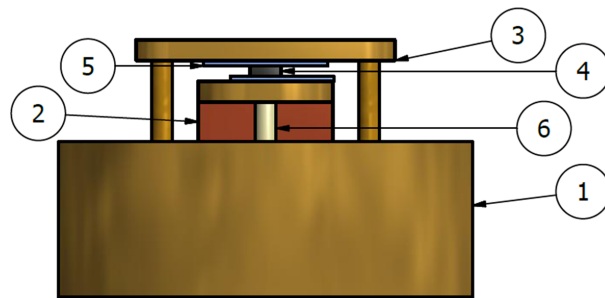


Fig. 3.10 CAD drawings of the probe head (a) cross section of the entire sample holder (lengths are indicated in mm). (b) First version of the sample stage. 1: brass cylinder acting as thermal bath 2: Peltier element 3: brass plate 4: sample 5: sapphire plate for electrical and magnetic insulation 6: plastic screws for thermal insulation of the brass plate from the brass cylinder.

of the cap, which is covering the sample space, was chosen to be made out of Teflon. The reason for this is that this would allow the probe head to be rotated between the pole caps of the electromagnet while being in touch with them. This way, it was made sure that the sample would always be positioned exactly in the middle of the field. A more detailed sketch of the sample chuck area is shown in figure 3.10b. The base of the probe head (1) acts as a thermal bath for the Peltier element (2) and is thus made

of a big brass cylinder. The Peltier element is clamped between this brass cylinder and a thin brass plate. This plate ensures a uniform temperature across the surface and gives enough space to attach a thermocouple for measuring the bottom sample temperature. For electrical and magnetic insulation the sample is placed in between two thin ($10 \times 10 \times 0.5 \text{ mm}^3$) sapphire plates (5) on top of the brass plate. In this configuration, the sample is placed face-up, which means that the FMI/substrate is on the bottom. Originally, it was planned to have another brass plate on top of the sample, in which two spring-loaded contacts and a thermocouple would be embedded. Out of practical reasons, mainly due to electrical insulation, we decided, however, to switch to a plastic top (shown in figure 3.11a). In order to measure the upper sample temperature, a thermocouple was attached to a copper wire which sits in the middle of the two spring-loaded contacts. These contacts are connected to the nanovoltmeter for measuring the SSE voltage across the sample. The plastic top can be slid on top of the sample, guided by metal rails. It is fixed with a weight on top. The inside of the finished first version of the probe head is shown in figure 3.11a. Figure 3.11b shows the sample holder fixed on a rotation stage on a metal frame inside the electromagnet.

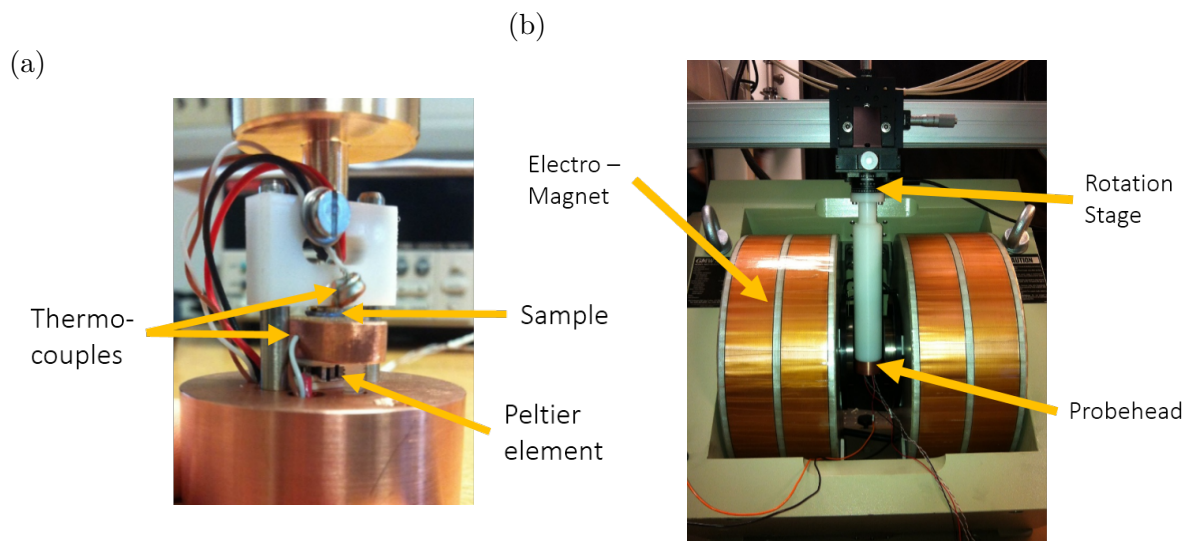


Fig. 3.11 (a) Interior of the first version of the probe head for the spin Seebeck measurements. The white plastic top can be slid on to the sample along the metal guides. It has two embedded spring-loaded contacts for contacting the sample and holds a thermocouple. Once it is placed onto the sample, it is fixed in place with a weight on top (top metal block in the picture). (b) The probe head is mounted on a rotation stage in an electromagnet.

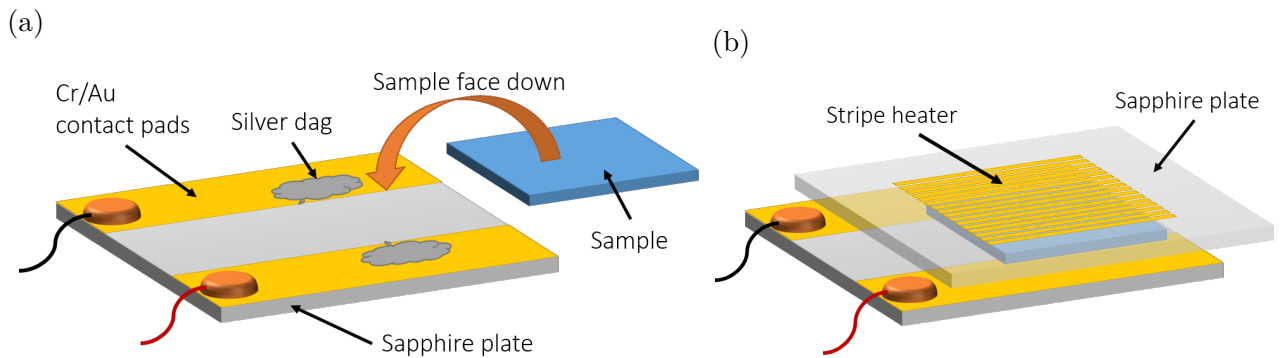


Fig. 3.12 (a) The sample was placed onto the metal leads face down. A small amount of silver dag was used to enhance the electrical contact between the metallic layer of the sample and the contact pads. (b) A Pt stripe heater was patterned on to a sapphire plate and placed on top of the sample to increase the temperature gradient.

With this setup, we could successfully measure the SSE effect in YIG/Pt devices. However, the maximal temperature gradient was only around 1 K. As the voltage signal depends linearly on the temperature difference, it is crucial to increase the temperature difference in order to enhance the voltage signal. For this, the probe head was modified in the following way as depicted in figure 3.12. Two Cr (5 nm)/ Au (120 nm) parallel metal tracks, separated by 4 mm, were thermally evaporated on to the bottom sapphire plate using a shadow mask. Two wires were fixed to the metal leads using silver dag and connected to the nanovoltmeter. Instead of contacting the sample with the spring-loaded contacts from the top, electrical contact was made by placing the sample upside down on to the metal leads on the sapphire plate. A small amount of silver dag was used to enhance the contact between the metallic layer of the sample and the tracks. In order to increase the temperature gradient, an additional heater was inserted on top of the sample. For this, a 50 nm Pt thick stripe heater has been sputtered onto a sapphire substrate using photo-lithography for patterning. The spring-loaded contacts were used to contact the top heater, which was connected to a power source (Keithley 236). With this modified probe head, a temperature difference of up to 40 K can be reached.

All instruments and the power supply for the magnet are connected to a computer using a GPIB interface and can be controlled remotely using LabView routines, which we developed while building the setup.

Spin Seebeck effect measurement

An in-plane magnetic field and a temperature gradient perpendicular to the interface of the sample have to be applied for measuring the spin Seebeck effect. As the SSE voltage follows the magnetisation of the ferromagnet, the fundamental measurement is to measure the inverse spin Hall effect voltage while sweeping the magnetic field between positive and negative saturation field at a fixed temperature difference. The magnitude of the SSE signal is then given by half of the voltage difference between positive and negative saturation field. The dependence of the SSE signal on several experimental parameters has been explored in this work.

3.5 Thermal spin detection experiments

Having discussed the thermal spin injection measurements in the previous subsection, we now turn to thermal spin detection. Here, we introduce experiments studying thermal spin-to-charge conversion. For this, we have tested two ways of creating a spin accumulation, spin pumping and optical spin injection.

3.5.1 Inverse spin Nernst effect with spin injection via spin pumping

Samples

The device design used in ANE measurements has proven to be a very sensitive architecture for detecting thermally driven, magnetisation dependent effects [134]. Therefore, the initial design for the ISNE samples was based on the ANE architecture. The ISNE signal is linear with the temperature gradient and is additive along the length of the sensing bar. For these reasons, we designed a long sensing bar with stripe heaters on both sides in near vicinity. The dimensions required are smaller than the minimal resolution of photolithography, which can go down to about $2\ \mu\text{m}$. Hence, we turned to electron beam (e-beam) lithography for patterning the devices.

The resist sensitivity is a substrate-dependent material property, which determines the dose timer for the exposure. In order to determine the optimum parameters for our material system, we performed a dose test. For this, we wrote two patterns, a square consisting of four triangles forming a diagonal cross with a gap of $1\ \mu\text{m}$ in the centre, which we commonly use as alignment markers, and three rectangles of $1\ \mu\text{m}$ width with a separation of $250\ \text{nm}$. After following the procedure described

above, a layer of 30 nm of Pt was deposited and the remaining resist was lift-off in Acetone. Four of these patterns are shown in figure 3.13 for different dose timers. The cross inside the square is resolved best in pattern A, which was written using a dose timer of 27 μs . The cross in B (36 μs) shows slight signs of overexposure, as the gap gets narrower towards the centre. In both, C (45 μs) and D (63 μs) the cross inside the square cannot be resolved anymore due to overexposure. The three rectangles could not be resolved at all with the dose timer used for pattern A, while being clear in both B and C, and also show signs of overexposure in D, as the gaps between the rectangles start to curve. Therefore, we are using a resist sensitivity of 350 $\mu\text{C}/\text{cm}^2$ for alignment markers and large patterns and 450 $\mu\text{C}/\text{cm}^2$ for narrow and long patterns.

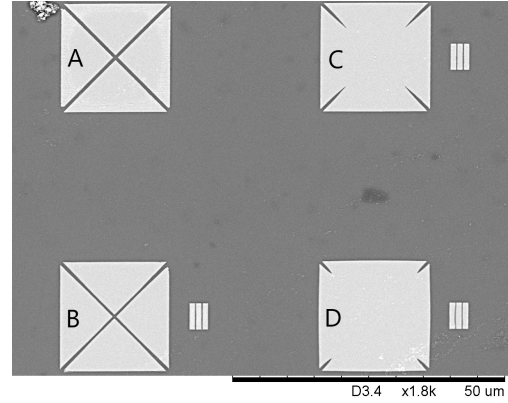


Fig. 3.13 SEM image of platinum markers on a YIG substrate patterned using electron beam lithography with different dose timer varying from 27 μs to 63 μs . Pattern A, B, C and D correspond to a resist sensitivity of 300, 400, 500, 700 $\mu\text{C}/\text{cm}^2$ respectively.

The design for the ISNE devices discussed in this work is shown in figure 3.14a. The substrate was a 5 μm thick YIG film (single-sided) grown on GGG by LPE, which was purchased from INNOVENT and cut into 5 mm \times 3 mm pieces. In addition to the usual cleaning procedure, the substrate was cleaned in Piranha solution for 10 min. Every substrate was composed of three devices. In the first step, a 25 nm film of platinum was deposited for the alignment markers (shown in blue). The alignment markers were designed to be at the corners of the devices and were used to align the subsequent patterns across different steps of lithography. In the second step, the platinum sensor (shown in green) was written with respect to the position of two of the alignment markers. The dimensions of the bar were set to 2 $\mu\text{m} \times$ 580 μm . It is crucial that the thickness of the layer of platinum for the sensor is on the order of the spin diffusion length, in order to measure a spin-dependent effect in this geometry. In order to have precise control of the layer thickness and reliable quality, a 3 nm layer of platinum was sputtered by S. Brennan at the Thin Film Magnetism Group of the Cavendish Laboratory. Proceeding the deposition of platinum, the substrate was cleaned in-situ in an Argon plasma for 1 min. In the last step, the contact leads to the sensor, the heaters

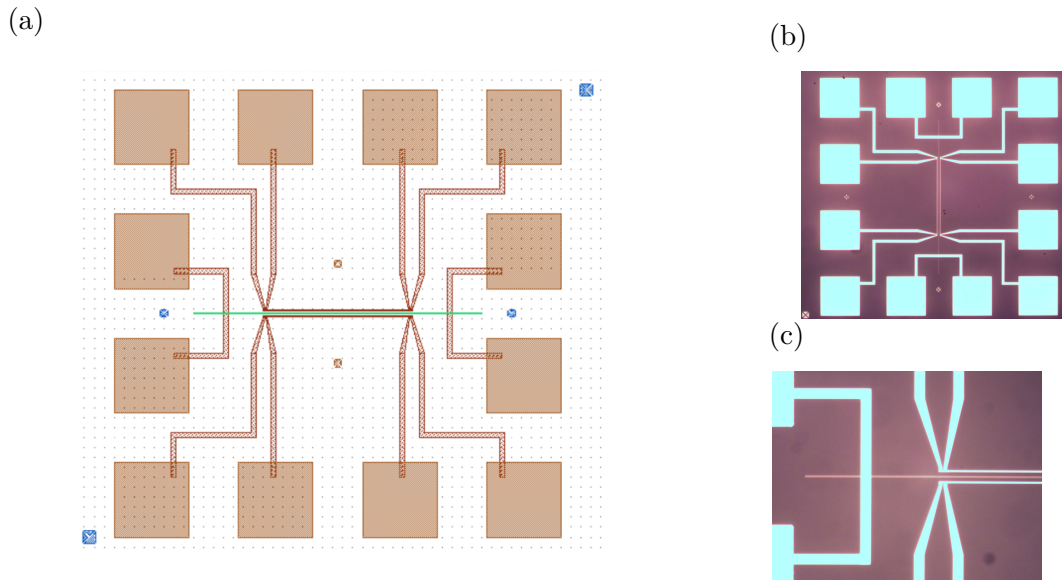


Fig. 3.14 (a) Design of an ISNE device. Alignment markers are drawn in blue, the Pt sensor in green and the heaters, contact leads to the sensor and contact pads in brown. The side length of the square contact pads is $150\ \mu\text{m}$. (b) Optical microscope image of the fabricated device. The patterned layers of platinum are shown in light blue on the YIG substrate (dark violet). (c) Magnified microscope image of half of the central region of the device, showing the platinum sensor between two heaters.

and the contact pads (shown in brown) were patterned. The strip heaters, which are parallel and to both sides of the sensor, are $1.5\ \mu\text{m}$ in width and $300\ \mu\text{m}$ long. They are contacted by two contact leads on each end. This four-point-probe configuration allows using the heaters as temperature sensors as well. In order to ensure low resistance of the contact leads and efficient heating, a $50\ \text{nm}$ layer of platinum was deposited. Optical microscope images of the fabricated devices are shown in figure 3.14.

Coplanar waveguide setup

Due to the spatial restrictions in the ESR, the sample size, as well as the number of connectors, is very limited. A common alternative setup for microwave excitation is making use of the field distribution in a coplanar waveguide (CPW). In a CPW, microwaves are transmitted through a stripline between two ground planes creating an in-plane AC magnetic field, which can excite FMR. An additional benefit of CPWs compared to the ESR is that the frequency can be varied. In order to facilitate simultaneous precise electrical measurements and microwave excitation, a new sample holder had to be fabricated. For this, a CPW was designed on an FR4-printed

circuit board (PCB) with integrated pads for electrically contacting the samples via wire-bonding.

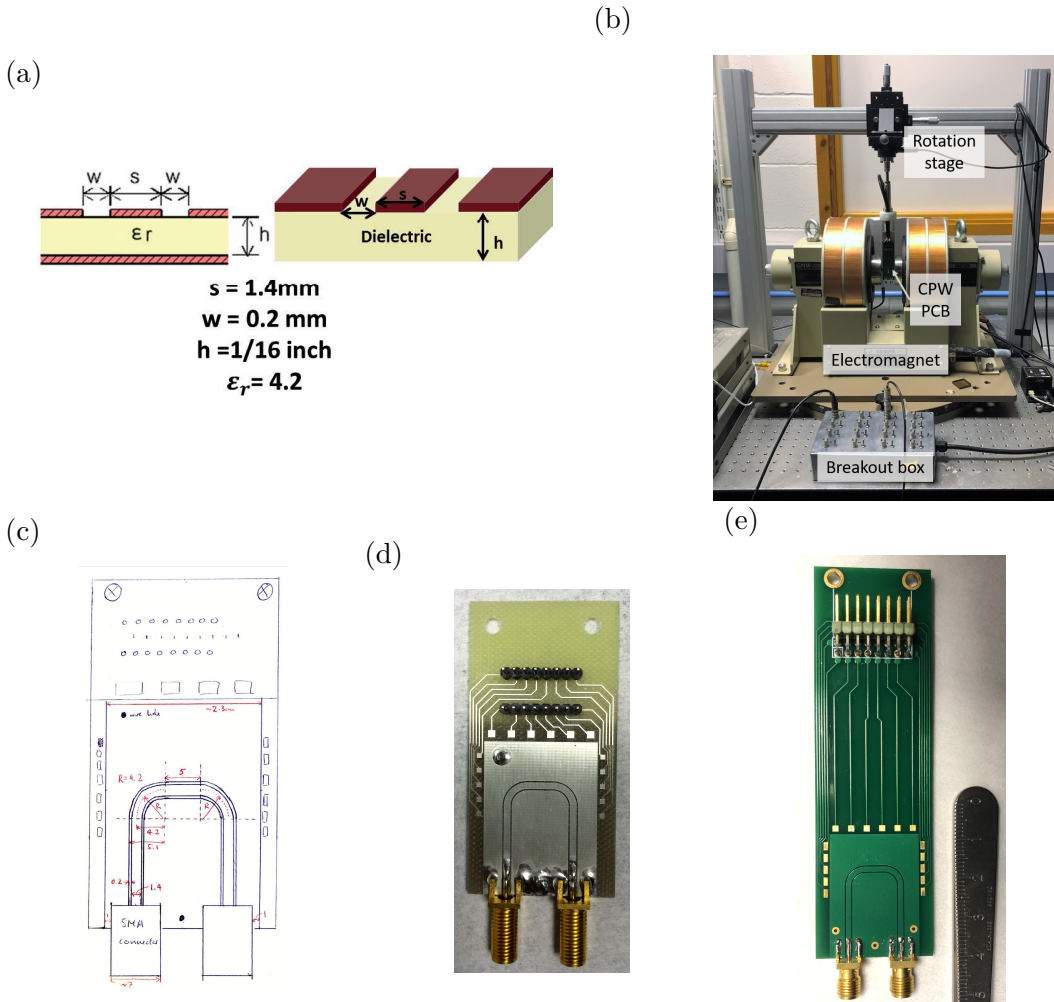


Fig. 3.15 (a) Schematic of the CPW design including dimensions (reproduced from [131]). (b) Picture of the electromagnet setup for spin pumping experiments. (c) Design of a PCB with an integrated stripline for microwave transmission. The dimensions are given in units of mm unless stated otherwise. The wire-bonding pads around the ground plane are electrically connected on the PCB with the circular connectors in the top section of the PCB. (d) Image of the first version of the PCB made according to the design. (e) Third and final version of the CPW with an elongated PCB to allow easier wire-bonding of the sample.

The dimensions of the fundamental CPW were taken from the predecessor CPW, which was designed by Dr K. Kang [131]. A schematic of the CPW including the exact measures is shown in figure 3.15a. The characteristic impedance of the waveguide was simulated to be $49.6\ \Omega$ with a near perfect transmission in the range between 2 GHz

and 18 GHz using AWR Design Environment. This characteristic impedance matches the output impedance of the microwave source of 50Ω , ensuring optimum transmission.

In order to fit the sample holder between the pole pieces of the electromagnet, the SMA connectors, which connect the microwave lines to the stripline, could not be placed on the sides of the PCB. Therefore, the stripline had to be bent such that the SMA connectors were edge-mounted to the PCB at the bottom as shown in the sketch in figure 3.15c. By choosing the bending radius R a factor of three larger than the width of the stripline, the microwave transmission should not be affected by the bending [135]. The ground plane around the stripline had to be large enough not to distort the field lines significantly such that a uniform AC microwave magnetic field is created in the central region of the CPW. Sixteen contact pads were placed around the ground plane. The pads can be electrically contacted from a break-out box via the connecting pins and a shielded cable to minimise electrical noise and allow high precision measurements. Indeed, it has been verified that electrical measurements on metallic samples can be conducted with picovolt accuracy using the final version of the CPW. The prototype of the CPW was manufactured in the workshop of the Cavendish Laboratory. A picture of the sample holder is shown in figure 3.15d. Several small alterations were made for the final design of the CPW. The space between the bonding pads and the connector was increased to allow more space for contacting the samples electrically via wire-bonding. In order to ensure a reliable connection between the cable and the connector pins on the PCB, a more robust connector was used. Furthermore, additional wire holes connecting the top and the bottom ground plane were introduced to improve the uniformity of the microwave magnetic field. Additionally, the CPW was coated with a thin insulating (green) layer to avoid spurious signals and shorting from direct electrical contact with the sample. Figure 3.15e shows a picture of the final CPW manufactured by PCBtrain.

The measurements towards the detection of the inverse spin Nernst effect were conducted using the CPW sample holder, which is described in the previous section, for the microwave excitation. The microwave source (Anritsu MG3692C signal generator) offers the possibility of chopping the microwaves with respect to an external trigger. The transmitted microwaves were converted into a voltage, which is proportional to the microwave power, with a diode (Anritsu 70KC50 detector) and an additional attenuator (Anritsu 43KC-10) connected ahead. This allowed recording the microwave absorption at FMR in homodyne electrical measurements. The external magnetic field was provided by an electromagnet (GMW 5403). Figure 3.16a shows a schematic of the measurement arrangement. The two heaters were grounded on one side and connected

to an alternating current source with diodes with opposite orientations. Therefore, one will only transmit current with positive polarity while the other only conducts current with negative polarity. Consequently, applying an AC heater current to the heaters in the diode configuration results in a sinusoidally varying in-plane temperature gradient between the heaters perpendicular to the sensing bar. The direction of the current flow was chosen such that the Oersted field created from the heaters was pointing in the same direction for both heaters. Thereby, the Oersted field is modulated at twice the frequency of the temperature gradient and hence can be excluded as a source of artefact. The voltage signal across the sensor bar was measured in double lock-in configuration (Stanford Research Systems SR830 DSP lock-in amplifier) with a low-noise preamplifier (Stanford Research Systems SR560) connected ahead. The first lock-in was recording the voltage signal with respect to the fast modulation of the microwaves. The output was then fed into the second lock-in, which measured the voltage with respect to the applied heater current. The first harmonic signal in the latter lock-in measurement depends linearly on the variation of temperature and, most importantly, on the in-plane component of the temperature gradient. This is therefore the ISNE signal we are aiming to observe. The second harmonic signal, on the other hand, does not depend on the in-plane temperature gradient but rather the out-of-plane gradient. Hence, we would expect to measure contributions from the SSE and the Oersted fields, as mentioned above, in this configuration.

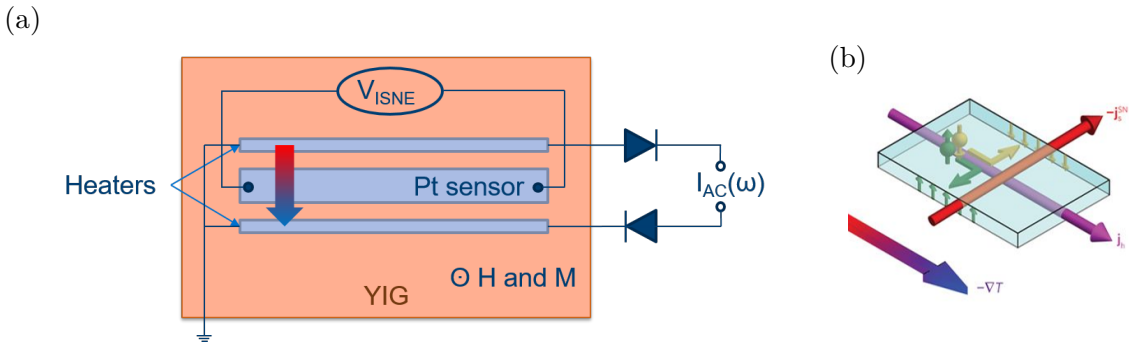


Fig. 3.16 (a) Schematic of the measurement towards detection of the ISNE. (b) Schematic of the spin Nernst effect (illustration adapted from [19]).

3.5.2 Inverse spin Nernst effect with optical spin injection

Samples

The design of the samples for the ISNE with optically created spin polarisation is based on the previously mentioned ISNE samples. Figure 3.17 shows a sketch of the central region of the sample. Compared to the previous ISNE samples for spin pumping, there are three main differences. As the GaAs substrate is conductive when excited with light, the heaters had to be electrically insulated from the substrate. For this, a 65 nm thick layer of aluminium oxide (shown in yellow) has been deposited via sputtering in a 10% oxygen and 90% argon environment in the regions underneath the heaters. The pattern was chosen slightly larger than the actual heaters to prevent leakage at the edges of the heaters. Furthermore, the distance between the two heaters was chosen to be significantly larger to avoid scattering and interference effects of the incident laser beam due to the reflection of the metallic and thus reflective heaters and ensure that the light is focused only on the central sensing bar. As the spin injection is localised to the beam spot, there is no benefit in increasing the length of the bar anymore. It was therefore chosen slightly larger than the distance between the heaters.

In addition to the aforementioned alterations, the *p*-doped layer had to be electrically contacted. For this, a 5 mm×5 mm contact pad was defined in the corner of the GaAs substrate with e-beam lithography and etched by 1200 nm in phosphoric acid (H₃PO₄)

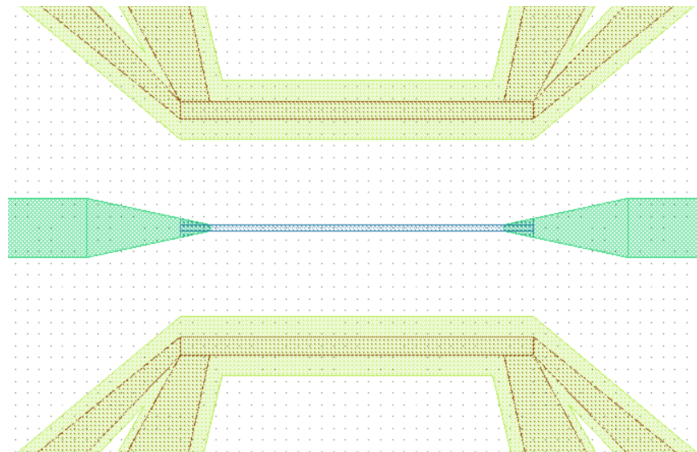


Fig. 3.17 Central part of the sample design for the ISNE with optical spin injection. The horizontal bar in the middle of the device is the platinum sensor (blue). The thicker platinum leads contacting the sensor are drawn in green. The heaters (brown) are electrically insulated from the GaAs substrate by an additional layer of aluminium oxide underneath, which is shown in yellow. The distance between the two heaters is 20 μm .

for 170 s. For the metallic contact, 20 nm chromium and subsequently 80 nm gold have been deposited.

Optical setup and measurement

The setup for the optical spin injection was designed and built by Dr R. Di Pietro, with whom these optical measurements have been performed. A schematic of the arrangement of the optical components is shown in figure 3.18a.

First, the unpolarised laser beam (at a wavelength of 810 nm) passes a polarising beam splitter, which sets the orientation of the transmitted linearly polarised light. This beam is then passed through a rotating $\lambda/2$ -waveplate. The retardation of the incident light depends on the angle of rotation α of the half-waveplate resulting in a rotation of the linearly polarised light by 2α . In order to enable phase sensitive lock-in measurements, a photoelastic modulator (PEM) at a frequency of 42 kHz was used as a quarter-wave plate. Linearly polarised light incident on a PEM can be decomposed into two components, one perpendicular and one parallel to its optical axis. Due to the birefringence of the PEM, the retardation of the two components is different. For the $\lambda/4$ -waveplate, the amplitude of the oscillation of the PEM is adjusted such that for linearly polarised light incident at an angle of 45° , one component is alternately retarded and advanced by 90° relative to the other. As a result, the exiting light is varying sinusoidally between circularly right and circularly left polarisation. Similarly, there is no relative retardation between the components when the incident light is parallel and perpendicular to the optical axis. Hence, the light remains linearly polarised.

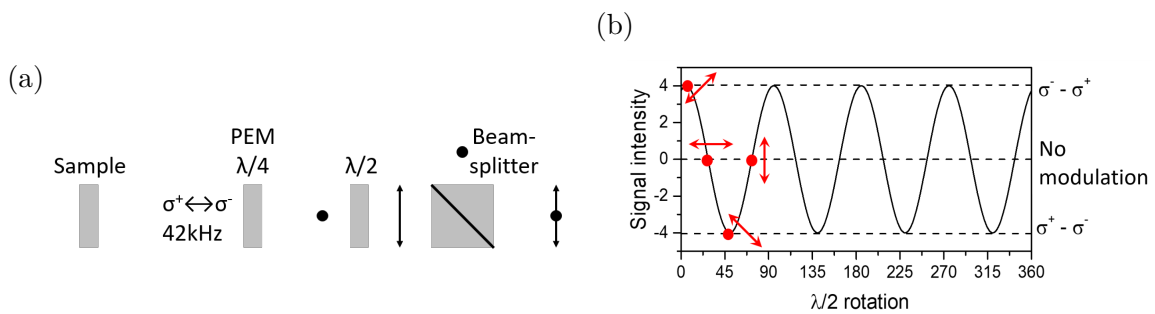


Fig. 3.18 (a) Sketch of the optical setup developed by Dr R. Di Pietro. (b) Expected signal intensity as a function of rotation angle of the $\lambda/2$ waveplate. The orientation of the incident linearly polarised light on the PEM with respect to its optical axis is indicated with red arrows (Illustrations made by Dr R. Di Pietro, used with permission).

The sample was mounted inside a cryostat (ARS closed cycle Helium cryocooler with optical windows). In order to minimise noise from thermal effects, the measurements were conducted at a temperature of ~ 20 K. A DC bias voltage was applied to the back-contact in the p -doped layer of GaAs with respect to one side of the platinum sensor, which was set to ground. In this photodiode configuration, photoexcited holes are extracted from the back-contact, while electrons are accelerated towards and injected into the platinum bar. The voltage across the bar was measured in a double lock-in configuration. The first modulation was given by the fast oscillation of the PEM. The alternating current in the diode configuration (as described in section ??) was set at a significantly lower frequency. The measurement can also be conducted with only one heater. In this configuration, the alternating current is sent directly to one heater, and the signal is recorded as a second harmonic of the current modulation. The drawback compared to the measurements with two heaters in the diode configuration is that contributions from the out-of-plane temperature gradient cannot be excluded straightforwardly making multiple symmetry checks necessary.

Figure 3.18b shows the expected signal intensity of spin-dependent effects. The maximum signal is expected when the light incident on the sample is purely circularly polarised. At -45° the oscillation between circularly left and right polarisation is phase shifted by π . Here, the minimum in signal reflects the dependence of the signal on the orientation of the spin. There is no signal expected for parallel or perpendicular light as there is no net spin polarisation of the photoexcited charge carriers without circularly polarised light.

There might be some contribution from spurious effects, which depend on linear polarisation, in the actual data from the experiment. Therefore, the obtained data has to be decomposed into components due to circular and linear polarisation. The exact angles of the half-wave plate at which circularly polarised light excites the sample have been determined in reference measurements. The fitting function is given by

$$V = V_c \cos\left(\frac{2\pi}{T_c}(\alpha + \theta_c)\right) + V_l \cos\left(\frac{2\pi}{T_l}(\alpha + \theta_l)\right) + \text{const.}, \quad (3.4)$$

where $V_{c(l)}$, $T_{c(l)}$ and $\theta_{c(l)}$ denote the amplitude, period and phase shift for circular (linear) polarisation respectively. The values of the period and phase shift extracted from the reference measurement are listed in table 3.3.

Table 3.3 Periodicity and phase shift of circular and linear component of the signal from the optical signal

T_c	θ_c	T_l	θ_l
89.96°	70.24°	2	89.93°
			47.74°

3.5.3 Electrically modulated inverse spin Hall effect

Samples

In order to measure the current induced ISHE, we used a device design where a current is passed through a platinum bar, and voltage can be measured perpendicular to the current direction. Instead of using a simple cross-bar structure, where the voltage signal might be offset due to asymmetry in the device geometry, we have used a Hall bar with six contacts. This allows doing a three-point voltage probe using a potentiometer. The Hall bar was patterned using photolithography on 100 nm YIG films from Matesy. The NM of the first sample we discuss in this work is a 3 nm layer of platinum. There is an additional 2 nm interlayer of rubidium in the second sample to decouple the platinum from YIG. Figure 3.19a shows an optical microscope image of the YIG/Pt Hall bar.

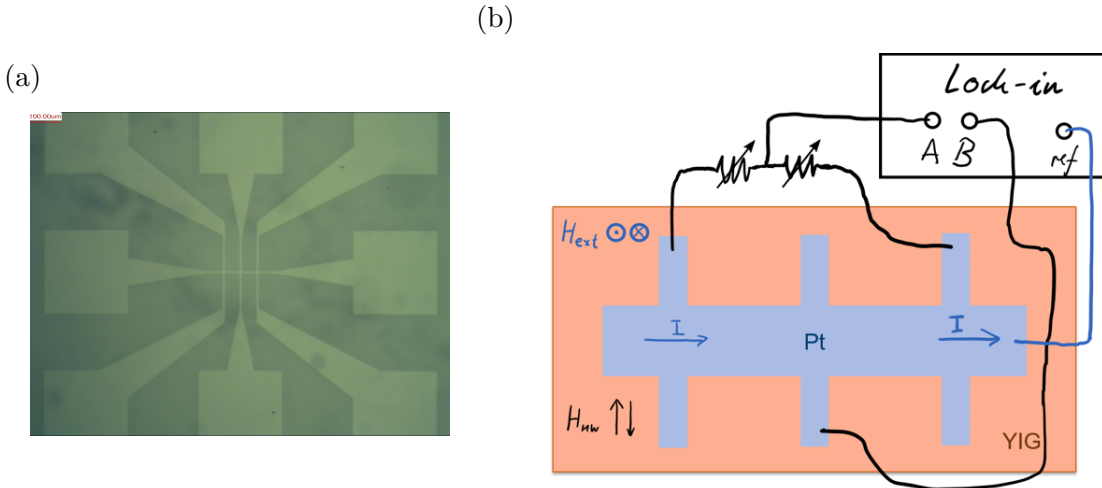


Fig. 3.19 (a) Optical microscope image of the Hall bar device for measuring current induced ISHE. The horizontal bar is $10 \mu\text{m} \times 100 \mu\text{m}$ in size and is contacted by three perpendicular bars, which are parallel and separated by $50 \mu\text{m}$. (b) Schematic of the measurement towards detection of the electrically modulated ISHE including a potentiometer.

Electrically modulated inverse spin Hall effect measurements

The measurements of the electrically modulated ISHE were conducted on the same setup as the spin pumping experiments towards detection of the ISNE with slight alterations of the measurement configuration. The sketch in figure 3.19b shows a schematic of the measurement configuration. An alternating current is passed through the platinum Hall bar, and the voltage perpendicular to the current direction is measured. For this, the voltage between the top two leads and the bottom lead is set manually to zero by using a potentiometer to allow for maximum precision and best possible resolution.

Chapter 4

Quantifying Spin Injection by Measuring Linewidth Broadening

Precise and reproducible measurements of the linewidth of the microwave absorption at FMR are of paramount importance in the linewidth broadening experiments presented in this work. Therefore, before studying spin injection into organic materials, we shall focus on optimisation of the measurement procedure and characterisation of the magnetic permalloy films in this chapter.

4.1 Optimisation of the linewidth broadening measurement

Due to the uniformity of the standing microwave magnetic fields in the ESR cavity and a sensitive lock-in detection method, the microwave absorption measurements using the ESR setup yield very precise and low noise FMR spectra. In order to ensure that the measurements are conducted well outside the power saturation regime, where the lineshape and linewidth might be distorted, the measurement parameters have been chosen carefully. The modulation amplitude of the external magnetic field was set to 0.2 G to allow resolution of changes in linewidth on the same order of magnitude. Furthermore, we used 0.2 mW microwave power to ensure a linear response. In order to optimise the conversion time t_c , the time over which the signal is collected and averaged for one data point, we have conducted reference measurements of the linewidth ΔH of a permalloy film varying t_c . The results are shown in table 4.1. The linewidth is distorted for conversion times shorter than 25 ms. In order to exclude any inaccuracy, we have conducted the LWB measurements with $t_c = 30$ ms.

Table 4.1 Linewidth of permalloy absorption at different conversion times t_c

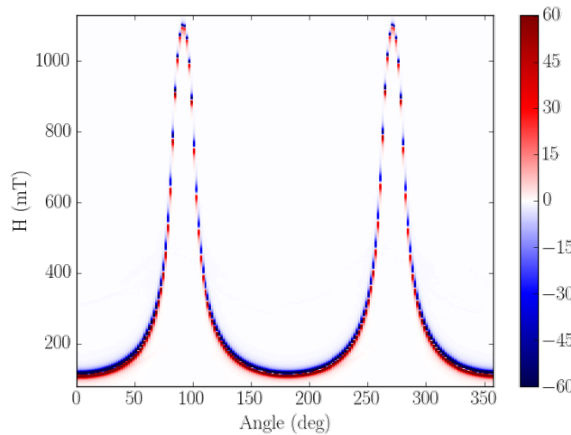
t_c (ms)	10	15	20	25	35	45
ΔH (G)	25.72	25.55	25.45	25.44	25.46	25.44

By repeatedly mounting and measuring the same sample multiple times, the accuracy of the linewidth following the procedure described in section 3.3.2 has been found to be ~ 0.1 G. When studying the change in linewidth due to spin pumping, the precision of the measurements can be further increased by increasing the number of samples studied for each material.

4.2 Characterisation of permalloy

In order to verify the quality of the permalloy film, we have measured the angular dependence of the FMR absorption signal rotating the external field from our standard in-plane configuration to out-of-plane. Figure 4.1a shows the absorption as a function of magnetic field and angle. Here, $\theta_H = 0^\circ$ corresponds to the external magnetic field H in the plane of the permalloy film and $\theta_H = 90^\circ$ denotes the configuration with out-of-plane field. We can observe the typical $\cos(\theta_M)^2$ dependence of the resonance field on the out-of-plane angle θ_H . By fitting the angular dependence of the resonance

(a)



(b)

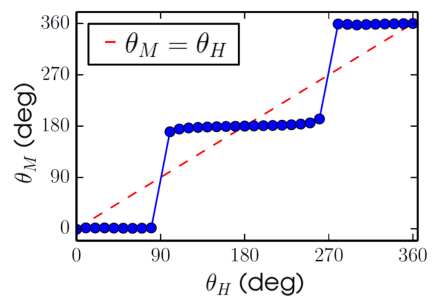


Fig. 4.1 (a) Microwave absorption (a.u.) at FMR of permalloy as a function of external magnetic field H and out-of-plane angle θ_H . (b) Angle of the magnetisation θ_M as a function of out-of-plane angle θ_H of the external magnetic field showing in-plane anisotropy of the thin permalloy film.

field using equation 2.11, we can extract the saturation magnetisation $M_s = 690$ mT and gyromagnetic ratio $\gamma = 29.6$ GHz/T. These values agree well with reports in literature [12] and confirm optimum magnetic properties of the permalloy films.

From the fit, we can also determine the angle of the magnetisation θ_M of permalloy as a function of out-of-plane angle θ_H of the external magnetic field. Figure 4.1b clearly shows the strong in-plane anisotropy of the thin permalloy film, as θ_M follows a nearly step-like switching behaviour when the external magnetic field is rotated out-of-plane.

4.3 Linewidth broadening in Py/Pt

As mentioned section 2.3.2, platinum is known to be a reliable and strong spin sink layer. Spin injection from permalloy into platinum has been quantified previously in several reports in literature, making it a suitable reference system for further LWB experiments.

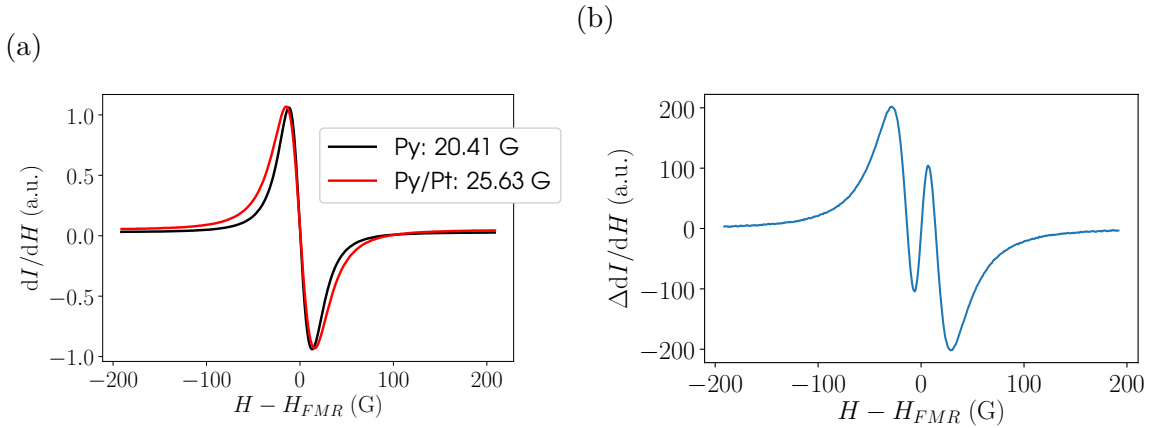


Fig. 4.2 (a) Derivative microwave absorption signal at FMR of a bare permalloy film (black line) and after deposition of 15 nm platinum on the same film (red line). The extracted linewidth of the two curves is listed in the legend. (b) Difference of symmetric components of the two normalised FMR spectra shown in (a) illustrating the increase in linewidth.

The microwave absorption at FMR of four permalloy films has been measured before and after deposition of 15 nm of platinum. Figure 4.2a shows the derivative absorption signal recorded for the bare permalloy film (black line) and after deposition of platinum (red line). We can observe that the peaks of the signal below and above the resonance field H_{FMR} are shifted to the lower and higher magnetic field respectively. Furthermore, the decay of the tails is broader due to the addition of the NM layer. This

is more clearly visualised in figure 4.2b, where the difference between the symmetric components of the normalised FMR spectra of the two curves in figure 4.2a is shown. From fitting the data using equation 3.2, we can extract the linewidth of the bare permalloy film $\Delta H_{Py} = 20.41$ G and with the additional platinum layer $\Delta H_{Py/Pt} = 25.63$ G. Compared to the accuracy of a single linewidth measurement of ± 0.1 G, we can conclude that we can observe a significant increase in linewidth due to spin pumping from permalloy into platinum.

In order to estimate the error in the increase in linewidth due to sample to sample variation, this measurement has been conducted on four different substrates. The normalised average increase in linewidth is given by $\Delta H_{Py/Pt} - \Delta H_{Py} = 5.7 \pm 0.6$ G. The large error might originate in the inhomogeneous deposition of platinum, as the film quality depends strongly on the position of the substrate in the plasma plume in magnetron sputtering.

From the increase in linewidth, we can estimate the spin-mixing conductance to be $g_{eff}^{\uparrow\downarrow} = 3.5 \cdot 10^{19} \text{ m}^{-2}$. This value agrees very well with previous reports of spin injection efficiency across a permalloy/platinum interface in literature [65]. We can, therefore, conclude that the effects on the permalloy films due to exposure to ambient conditions, such as oxidation, do not significantly decrease the spin transparency of the interface. Furthermore, this verifies that LWB is indeed a sensitive method for directly quantifying spin injection into NM layers without relying on additional spin detection mechanisms.

4.4 Effects of solvents on permalloy

A commonly used technique for depositing OSCs is solution-processing. In this method, the OSC is dissolved in a solvent and deposited on the substrate via spin-coating. We noted that some solvent influence the thin layer of permalloy, resulting in an increase of linewidth not due to spin pumping but a change in magnetic properties. Therefore, the solvents had to be tested carefully before employing them for the LWB experiments.

For this, eight different commonly used solvents have been tested by comparing the linewidth before and after spin-coating the permalloy substrates with the respective solvent. The changes in linewidth $\delta\Delta H$ are listed in table 4.2 ordered by the strength of the effect.

There is no significant influence of the solvent on the magnetic properties for THF, ACN and IPA as the change in linewidth is within the accuracy of the LWB measurement. Toluene, Acetone and Hexane show a significant increase by ~ 1 G.

Table 4.2 Change in linewidth due to solvent treatment of thin permalloy films

Solvent	THF	ACN	IPA	Toluene	Acetone	Hexane	Chloroform	DCB
$\delta\Delta H$ (G)	0.1	0.1	0.2	0.9	1.1	1.2	6	9.8

Moreover, an even larger increase by 6 G and nearly 10 G was recorded for the chlorinated solvents Chloroform and DCB.

These findings demonstrate the necessity of being very careful during the processing of the samples in order to minimise and exclude spurious contributions to LWB to allow precise quantification of spin injection properties.

4.5 Conclusions

In summary, we have determined the optimum parameters for reliable and reproducible measurements of microwave absorption in the ESR setup. Furthermore, the quality of the patterned thin permalloy films used throughout the LWB studies presented in this work has been characterised. Spin pumping has been successfully demonstrated in the reference system of permalloy/platinum. Both, the magnetic properties of permalloy as well as the extracted spin-mixing conductance of Py/Pt, agree well with reports in literature. The effects of certain solvents on the magnetic properties have been investigated. Three solvents, THF, ACN and IPA, have been found not to cause a significant increase in linewidth. As a consequence, the use of solvents shall be limited to these for the LWB measurements in this work. We can, therefore, conclude that measuring LWB is indeed a sensitive and suitable technique for quantifying spin injection across an FM/NM interface.

Chapter 5

Spin Injection in Small Molecules

In the preceding chapter, we have shown that linewidth broadening is a sensitive and quantitative measure for spin injection. Due to the simple sample structure and direct determination of the spin injection efficiency, which does not rely on any secondary effect for spin detection, this method paves a novel path to probing spin properties in organic semiconductors. In this chapter, we shall employ this technique to investigate spin injection into small molecules.

5.1 Spin injection into DNTT

The first small molecule system we have investigated spin injection into is DNTT. Figure 5.1a shows the FMR absorption of the bare permalloy substrate (black) and the FMR spectrum after deposition of DNTT. The insets display the shift of the peaks of the signal of the Py/DNTT bilayer to lower (higher) magnetic field below (above) the resonance field (red arrows). This implies an increase in linewidth of the microwave absorption. The difference of the symmetric component of the normalised microwave absorption spectra is shown in figure 5.1 as a function of magnetic field. This signal illustrates the increase in linewidth from the bare permalloy substrate to the DNTT bilayer. The broadening of the absorption in Py/DNTT has been measured for nine samples, and the difference in linewidth is summarised in a histogram in figure 5.1d. In order to simplify direct comparison between different samples, $\delta\Delta H$ has been normalised to a linewidth of 21 G. On average the linewidth increases by $\delta\Delta H = 0.54 \pm 0.05$ G.

In order to exclude distortion of the line shape and linewidth due to interfacial effects, which are not related to spin injection, we have performed this experiment with an additional thin gold layer between the FM and OSC. We verified that the gold

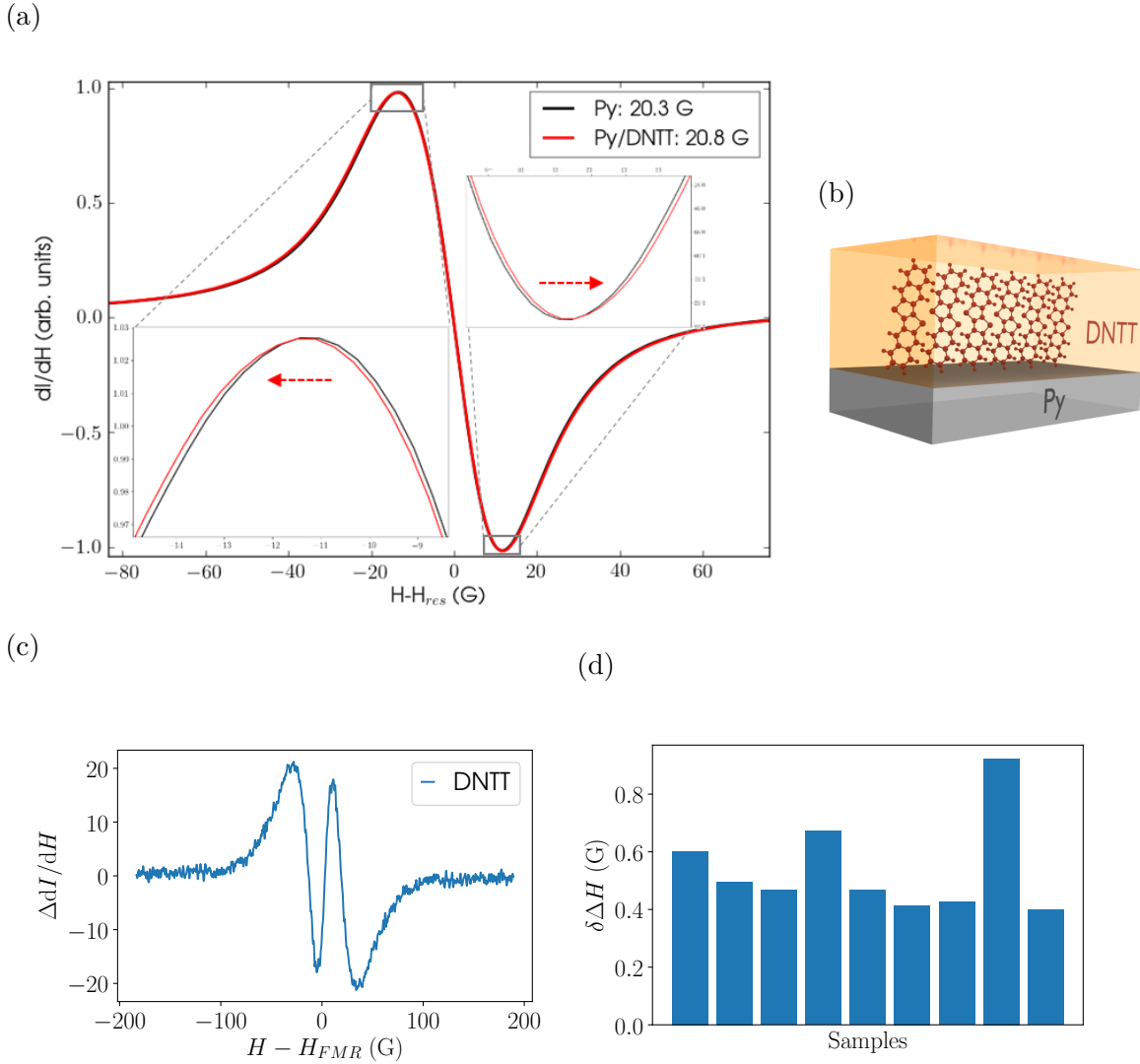


Fig. 5.1 (a) Absorption spectra of the pristine permalloy film (black) and after deposition of DNTT (red). The insets show the magnified region around the peaks clarifying the shift due to the increase in linewidth (red arrows). (b) Schematic of the interface between permalloy and DNTT. (c) Difference between symmetric component of the normalised spectra. (d) Histogram of increase in linewidth for nine different samples.

interlayer does not significantly change the linewidth broadening (more details in the following section 5.2).

Therefore, we can conclude that this significant increase in linewidth is a direct manifestation of spin injection from permalloy into DNTT. We can estimate the spin mixing conductance to be $g^{\uparrow\downarrow} = 3.35 \cdot 10^{18} \text{ m}^{-2}$ for permalloy/DNTT. Compared to platinum, which is known to be an efficient spin sink layer, the spin-mixing conductance

Table 5.1 Change in linewidth, spin-mixing conductance and estimate of spin diffusion length for the three derivatives of DNTT

	DNTT	diPh-DNTT	C ₈ -DNTT
$\delta\Delta H$ (G)	0.54 ± 0.05	0.48 ± 0.09	0.10 ± 0.04
$g^{\uparrow\downarrow}$ (m ⁻²)	$3.35 \cdot 10^{18}$	$2.98 \cdot 10^{18}$	$6.3 \cdot 10^{17}$
λ_{SD} (nm)	40	30	1

extracted for permalloy/platinum with the same interface conditions is one order of magnitude higher (see section 4.3). Given the comparably small charge carrier concentration in DNTT and weak SOC due to the light composition of chemical elements, the spin injection efficiency into the OSC is remarkably high.

5.2 Spin injection into three derivatives of DNTT

Furthermore, we have studied spin injection into all three derivatives of DNTT, which were introduced in section 3.1.2. The interface properties can vary between different batches of permalloy. In order to ensure comparability, we measured linewidth broadening for the three materials on the same batch of magnetic substrates. The changes in linewidth are illustrated in the bar diagram in figure 5.2a for the three derivatives of DNTT at a film thickness of 75 nm. The change in linewidth is comparable for DNTT and diPh-DNTT, where $\delta\Delta H = 0.48 \pm 0.09$ G and considerably suppressed for C₈-DNTT with $\delta\Delta H = 0.10 \pm 0.04$ G. The extracted linewidth broadening and estimate for spin-mixing conductance of the three derivatives of DNTT are summarised in table 5.1.

Moreover, we measured linewidth broadening of the three derivatives of DNTT as a function of thickness ranging from 10 nm to 75 nm. The thickness dependence has been measured on one batch of permalloy for each material and renormalised using the relative results from the comparative experiment mentioned above. The results are shown in figure 5.2b. From the gradual onset of $\delta\Delta H$ for DNTT and diPh-DNTT with film thickness, we can estimate the spin diffusion length to be 40 nm for DNTT and 30 nm for diPh-DNTT from the fit of the data to equation 3.3. The signal for C₈-DNTT is already saturated at 10 nm. Following the same interpretation as for DNTT above, this would imply that the spin diffusion length is considerably shorter. However, interfacial effects such as poor electrical contact between the molecules and the metallic layer might also play a role. This indicates that the backflow due to the

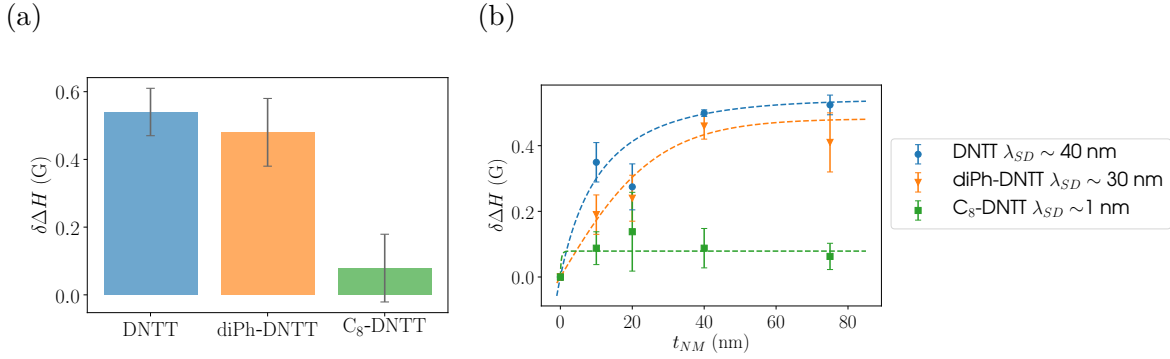


Fig. 5.2 (a) Bar diagram illustrating the change in linewidth for Py/DNTT (blue), Py/diPh-DNTT (orange) and Py/C₈-DNTT (green). (b) Linewidth broadening as a function of the thickness of DNTT (blue circles), diPh-DNTT (orange triangles) and C₈-DNTT (green squares). From the gradual increase in signal with film thickness, the spin diffusion length can be estimated using the fit (dashed lines).

spin accumulation in the material balances injected spin current even in very thin layers.

In order to exclude broadening of the linewidth due to modification of the magnetic properties of permalloy at the interface which are not related to spin injection into the OSC, we have performed the linewidth broadening experiment on samples with an additional gold (Au) interlayer between permalloy and the DNTT derivatives. For this, a 3 nm layer of gold was thermally evaporated subsequent to the evaporation of permalloy without breaking vacuum. The thickness of the Au interlayer is one order of magnitude smaller than the spin diffusion length in Au. Therefore, we would not expect any significant loss of spin angular momentum in the interlayer. The microwave absorption signal was measured for each sample before and after the deposition of the OSC (thickness of 30 nm).

DNTT and diPh-DNTT show significant linewidth broadening of $\delta\Delta H = 0.33 \pm 0.13$ G and $\delta\Delta H = 0.38 \pm 0.16$ G respectively. The increase in linewidth is comparable for the two materials. Comparing the magnitudes of $\delta\Delta H$ with the values for the same thickness of 30 nm for DNTT and diPh-DNTT, which we can extract from the fit to the thickness dependent measurements shown in figure 5.2b, we see that the results agree within the errors.

The third derivative of DNTT we used in this control experiment is C₁₀-DNTT. This is a very similar material system to the previously studied C₈-DNTT in terms of structure and electrical conductivity properties but has slightly longer alkyl side-chains. We cannot observe significant spin injection into C₁₀-DNTT. This confirms the decrease in spin injection efficiency due to alkyl side chains.

Based on the results of this control experiment, we can conclude that the gold interlayer does not affect the change in linewidth significantly. Consequently, we can confirm that the linewidth broadening experiments do indeed probe spin injection across the FM/NM interface.

As the spin-mixing conductance is highly dependent on the interface, we have carefully characterised the structural properties of the molecules grown on permalloy substrates. For this, X-ray reflectivity (XRR) measurements were conducted by JProf K. Broch at the Universität Tübingen in Germany. The obtained XRR data of the three derivatives of DNTT are shown in figure 5.3a-c. The observed Bragg reflection peaks agree well with the crystal structures of the small molecules reported in literature. Hence, we have validated that the thin films of the three DNTT derivatives adopt a 2D herringbone packing in-plane and stack with the long axis of the molecule perpendicular to the substrate as illustrated for DNTT in figure 5.1b. From the fit of the XRR curves at different thickness ranging from 5 nm to 20 nm in steps of 5 nm, the calibration of the thickness of the films has been confirmed within an error of 5%.

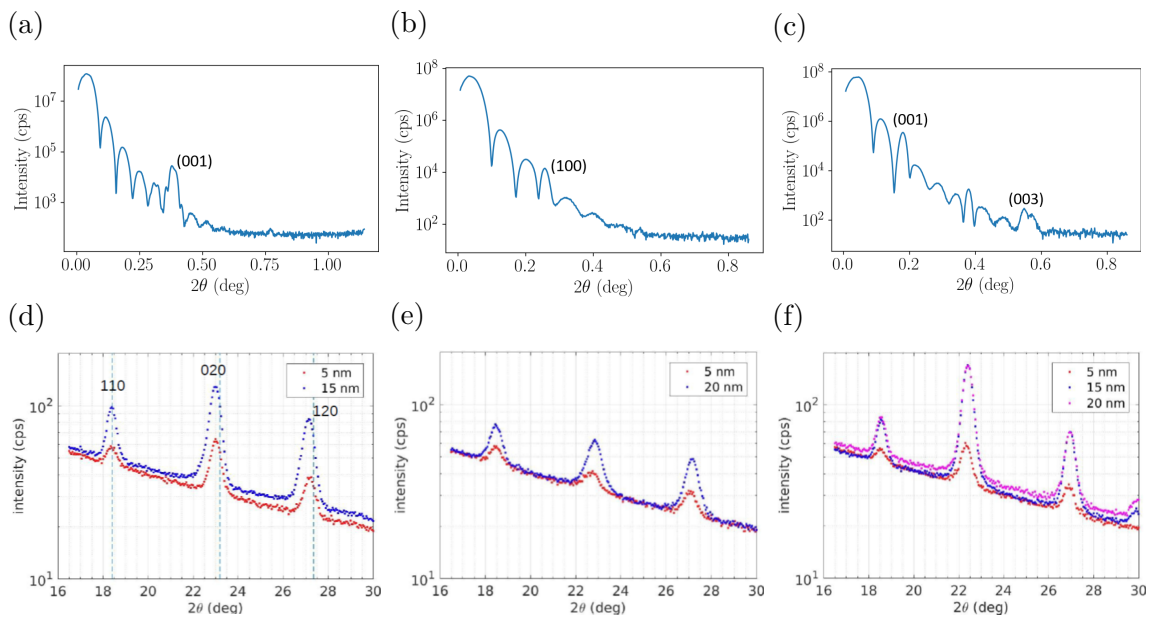


Fig. 5.3 Structural characterisation via XRR measurements of (a) DNTT, (b) diPh-DNTT and (c) C₈-DNTT on a permalloy substrate. The positions of the Bragg peaks agree with the crystal structure reported in literature. Thickness-dependent GIXD measurements are shown for (d) DNTT, (e) diPh-DNTT and (f) C₈-DNTT on a permalloy substrate. There is an indication for a small wetting layer only in DNTT.

Thickness-dependent GIXD measurements on the films of the DNTT derivatives grown on permalloy were conducted by Dr J. Novák at Masaryk University, Czech Republic. The results are shown in figure 5.3d-f. All three molecules grow with the (100) plane of their unit cell parallel to the interface for film thickness ranging from 5 nm to 40 nm. This implies that the long axis of the molecules is approximately perpendicular to the surface of the permalloy film at the interface. Furthermore, the out-of-plane lattice spacing (along (001)) agrees with bulk values reported in literature. The slight shift in peaks in the GIXD spectra for DNTT and diPh-DNTT films indicates an increase and decrease respectively of the in-plane lattice constants as a function of film thickness due to interfacial effects before adopting the bulk crystal structure, while they remain constant for C₈-DNTT. These results validate the assumption that the molecules adopt their preferential orientation with their long axis perpendicular to the substrate at the interface to permalloy.

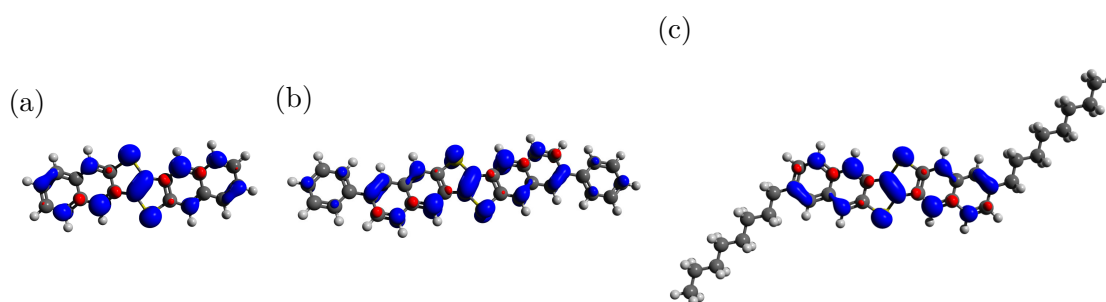


Fig. 5.4 Spin isodensity contour maps of cationic (a) DNTT, (b) diPh-DNTT and (c) C₈-DNTT. Majority and minority spin density are shown in blue and red respectively.

The spin density in the cationic radicals of the three derivatives of DNTT was calculated using DFT by Dr E. McNellis following the same procedure as described in [136]. A visualisation of the distribution of majority (blue) and minority (red) spin on the molecule is shown in figure 5.4 for the three DNTT derivatives. For DNTT, the spin density is distributed over the entire molecule. Similarly, the spin density distributes over the entire molecule in diPh-DNTT and is also delocalised in the phenyl rings. In the case of C₈-DNTT, the spin density shifts only slightly towards the alkyl side chains but remains mostly on the core of the molecule. This implies that the separation of the core of the molecule and thus separation of the regions with high spin density from the interface to the FM due to alkyl side chains decreases the spin injection efficiency significantly.

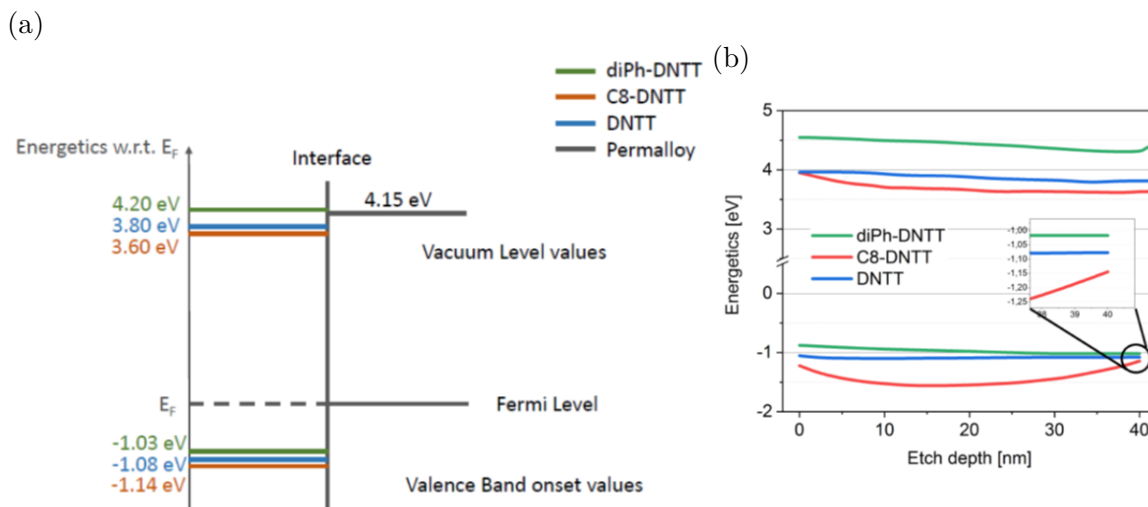


Fig. 5.5 (a) Energy levels of DNTT (blue), diPh-DNTT (green) and C₈-DNTT (red) at the interface to permalloy (grey). (b) Thickness-dependent UPS measurements of the three DNTT derivatives (same colour code as in (a)). The inset shows the hole injection barrier at the Py/OSC interface.

In order to investigate the electronic properties of the three derivatives of DNTT ultraviolet photoelectron spectroscopy (UPS) measurements on thin OSC films on permalloy substrates have been performed by V. Lami in the group of Prof Y. Vaynzof at the Universität Heidelberg in Germany. The diagram of energy levels of the small molecules with respect to the Fermi level of permalloy at the interface is shown in figure 5.5a. From the position of the Fermi level, we can conclude that the three derivatives of DNTT are p-type materials. We presume that the presence of holes in these materials is due to unintentional doping of the films. Figure 5.5b shows the energetics as a function of thickness of the organic film. In this experiment, UPS spectra have been recorded while etching the films down to the interface. The energy levels of the HOMO for DNTT and diPh-DNTT do not show any bending at the interface to permalloy but stay constant from the interface to a film thickness of 40 nm. This implies that the space-charge layer that is induced by permalloy at the interface is negligible confirming that the dependence of the linewidth on the thickness of the organic films is indeed due to spin diffusion.

5.3 Effect of doping on spin injection in DNTT

In order to study the effect of the charge carrier concentration on the spin injection efficiency, LWB experiments have been performed on the three derivatives of DNTT doped with F_4 -TCNQ.

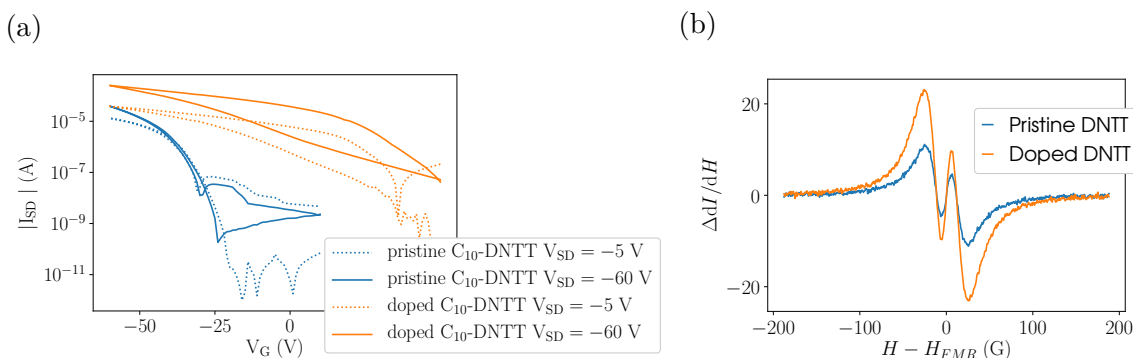


Fig. 5.6 (a) Field-effect transistor characteristics of pristine C_{10} -DNTT and C_{10} -DNTT doped with F_4 -TCNQ (by Dr G. Schweicher) (b) Difference in symmetric part of the microwave absorption signal between bare Py and Py/DNTT (blue) and Py/DNTT doped with F_4 -TCNQ (orange)

The change in charge transport characteristics upon doping with F_4 -TCNQ has previously been studied in C_{10} -DNTT, another derivative of DNTT, which is similar to C_8 -DNTT. Dr G. Schweicher has generously given permission to include his field-effect transistor (FET) measurements in this work. The FET characteristics of pristine (blue) and doped (orange) C_{10} -DNTT thin films in the linear (dotted lines) and saturation (solid line) regime are shown in figure 5.6a. Compared to the pristine C_{10} -DNTT films, the doped film shows an increased hysteresis, a shift in turn-on voltage and higher on- and off-current, which indicates that additional charges have been added in the system. This result implies that the charge carrier concentration in DNTT derivatives can be varied efficiently by doping.

To see the influence of doping on the spin injection efficiency, we have measured the microwave absorption of the same substrates before and after deposition of the OSC and after doping. The increase in linewidth for the pristine DNTT (30 nm thickness) and after doping with DNTT compared to the FMR spectrum of the same bare Py film is illustrated in figure 5.6b. The average change in linewidth for Py/DNTT is $\delta\Delta H = 0.22 \pm 0.01$ G. The increase in linewidth in Py/doped DNTT compared to the bare Py substrate is $\delta\Delta H = 0.50 \pm 0.03$ G. Consequently, the spin injection efficiency increases by more than a factor of two by doping the films. This implies a strong

dependency of spin injection on the number of charge carriers in the OSC.

The change in linewidth upon doping has also been investigated for diPh-DNTT and C₈-DNTT. However, the sample to sample variation was too large to extract a significant influence of doping on linewidth broadening in these materials. This might be due to a change in morphology through solution-doping. During this process, the OSC swells in the solvent to allow for incorporation of the dopants. This can induce critical changes in the structure of the thin films leading to poor charge transport properties. This problem could potentially be alleviated by switching to an alternative doping method in which F₄-TCNQ is evaporated on the OSC film. This technique has been shown to induce efficient doping while retaining the original microstructure [137].

The experimental results suggest that further measurements studying the change in charge transport and structural properties upon doping are necessary to quantify the effect of doping on spin injection.

5.4 Spin injection into derivatives of BTBT

In order to test the generality of the effect of alkyl side chains, another small molecule system similar to DNTT has been investigated. For this, linewidth broadening has been measured for permalloy/ BTBT and C₈-BTBT bilayers. The increase in linewidth with BTBT was determined to be $\delta\Delta H = 0.53 \pm 0.15$ G. This value is comparable to the broadening with DNTT, which can be expected due to the structural and electrical similarities between the two small molecules. The broadening of the linewidth was indeed strongly suppressed for C₈-BTBT with $\delta\Delta H = 0.10 \pm 0.03$ G. This confirms the decrease of spin injection due to addition of alkyl side chains.

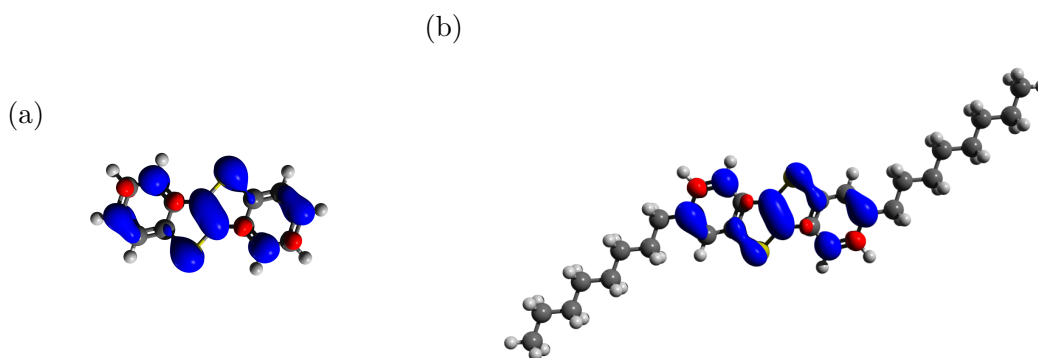


Fig. 5.7 Spin isodensity contour maps of cationic (a) BTBT and (b) C₈-BTBT. Blue and red show the distribution of majority and minority spin density on the molecules respectively.

The theoretically calculated spin density maps of the two derivatives of BTBT are shown in figure 5.7. Similarly to DNTT, the spin density is evenly distributed across the BTBT molecule and does not shift considerably towards the alkyl side chains upon their addition to the core of the molecule.

5.5 Spin injection in small molecules with diradical character

In addition to investigating the influence of the molecular structure on spin injection, we have also explored the possibility of tuning the spin injection efficiency via spin-orbit coupling. For this, several small molecules with theoretically predicted diradical character have been synthesised and the LWB properties tested.

The first diradical molecule we investigated was DFB1. Figure 5.8a shows the difference in the symmetric component of the normalised FMR spectra between a bare permalloy substrate and the same substrate after deposition of DFB1. Due to the normalisation of the spectra before the subtraction, the amplitude of the signal is roughly proportional to the change in linewidth. The average change in linewidth extracted for DFB1 was $\delta\Delta H = 0.14 \pm 0.03$ G. This implies that the spin injection into DFB1 is significantly less efficient compared to the non-alkylated small molecules discussed in the previous section of this chapter.

Structural characterisation has not been conducted on this material yet. However, due to the bulkiness of the molecule, it is expected to adopt large torsion angles in the molecule. As a result, the molecular packing will most likely be mostly amorphous or very unfavourable for charge transport and hence does not allow for delocalisation between molecules.

The initial measurements on indenofluorene were conducted on DX-IDF and DX-IDT. The change in linewidth for the two materials is shown in figure 5.8b and 5.8c respectively. The side peaks for DX-IDT might arise from distortions in the lineshape of this particular sample. However, the magnitude is on the order of the noise level. The average increase in linewidth was extracted to be $\delta\Delta H = 0.6 \pm 0.3$ G for DX-IDF and $\delta\Delta H = 0.23 \pm 0.14$ G for DX-IDT. The larger spin injection efficiency for DX-IDF agrees with the expectation of enhancement of spin injection due to a larger diradical character. However, due to the large sample-to-sample variation, the error for DX-

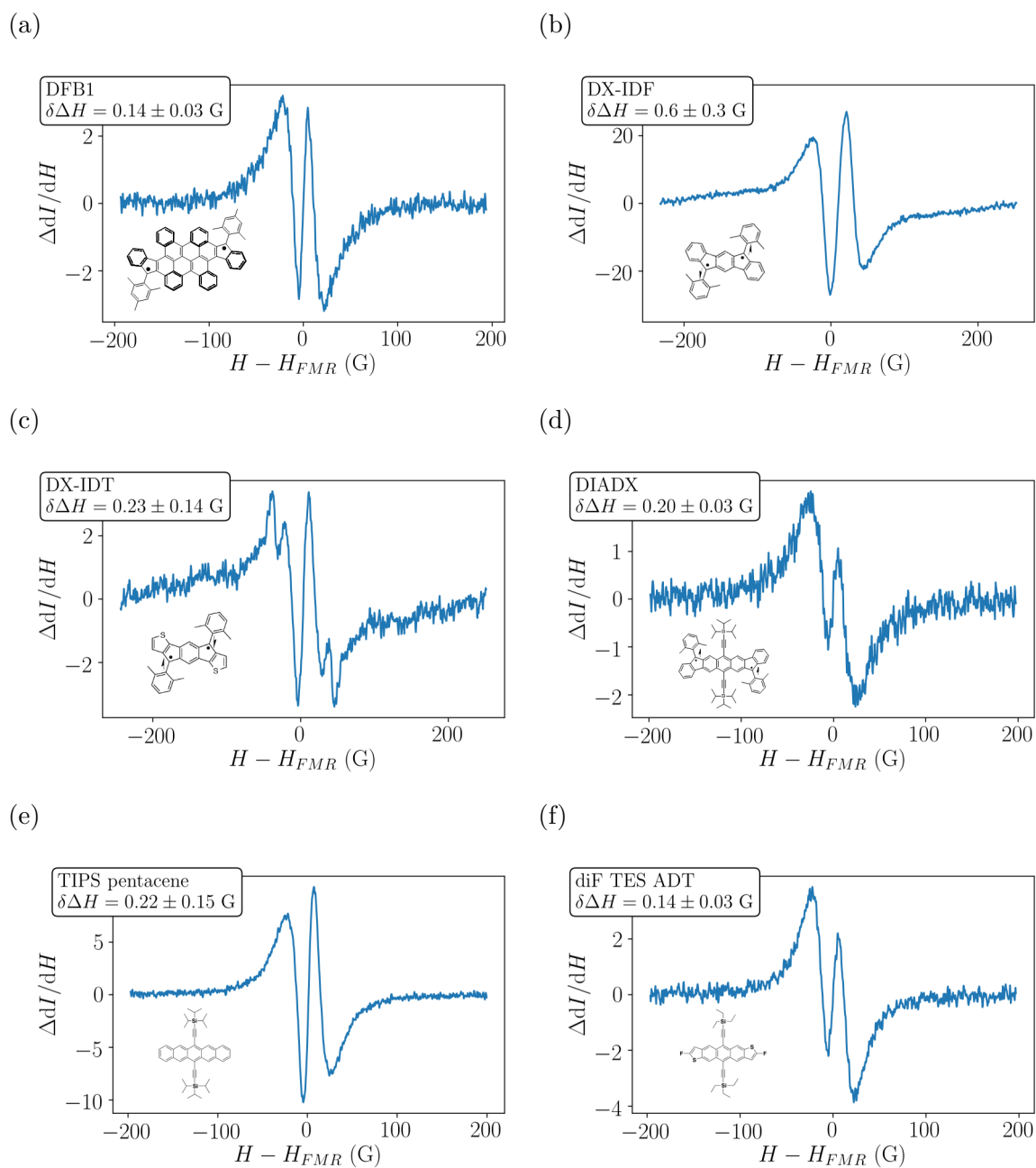


Fig. 5.8 Illustration of the change in linewidth for six small molecules with different diradical character. The difference of symmetric component of the normalised FMR spectra before and after deposition of the NM is shown for (a) DFB1, (b) DX-IDF, (c) DX-IDT, (d) DIADX, (e) TIPS pentacene and (f) diF TES ADT (arbitrary units). Due to the normalisation of the FMR spectra before subtraction, the amplitude of the peaks is proportional to the difference in linewidth.

IDF does not allow us to observe a significant difference between the two materials conclusively.

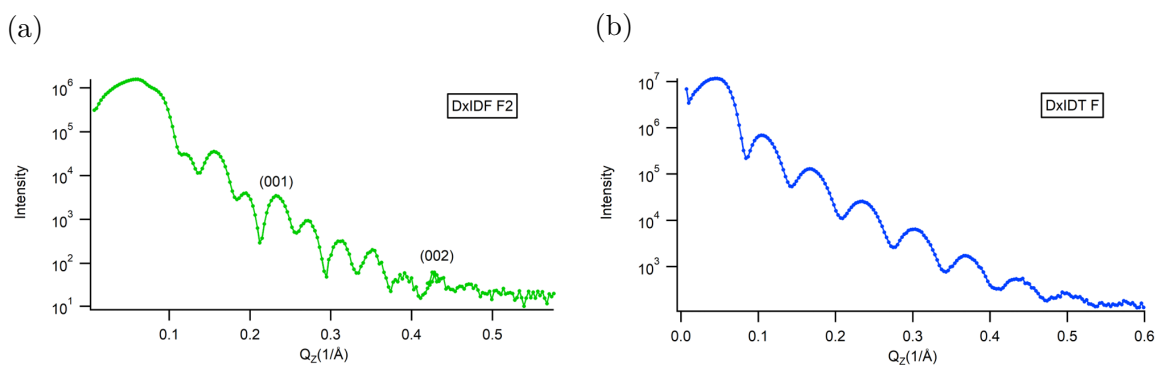


Fig. 5.9 XRR data from Dr K. Broch on the two indenofluorene derivatives on a permalloy substrate. (a) DX-IDF shows two Bragg reflection peaks, while (b) DX-IDT does not show any Bragg peaks.

The structural properties of films of the two small molecules deposited on a permalloy substrate have been investigated by XRR measurements conducted by JProf K. Broch. The obtained curves are shown in figure 5.9. In the case of DX-IDF, two Bragg peaks were observed at $Q_z = 0.21 \text{ \AA}^{-1}$ and $Q_z = 0.42 \text{ \AA}^{-1}$, agreeing with a crystal structure of $a = 1.34 \text{ nm}$, $b = 0.67 \text{ nm}$ and $c = 2.61 \text{ nm}$ reported in literature. No peaks could be observed for DX-IDT, implying that the film grows amorphous. The difference in structural properties makes isolating the contribution due to the increase in diradical character challenging.

The LWB experiments on the halogenated DX-IDF analogues did not result in significant changes in linewidth. This might be due to the fact that the wetting of the solution on the substrates was very poor, resulting in inhomogeneous films with multiple holes and uncovered patches visible under the optical microscope.

Moreover, we have conducted LWB measurements on the Anthracene derivative DIADX, in which a high diradical character had been predicted theoretically. In this experiment, TIPS pentacene and diF TES ADT served as reference materials. The change in linewidth due to spin pumping is illustrated in figure 5.8d-f for the three small molecules. The extracted average increase in linewidth is $\delta\Delta H = 0.20 \pm 0.03 \text{ G}$ for DIADX, $\delta\Delta H = 0.22 \pm 0.15 \text{ G}$ for TIPS pentacene and $\delta\Delta H = 0.14 \pm 0.03 \text{ G}$ for diF TES ADT. Due to the structural similarity, all three materials adopt brick-wall structure.

We can conclude that we do not observe a significant change in spin injection effi-

ciency due to diradical character of the molecule or change in SOC with heavy-atom substitution in this material system.

5.6 Conclusions

In summary, we have successfully demonstrated spin pumping into organic semiconductor small molecules and extracted a sizable spin-mixing conductance of $g^{\uparrow\downarrow} = 3.35 \cdot 10^{18} \text{ m}^{-2}$ for Py/DNTT. This is the first direct observation of spin injection into OSCs as well as measurement of the spin diffusion length, which, unlike previous studies, does not rely on a secondary effect for spin detection.

We have demonstrated strong suppression of spin injection and spin diffusion length due to addition of alkyl side-chains in DNTT and BTBT derivatives. This highlights the importance of the structural properties of the small molecules at the interface to the FM. The vast possibilities of molecular design for organic small molecules combined with the tunability of the spin-mixing conductance bring forth potential for application-specific tailor-made organic materials.

The significant increase in LWB of Py/DNTT with doping implies a sensitive dependence of spin injection on charge carrier concentration in the OSC. This suggests a strong link between spin and charge properties in spin pumping experiments, agreeing with recent findings in spin transport experiments [15]. The observed dependence on spin concentration calls for further investigation and remains an important open question in the field of organic spintronics.

Furthermore, the influence of diradical character on spin injection efficiency has been explored in small molecule OSCs. No significant change in LWB could be observed between open-shell and closed-shell molecule analogues. A large diradical character y requires the overlap of the orbitals of the unpaired electrons to be small, which leads to a large HOMO-LUMO gap. As a consequence, when designing these systems, we have to balance the spin character of the molecule with charge transport and structural properties in order to enhance spin injection efficiency.

Chapter 6

Spin Injection in Polymers

Following on from the work on spin injection into small molecules, we shall expand the exploration to polymers, OSC systems with different transport mechanisms, to get a more general insight into the underlying concepts. The choice of polymers was restricted by the limiting criterion of solubility in THF. Three derivatives of P3HT and IDT-BT have been found to fulfil this requirement and shall be presented in this chapter.

6.1 Structural characterisation

The structural properties have been characterised for P3HT, d-P3HT and IDT-BT on permalloy films deposited on Silicon substrates ($20 \times 20 \text{ mm}^2$). For this, the samples were prepared following the same procedure as for the LWB samples. The Grazing-Incidence Wide-Angle X-ray Scattering (GIWAXS) patterns, shown in figure 6.1, were measured by Dr H. Ahn at Pohang University in South Korea and analysed by Dr B. Kang.

The patterns for P3HT and d-P3HT show dominant peaks along the q_z direction, which are characteristic features of edge-on lamellar stacking. Furthermore, the extracted lamella d -spacing of $\sim 1.8 \text{ nm}$ agrees well with previous reports in literature [3]. The pattern for IDT-BT shows faint signatures of face-on stacking along q_x . However, it is dominated by broad isotropic contributions, indicating an amorphous structure of the film. More details on the crystallographic information can be found in appendix B.

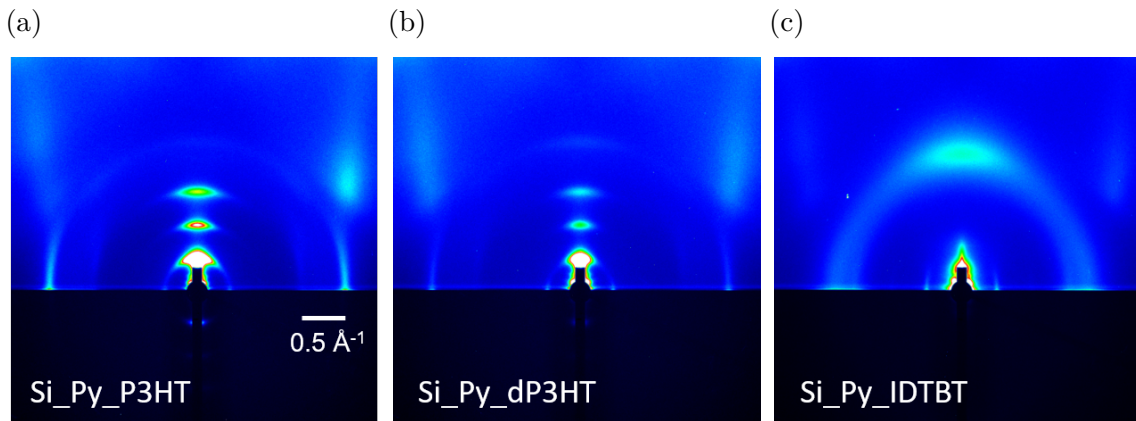


Fig. 6.1 GIWAXS patterns of P3HT, d-P3HT and IDT-BT. P3HT and d-P3HT show the characteristic lamellar stacking, whereas IDT-BT is almost amorphous.

6.2 Linewidth broadening experiments in polymers

We have investigated spin injection from permalloy into four polymers. The samples in this section were all fabricated from polymer solutions in THF at a concentration of 2 mg/ml.

The increase in linewidth for P3HT is illustrated in figure 6.2a, where the difference of the absorption signal of the bare permalloy film and Py/P3HT is shown as a function of magnetic field. The average increase in linewidth was $\delta\Delta H = 1.36 \pm 0.07$ G. This is larger by approximately a factor of three compared to the linewidth broadening for Py/DNTT and of the same order of magnitude as the Py/Pt reference.

In order to exclude contributions to the increase in linewidth arising from impurities, especially metal compounds, which are used during the synthesis of the OSC, the polymer was repurified. No significant change in LWB could be observed, implying that we are indeed probing spin injection into the polymer P3HT and we can exclude significant contribution to the increase in linewidth due to impurities.

As discussed in section 5.2, the spin injection efficiency is very sensitive to interfacial structure and can be significantly suppressed by alkyl side-chains. Given the edge-on alignment of P3HT, the high spin injection efficiency is especially surprising. The ionisation potential (IP) of P3HT lies at -4.8 eV [117], while the IP of DNTT is considerably deeper (< -5 eV). Consequently, *p*-doping by exposure to oxygen in ambient conditions is significantly more efficient in P3HT [118], resulting in a higher charge carrier concentration. The increase in spin injection efficiency with increase in

charge carrier density and spin density agrees well with the findings from the doping experiment on LWB in Py/DNTT in section 5.3.

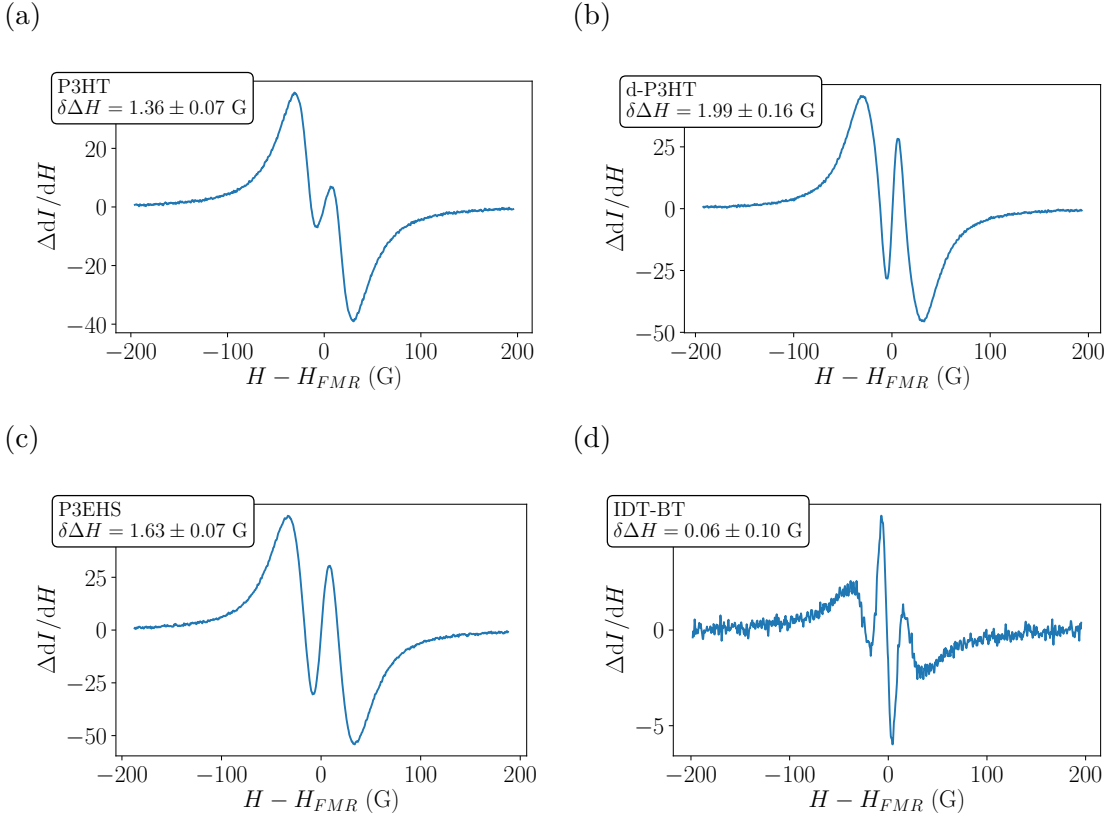


Fig. 6.2 The difference of the symmetric component of the normalised FMR spectra before and after deposition of the NM is shown for (a) P3HT, (b) d-P3HT, (c) P3EHS and (d) IDT-BT.

The linewidth broadening for deuterated P3HT is shown in figure 6.2b. The increase in linewidth was determined to be $\delta\Delta H = 1.99 \pm 0.16$ G. The resulting spin injection efficiency is larger by nearly 50% compared to P3HT.

As discussed in the previous section, the structural properties of the two polymers are very similar. Furthermore, the HOMO and LUMO levels of d-P3HT are close to the energy levels of protonated P3HT [138], implying a comparable level of oxygen doping and thus similar charge carrier concentration. Therefore, the increase in spin injection efficiency cannot be attributed to the difference in morphology or spin density. Due to the edge-on orientation of the polymer, the backbone is separated from the magnetic substrate by the alkyl side-chains. Charge transport mainly occurs along and between the backbones. Analogously to section 5.2, we presume the spin density predominantly to be in the same region as the charge density. Consequently, for spin injection into

the polymer, the spins need to traverse the side-chains efficiently. Deuteration reduces the hyperfine field, leading to less spin relaxation along the side-chains. This could imply more efficient spin injection, which would result in larger linewidth broadening for Py/d-P3HT compared to Py/P3HT.

In order to study the influence of SOC on spin injection efficiency, LWB has been studied in P3EHS. The difference between the bare permalloy and Py/P3EHS absorption spectra is shown in figure 6.2c. The extracted average increase in linewidth was $\delta\Delta H = 1.63 \pm 0.07$ G. In addition to the increase in SOC, there are several other factors, which need to be considered when comparing spin injection from P3HT and P3EHS.

The ionisation potential of P3EHS lies deeper than for P3HT, making oxygen doping less efficient [139]. This results in a smaller charge carrier concentration in the heavy element substituted polymer. Moreover, the branched side-chains introduce more twisting in the molecule along the backbones. As a result, the conjugation length is decreased, leading to worse charge transport properties [140]. These two effects are therefore expected to worsen the spin injection rather than enhancing it. The branched side-chains are expected to allow for more dense packing, which manifests in a smaller lamella d -spacing. However, measurements for characterising the structural properties of P3EHS thin films are necessary. Dr M. Little is currently synthesising the thiophene-based polymer with branched side-chains, P3EHT. Measuring LWB in P3EHT and P3EHS will allow a more direct comparison of the spin injection efficiency with respect to SOC.

In contrast to the aforementioned polymers, we could not measure significant spin injection into IDT-BT. The change in linewidth was on average $\delta\Delta H = 0.06 \pm 0.10$ G. The difference in absorption spectra of the bare permalloy film and Py/IDT-BT are shown in figure 6.2d.

The high mobility and the face-on orientation of the polymer would have been expected to facilitate efficient spin injection and transport. However, the deep ionisation potential of IDT-BT implies inefficient oxygen doping, leading to a low charge carrier concentration and hence a low spin density in the polymer film. This result agrees well with the finding from the doping dependence of LWB in DNTT in section 5.3 and confirms the sensitivity of spin injection on spin concentration.

6.3 Doping of P3HT

In section 5.2, we have seen that the spin injection efficiency depends very sensitively on the number of charge carriers in DNTT. In order to get a more general picture of the influence of the charge carrier and thus spin density on spin injection, we have studied the doping dependence of LWB in P3HT.

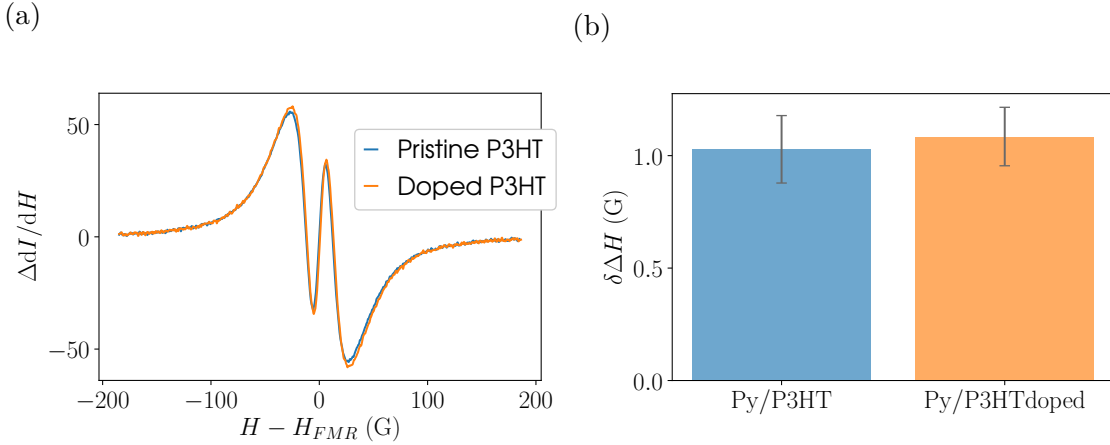


Fig. 6.3 (a) Difference between the FMR spectra of the bare permalloy substrate and Py/P3HT (blue) and after doping with F_4 -TCNQ (orange). (b) Bar diagram of LWB in Py/P3HT and Py/doped P3HT.

The difference between the FMR spectra of bare permalloy and Py/P3HT is shown in blue in figure 6.3a. The orange curve shows the difference between the bare permalloy film and after doping Py/P3HT with F_4 -TCNQ. The amplitude of the orange curve is only slightly larger than the blue, implying a small increase in linewidth. The average increase in linewidth for Py/P3HT and Py/doped P3HT is shown in figure 6.3b. The change in linewidth from $\delta\Delta H = 1.03 \pm 0.15$ G for Py/P3HT to $\delta\Delta H = 1.09 \pm 0.13$ G after doping Py/P3HT with F_4 -TCNQ suggests an increase in LWB upon doping. However, the change lies within the error bars.

As the procedure for solution doping relies on penetration of the dopant through the OSC film, the doping profile, which describes the charge carrier concentration as a function of film thickness, depends critically on the morphology of the film. Therefore, the charge carrier concentration at the interface to permalloy, the region, which the spin injection is most sensitive to, is expected to be smaller than the average in the bulk of the polymer film.

Furthermore, we also have to consider two competing effects when the number of charge carriers is increased in the OSC. So far, in the discussion of doping of DNTT in section 5.2, we have assumed a regime, in which the increase in Gilbert damping is limited by the spin injection rate. This allowed us to relate the increase in linewidth upon doping directly to the increase in spin density. Theoretically, this is described by the direct proportionality $\Delta\alpha \propto \kappa$, relating the increase in damping α to the number of spin scattering channels per interface atom of the ferromagnetic film κ [62].

However, the enhancement of spin injection efficiency by increasing the charge carrier and thus spin concentration in the OSC also results in a higher spin accumulation at the interface when the spin injection rate τ_i^{-1} is higher than the spin-flip relaxation rate τ_{SF}^{-1} . The diffusion of the spin accumulation $\boldsymbol{\mu}_s(x)$ from the FM/NM interface into the NM is given by

$$i\omega\boldsymbol{\mu}_s = D\partial_x^2\boldsymbol{\mu}_s - \tau_{SF}^{-1}\boldsymbol{\mu}_s, \quad (6.1)$$

where D denotes the diffusion coefficient [59]. It follows that a spin accumulation builds up at the interface when the injected spins cannot leave the interface fast enough (limited by D) or relax efficiently (determined by τ_{SF}^{-1}). This spin accumulation drives a backflow of spin current, which reduces the effective increase in Gilbert damping.

These two competing effects of increasing the charge carrier concentration suggest the existence of a critical concentration, above which the enhancement of LWB is compensated and hence saturates. The aforementioned oxygen doping due to exposure of the P3HT films to air leads to an inherently high charge carrier concentration, which might already be approaching the critical spin density. In this case, additional doping with F₄-TCNQ is not expected to modulate the spin injection efficiency significantly.

6.4 Thickness dependence of linewidth broadening

We have investigated the thickness dependence of LWB for three polymers, P3HT, d-P3HT and IDT-BT. The thickness was controlled by varying the concentration of the solution from 0.5 mg/ml to 2 mg/ml. The thickness of the P3HT film spun from a 2 mg/ml solution in THF was determined to be ~ 20 nm via atomic force microscopy measurements. Using the linear relationship between concentration and thickness, we expect the thickness of the films to range from ~ 5 nm to ~ 20 nm.

Figure 6.4 shows the LWB for the three different polymers as a function of solution concentration. Unlike the thickness dependence of the derivatives of DNTT discussed in section 5.2, $\delta\Delta H$ stays constant or even has a slight tendency to decrease with increasing thickness.

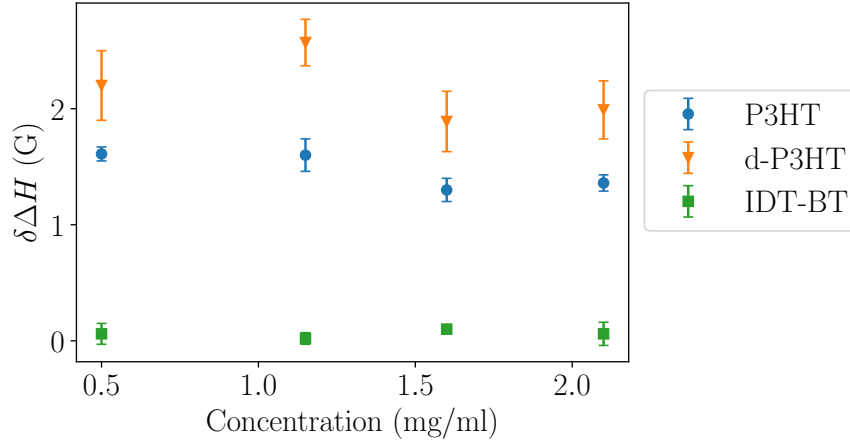


Fig. 6.4 (a) Difference between the FMR spectra of the bare permalloy substrate and Py/P3HT (blue) and after doping with F₄-TCNQ (orange). (b) Bar diagram of LWB in Py/P3HT and Py/doped P3HT.

Using the same model from equation 3.3 as for the thickness analysis for the DNTT derivatives, we can estimate, that the spin diffusion length would have to be on the order of 10 – 100 μm or significantly shorter than 5 nm. However, this does not agree with previous reports in literature, where the spin diffusion length has been determined to be less than 2 μm in thickness dependent spin pumping and inverse spin Hall effect detection experiments [12, 141].

There are several factors, which can contribute to this unexpected thickness dependence. As oxygen doping of the polymer films is more efficient close to the top interface, which is exposed to air, the induced charge carrier concentration at the interface to permalloy might be larger in thinner films. This effect can counterbalance the reduction of spin backflow with increasing film thickness. Moreover, the morphology of the ultra-thin films might change for different film thickness. Therefore, further structural characterisation is necessary in future to get a more conclusive picture of the underlying effects.

6.5 Conclusions

In this chapter, we have explored spin injection into three derivatives of P3HT and IDT-BT. The increase in linewidth in Py/P3HT is $\delta\Delta H = 1.36 \pm 0.07$ G, implying a significantly larger spin injection efficiency compared to Py/DNTT. Both, deuteration and heavy-element substitution in P3HT have resulted in increasing the spin injection efficiency compared to P3HT. However, further material characterisation is necessary to quantify contributions from other coexisting effects. On the other hand, we could

not measure significant spin injection into IDT-BT, which can be linked to the low charge carrier concentration.

The additional charge carriers due to doping P3HT with F₄-TCNQ do not significantly influence the spin injection efficiency. This suggests that the enhancement of LWB with increasing charge carrier density is already saturated due to oxygen doping. Furthermore, LWB has been found to be independent of thickness for thin films ($\lesssim 20$ nm) for P3HT, d-P3HT and IDT-BT. Further structural characterisation is necessary to understand the fundamental mechanism behind this effect.

Chapter 7

Thermal Spin Injection and Detection

The emphasis of the preceding chapters has predominantly been on spin injection into organic semiconductors by spin pumping at FMR. In order to gain a more comprehensive understanding of spin properties in organic semiconductors, this chapter explores thermal effects. The first part focuses on thermal spin injection, the spin Seebeck effect. This is followed by endeavours towards thermal spin detection via the inverse spin Nernst effect.

7.1 Thermal spin injection via spin Seebeck effect

7.1.1 Initial measurements on YIG/Pt

The first thermal spin injection measurements were performed on YIG/Pt bilayer devices using the first version of the SSE setup. Figure 7.1a shows the raw data of a typical SSE voltage curve as a function of magnetic field B at a temperature difference of ~ 1 K. Due to a temperature drift of the average temperature during the magnetic field sweep and a contribution from the conventional Seebeck effect in platinum, there is a small linear drift and off-set in the raw data. The pure SSE voltage can be obtained by subtracting these contributions and is shown in figure 7.1b (this procedure is carried out with all measurement data unless stated otherwise). The voltage follows the magnetisation of YIG. It shows a sharp switching between the saturation fields between ± 5 mT and nearly no hysteresis. The SSE voltage signal at 1 K can be clearly observed and is approximately $4 \mu\text{V}$ in magnitude with a very low noise level of approximately ± 20 nV.

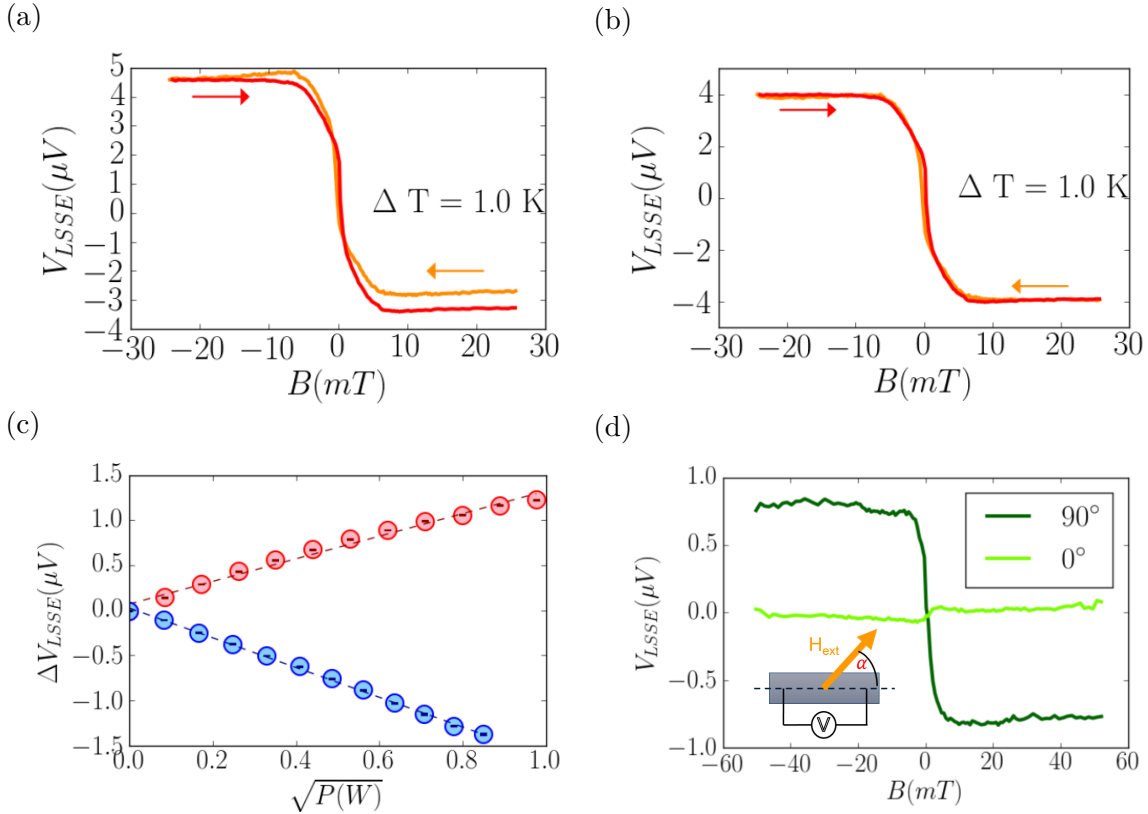


Fig. 7.1 SSE measurements on YIG/Pt using the first version of the setup (a) Raw data of the SSE voltage as a function of magnetic field B at a temperature difference of ~ 1 K. The arrows indicate the direction of the magnetic field sweep. (b) SSE voltage which has been corrected for a linear drift and offset. (c) SSE voltage signal as a function of the square root of the applied cooling (blue) and heating (red) power P of the Peltier element respectively. The dashed lines are linear fits through the data points. (d) Angular dependence of the SSE voltage. The dark (light) green line shows the voltage measured perpendicular (parallel) to the external magnetic field.

It is rather difficult to compare the magnitude of the SSE voltage to experimental results from different setups. This is due to the fact that the signal depends on many different parameters, such as film thickness of the samples and distance between the voltage probes, as the SSE voltage scales linearly with length [142]. Additionally, a critical factor is the determination of the temperature difference across the sample. Even changing to the modified sample holder, the signal, normalised by the temperature difference, decreased by more than a factor of five. This implies that absolute quantitative comparisons to previous findings are problematic. Nevertheless, comparison between different samples measured in the same setup and also between measurements on devices on different setups with respect to a YIG/Pt reference is possible.

After having successfully measured a signal, its symmetry had to be investigated in order to confirm that it is indeed due to the SSE. First, the dependence of the voltage signal on temperature difference has been studied. For this, the cooling and heating power respectively of the Peltier element has been varied. The temperature of a Peltier element depends linearly on the applied voltage or current, thus is proportional to the square root of the power.

In the first version of the probe head, the temperature measurements were somewhat unreliable. Furthermore, for small temperature differences, it can be assumed that the temperature difference across the sample depends linearly on the temperature of the Peltier element. For these reasons, the dependence of the voltage signal on the temperature difference is shown as a function of the square root of the power of the Peltier element in figure 7.1c. The data points marked in red show the voltage signal while the Peltier element was used to heat the sample and the points marked in blue show the signal for cooling. The dashed lines are a linear fit through the data points and show that the dependence of the voltage signal on the square root of the Peltier power is linear. Moreover, the sign of the voltage switches when the temperature gradient is applied in the opposite direction. However, the magnitude of the voltage is not precisely symmetric for cooling and heating. This might come from the fact, that generally cooling is more efficient in Peltier elements.

In order to check the symmetry of the ISHE in the platinum layer, measurements at two different angles have been performed at a temperature difference of ~ 0.2 K. Here 90° (dark green line) correspond to the usual configuration where the voltage is measured perpendicular to the external magnetic field, and 0° (light green) corresponds to measuring the voltage parallel to the magnetic field. The measured voltage as a function of magnetic field is shown in figure 7.1d.

For 90° the voltage signal is $\sim 0.8 \mu\text{V}$. One can observe a very small switching of the voltage signal of $\sim 0.05 \mu\text{V}$ around zero magnetic field, which presumably comes from a slight angular displacement. Hence, the measurements agree with the expectation that the voltage is a sinusoidal function of the angle.

Contributions from other effects such as the anomalous Nernst effect or the proximity Nernst effect have previously been shown to be negligible by making use of the different symmetry of the effects and the behaviour in strong magnetic field [143, 144, 76].

These preliminary experiments on YIG/Pt devices agree very well with the theory and previous findings. Therefore, we can conclude, that our SSE experimental setup is working well and we could successfully measure the SSE in these bilayer devices.

7.1.2 Inorganic bilayer devices

In order to compare the signal strength of different metals, YIG/metal devices with three different materials have been investigated. For this, the modified setup was used to achieve higher temperature gradients across the samples. Apart from the standard YIG/Pt, YIG/Cr and YIG/Pd were thought to be promising candidates. The SSE voltage normalised by the temperature difference is shown in figure 7.2.

Even though the spin Hall angle of chromium is claimed to be around half of the spin Hall angle of platinum [125], a higher resistivity leads to a comparable SSE voltage signal, as shown in figure 7.2b. K. Uchida *et al.* [145] on the contrary reported that the normalised voltage is more than five times smaller in YIG/Cr compared to YIG/Pt. As expected, the sign of the signal of YIG/Cr is opposite to YIG/Pt. This is due to the fact the spin Hall angle is of opposite sign for these two materials. However, it has to be noted that the noise level of the signal is approximately four times higher in YIG/Cr compared to YIG/Pt.

The spin Hall angle of palladium is reported to be around a factor of five times smaller compared to platinum as well [146, 147]. However, the low resistivity leads to a normalised SSE voltage signal for YIG/Pd, which is approximately ten times smaller than for YIG/Pt (see figure 7.2c).

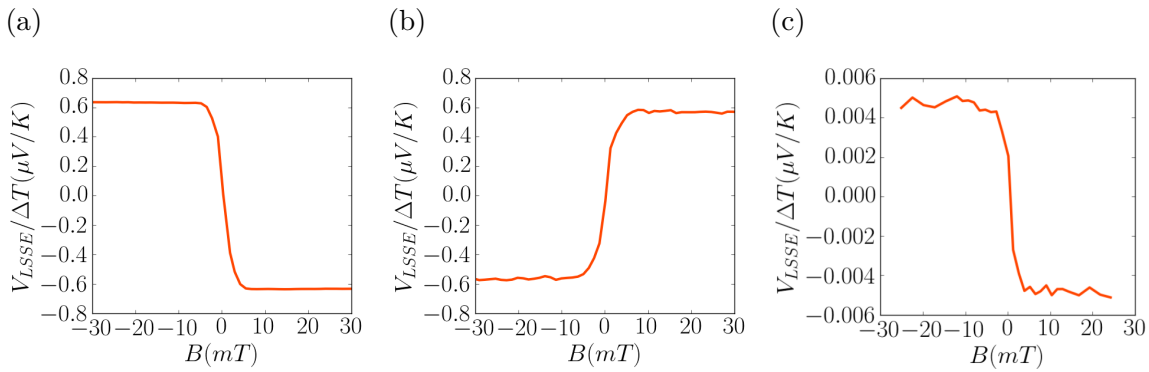


Fig. 7.2 SSE voltage normalised by the temperature difference as a function of magnetic field for three different YIG/ metal devices with (a) platinum (b) chromium and (c) palladium.

From these measurements, we can conclude that chromium along with platinum is a good candidate for trilayer devices. The advantage of chromium over platinum is that it can be easily thermally evaporated. In this process the individual chromium atoms have much lower energy when reaching the surface of the substrate, which might improve the interface. However, the increase in noise and oxidation of Chromium might

be detrimental in trilayer measurements. Furthermore, chromium is known to form anti-ferromagnetic and ferromagnetic half-metallic oxides under certain circumstances [148]. Given that it is not a noble metal and its oxidation is not well-controlled in our experiments, chromium might not be an ideal candidate for reliable spin measurements.

7.1.3 Organic devices

Trilayer devices

For the first try, organic trilayer devices with YIG/OSC/Pt or Cr, where PBTTT and P3HT have been chosen as the OSC layer, have been fabricated as described in section 3.4.1. Typical voltage measurements as a function of magnetic field are shown in figure 7.3 for five field sweeps with YIG/P3HT/Pt. First, it is noted that the noise level in these trilayer devices is more than twice as high compared to YIG/Pt. This could be due to shot noise which comes from a formation of a Schottky barrier at the organic-metal interface [149, 150]. Furthermore, this figure shows that the variation between different sweeps is considerable, which makes observing an SSE voltage behaviour impossible for the obtained data with the current noise level.

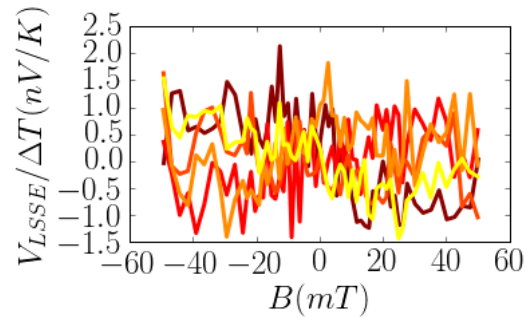


Fig. 7.3 Normalised voltage as a function of magnetic field of YIG/P3HT/Pt. Here, five different measurements are shown. Each measurement is marked in a different colour from dark red to yellow.

Unfortunately, all organic trilayer devices showed similar behaviour, so that no clear SSE voltage signal could be observed.

Delaminated films

Usually, the electrostatic force causes the delaminated films to adhere to the substrates it is transferred onto. In the case of platinum, this layer is too conductive for an electrostatic force to build up.

Transferring PBTTT and P3HT films was successful. The data from three different field sweeps for YIG/ delaminated (P3HT/Pt) is shown in figure 7.4 marked by dots. The solid blue line shows the average of the three measurements. The trend of the normalised voltage follows the SSE signal. However, the noise level is much higher

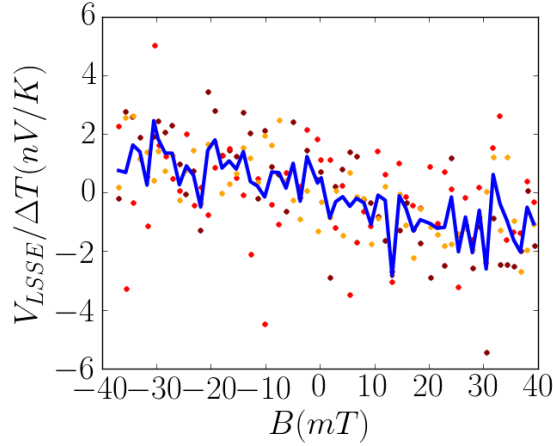


Fig. 7.4 Normalised SSE voltage as a function of magnetic field of YIG/ delaminated (P3HT/Pt). The points show three different measurements (each colour corresponding to one sweep) and the solid line represents the average of all data points.

than the possible SSE signal. Therefore, it cannot be concluded, that this indeed is an SSE signal. The data for PBTTT shows a slightly smaller noise level but is similarly inconclusive.

7.1.4 Conclusions

It has been shown that the SSE setup works very well and can achieve a temperature difference of more than 30 K across the samples. Using this setup, the SSE has been successfully observed in YIG/Pt. At a temperature difference of 34 K, an SSE signal of $21.5 \mu\text{V}$ was measured. The symmetry of the voltage signal has been studied and shows complete agreement with the theoretical predictions and previous findings. It has been found that YIG/Cr yields an SSE signal which is similar in magnitude as for YIG/Pt, whereas it had been found to be more than a factor of four times smaller [145]. However, the SSE has not yet been observed in devices with an organic interlayer. There is an indication that platinum penetrates significantly into the OSC film during sputtering. This implies that the interface between the organic material and platinum is heavily damaged which might be a reason for not being able to measure an SSE signal.

The experimental results suggest that the key to observing thermal spin injection into OSCs lies in finding a suitable material, which can be deposited on an organic film in a non-destructive way while retaining high spin-to-charge conversion efficiency.

One possible route might be high-pressure sputtering of platinum with an additional thermally evaporated interlayer of aluminium, which acts as a buffer layer, which has been developed recently by Dr R. Di Pietro. Using this method of deposition, spin transmission through an OSC and detection via the electrically modulated ISHE in platinum on top has been successfully measured (personal correspondence, unpublished work).

7.2 Thermal spin detection via inverse spin Nernst effect

Conventionally, spin-to-charge conversion in heavy metal layers via the spin Hall effect or electrical spin detection has been used to measure spin currents in OSCs. A significant drawback of these indirect methods is that we have to introduce an additional interface between the OSC and the detection layer, at which spin information can be lost due to additional scattering at the interface. Additionally, electrical measurements can introduce considerable noise due to the conductivity mismatch of the two different materials. Recently, direct spin Hall measurements in organic materials have been successfully conducted by M. Qaid and O. Zadvorna in the groups of Prof G. Schmidt and Prof H. Siringhaus (personal communication, unpublished work). However, due to the small spin Hall angle, which can be attributed to the light composition of OSC, and hence small spin-orbit coupling, it is challenging to measure an accurate signal.

As an alternative, we propose here the idea of detecting spin thermally. Two ways of injecting a spin accumulation into an NM, spin pumping from an insulating FM at FMR and optical spin injection from GaAs, are discussed in the following two subsections. For the initial measurements, we chose to investigate this effect in platinum, as it has served as a reliable spin and charge inter-conversion material. Furthermore, the inverse effect, where a spin accumulation is created with a charge current and a perpendicular temperature gradient, the direct spin Nernst effect, has been reported in Pt recently [19], making it a promising candidate for observing the ISNE.

7.2.1 Towards inverse spin Nernst effect in YIG/Pt

YIG has been shown to have a strong in-plane magnetic anisotropy. In order to determine the magnetic field at which the magnetisation is pointing parallel to the out-of-plane magnetic field, we have measured the voltage across platinum with respect

to the modulation of the out-of-plane temperature gradient as a function of out-of-plane magnetic field. In this measurement, the current through the heaters has been modulated at 57 Hz, and no microwave power has been applied. The second harmonic voltage signal is shown in figure 7.5.

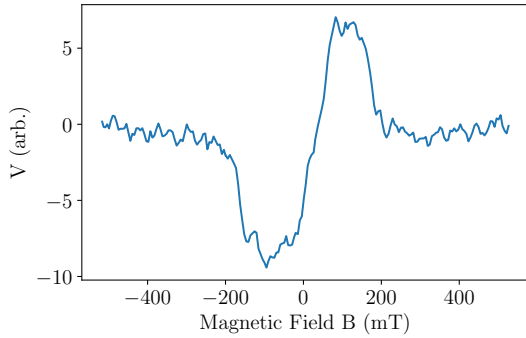


Fig. 7.5 Lock-in second harmonic voltage signal across the platinum bar with respect to modulation of heater power as a function of out-of-plane magnetic field. The magnetisation tilts in plane between -200 mT and +200 mT due to strong in-plane anisotropy of YIG, giving rise to a conventional SSE signal.

From this, we can conclude that this interface allows spin pumping from YIG and platinum indeed serves as an efficient spin to charge conversion layer. In the following ISNE experiment, the microwave frequency has been chosen such that the resonance field H_{FMR} is well above 200 mT to ensure pure out-of-plane spin polarisation.

In order to create an out-of-plane spin polarisation in platinum, YIG was excited with a microwave magnetic field at 3 GHz perpendicular to the external magnetic field, which is normal to the sample plane. The third panel in figure 7.6a shows the microwave transmission of the stripline in the coplanar waveguide as a function of magnetic field. The voltage was recorded as a first harmonic signal with respect to chopping the microwave field at a frequency of 12.345 kHz at a microwave power of 500 mW. It can be expected that at such high microwave power, some of the spin might also be injected thermally as YIG heats up at FMR. This is beneficial for increasing the total spin accumulation in the detector and should lead to a larger ISNE signal. The heating due to the microwaves should not influence the thermal detection of the spin accumulation as the modulation is at the frequency of the spin injection and not

As expected, we cannot observe a voltage signal at magnetic fields below -200 mT and above 200 mT as the temperature gradient and magnetisation, hence also spin polarisation, are colinear. Hence, there is no driving force for spin-dependent scattering which could induce an electromotive force along the voltage probes. However, in the region around zero magnetic field, the magnetisation tilts in-plane resulting in a conventional SSE voltage signal, which follows the magnetisation reversal.

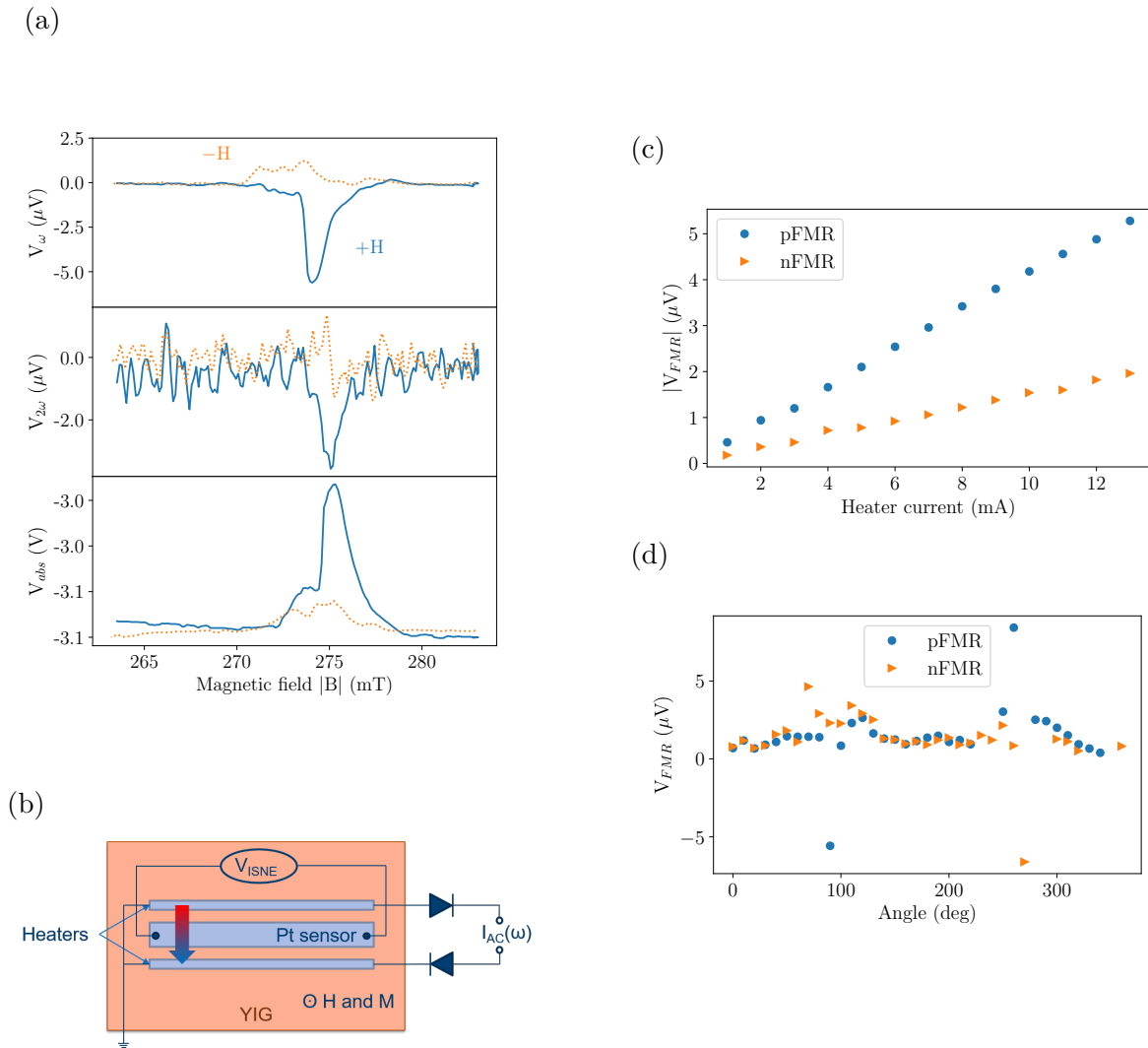


Fig. 7.6 (a) The topmost two panels show the first and second harmonic voltage signal with respect to modulation of the heater current and additional modulation of the microwave field as a function of positive (solid blue line) and negative (dotted orange line) out-of-plane magnetic field. The diode voltage measuring the microwave transmission as a function of magnetic field is shown in the third panel, indicating that the resonance field is at 275 mT. At FMR the peaks in the first and second harmonic voltage signal are of opposite sign for positive and negative magnetic field. (b) Schematic of measurement configuration. (c) Magnitude of voltage signal at FMR at positive (blue dots) and negative (orange triangles) out-of-plane magnetic field as a function of applied heater current. (d) Angular dependence of voltage signal at FMR at positive (blue dots) and negative (orange triangles) magnetic field. At zero angle the magnetic field lies in the plane of the sample and is perpendicular to the platinum sensor. At 90° the magnetic field is normal to the sample.

the heaters. The peak in diode voltage indicates that the resonance field for FMR in out-of-plane magnetic field lies at 275 mT. It is notable that the microwave absorption is not symmetric for positive and negative magnetic field but is highly suppressed in the latter. This has previously been observed in different samples on this setup and might be due to inhomogeneities in magnetic field.

The voltage across the platinum sensor was measured as a function of the modulation of the heater current in addition to the chopping of the microwave field. In this measurement, a heater current of 13 mA was applied. The first and second harmonic response are shown in the two topmost panels of figure 7.6a.

For the first harmonic signal, the peak in voltage at FMR is $-5.5 \mu\text{V}$ at positive magnetic field (solid blue line). At negative field (dotted orange line) the peak is reduced to $1 \mu\text{V}$ and of opposite sign. The smaller magnitude of the voltage signal can be ascribed to the smaller absorption signal at negative magnetic field, which is resulting in less efficient spin pumping possibly due to slight misalignment of the sample. The dependence of the sign of the signal on the direction of magnetic field indicates this effect is indeed spin-dependent.

The second harmonic voltage signal shows a small peak of $-2.8 \mu\text{V}$ at FMR at positive field. However, the signal at negative field is concealed in the high noise level of approximately $0.5 \mu\text{V}$. The origin of the second harmonic signal is independent of which heater the current passes through. This suggests that the signal arises from the change in the out-of-plane temperature gradient between the YIG substrate and the platinum sensor as YIG heats up considerably during FMR [151].

Figure 7.6c shows the magnitude of the voltage signal at FMR as a function of applied heater current varying from 1 mA to 13 mA. The data points at positive and negative field are denoted with blue circles (pFMR) and orange triangles (nFMR) respectively. Surprisingly, the signal for both polarities of magnetic field seems to depend linearly on heater current. As mentioned in section 2.5.3, the ISNE predicts a linear dependency of the signal on heater power $P = RI^2$, where $R = 1.2 \text{ k}\Omega$ denotes the resistance of the heater. Hence, we would expect a quadratic dependence on heater current I .

As the applied heater current results in a comparably high heater power ranging from 1 mW to 0.2 W, nonlinearities in the distribution of temperature in YIG can arise, and the magnetic properties might be distorted at such high temperatures. Additionally, there have been recent reports of injection of magnons from platinum into YIG by applying a current and magnon transport over several micrometres in YIG [152, 153], which could influence spin pumping.

The voltage signal at positive and negative FMR are shown in figure 7.6d as a function of angle. Here, zero degree corresponds to the external magnetic field pointing in the sample plane, and 90° denotes out-of-plane field. There is a positive offset of approximately $0.5 \mu\text{V}$ at in-plane magnetic fields. The voltage signal only arises at precisely out-of-plane magnetic field. This unexpected high sensitivity to the angle might be due to the strong in-plane anisotropy of YIG. Furthermore, the anisotropy might also manifest itself in spin orientation selectivity at the interface of YIG and platinum, favouring in-plane spin polarisation.

In summary, we observe a spin-dependent signal at FMR, which shows the correct symmetry upon inversion of the magnetic field. The heater current, as well as the angular dependence measurements, suggest that there might be competing effects coming into play. As a result, the contribution due to the inverse spin Nernst effect could not be extracted in this measurement.

7.2.2 Towards inverse spin Nernst effect in GaAs/Pt

Photodiode characteristics

At first, the optical properties of the GaAs sample have been verified by measuring I-V characteristics between the back contact and the platinum sensor. As shown in figure 7.7, the sample exhibits typical characteristics of a photodiode. The dark current (dashed blue line) shows a rectifying behaviour and the reverse current increases when the sample is illuminated with laser light at $640 \mu\text{W}$ power.

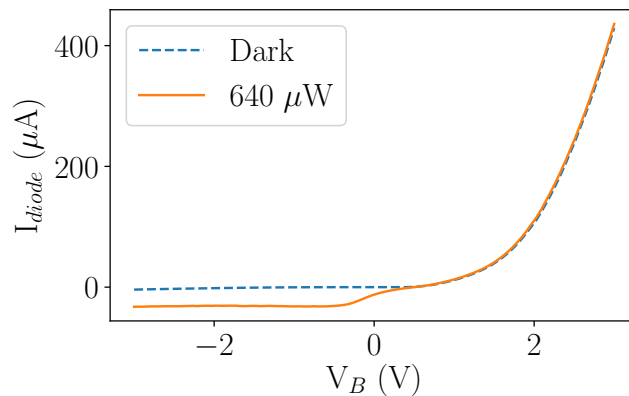


Fig. 7.7 I-V characteristics of the GaAs photodiode under laser illumination (orange line) and in the dark (dashed blue line).

Towards detection of inverse spin Nernst effect in GaAs/Pt

After confirming that photoexcitation of charge carriers works well in our sample, the ISNE measurements were conducted. For this, the reverse bias was set to -2 V on the back contact. In the first attempt, the configuration with two heaters connected via diodes as in the preceding spin pumping ISNE was adopted. The obtained data is shown in figure 7.8a. In this measurement, the amplitude of the AC voltage across the heaters was set to 2.8 V and the power of the incident laser beam on the sample measured to be $640 \mu\text{W}$.

The signal did not show any significant dependence on the polarisation of the light. The noise level of the measurement was $\sim \pm 20 \mu\text{V}$ and increased further with increasing larger heater power. It was noted that the resistance between the two heaters was in the Megaohm range. This indicates that the insulation of the aluminium oxide layer was insufficient for electrically decoupling the conductive GaAs substrate from the heaters. Therefore, when a voltage is applied to one end of one heater, the current flow is ill-defined as it can spread to the other heater as well. The noise introduced by the leakage made a sensitive detection of the thermal spin detection impossible.

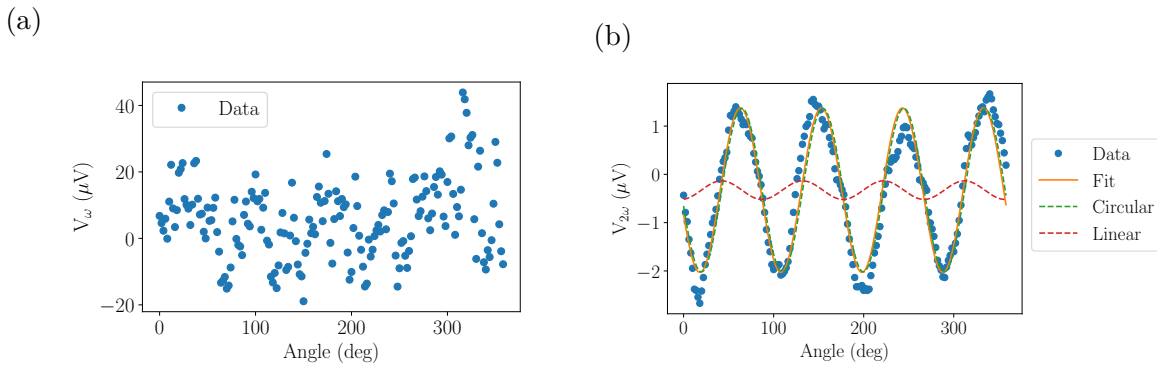


Fig. 7.8 (a) Data obtained in the ISNE measurements with two heaters in the diode configuration. The noise level of $\sim \pm 20 \mu\text{V}$ was too large to detect the thermal signal. (b) Second harmonic signal (blue dots) in the configuration using only one heater. From the fit (solid orange line) the component due to circular polarisation (dashed green line) was determined to be dominant over the linear polarisation (dashed red line).

In order to circumvent the problem with the electrical contact between the heaters, measurements with only one heater have been investigated. The data (blue dots) shown in figure 7.8b was taken at a laser power of $320 \mu\text{W}$ applying an AC voltage with amplitude of 10 V across the heater. The other heater was left floating to minimise

cross-talk between the two heaters. The recorded signal shows a clear dependence on the angle of the half-wave plate. From the decomposition with the fit to equation 3.4 (solid orange line) to the data the amplitude of the component due to the circularly polarised light (dashed green line) was determined to be $V_c = 1.7 \mu\text{V}$. This is significantly larger than $V_l = 0.2 \mu\text{V}$. Therefore, we can conclude there is a significant signal arising from circularly polarised light, which depends on the helicity of the polarisation. In addition to this, the signal is also dependent on the second harmonic of the heater current. It is therefore independent of the direction of the current and the Oersted field. Hence, we can presume that the origin of the effect causing the signal indeed lies in heating.

The analogous measurement was repeated using the other heater. Again, a clear angular dependence could be observed. However, the sign of the signal was the same for both heaters even though the direction of the temperature gradient was inverted. As a result, this effect in GaAs, which depends on the helicity of circularly polarised light as well as temperature, dominates over any potential contribution to the signal from the ISNE.

Consequently, the ISNE could not be detected in this architecture due to temperature and polarisation dependent effects in GaAs, which are modulated by the large leakage current from the heater.

7.2.3 Spin detection via electrically modulated inverse spin Hall effect

As the observation of the ISNE proved to be more difficult than expected, we wanted to take a step back and perform a similar but more straightforward experiment in order to identify a promising material system for further investigating thermal detection more successfully. For this, we followed previous work in literature and did AHE-like measurements, where the spins are not driven by a temperature gradient but electrically modulated [105, 104].

At first, ISHE at FMR has been measured in a YIG/Pt sample patterned into a Hall bar structure. For this measurement, a microwave frequency of 5 GHz and power of 1 W was applied. The result is shown in figure 7.9a. The dotted orange line corresponds to the diode voltage measuring the microwave transmission. The peak at 110.8 mT indicates the location of FMR. The solid blue line shows an ISHE voltage signal of $175 \mu\text{V}$ at FMR, which agrees well with previous measurements and reports

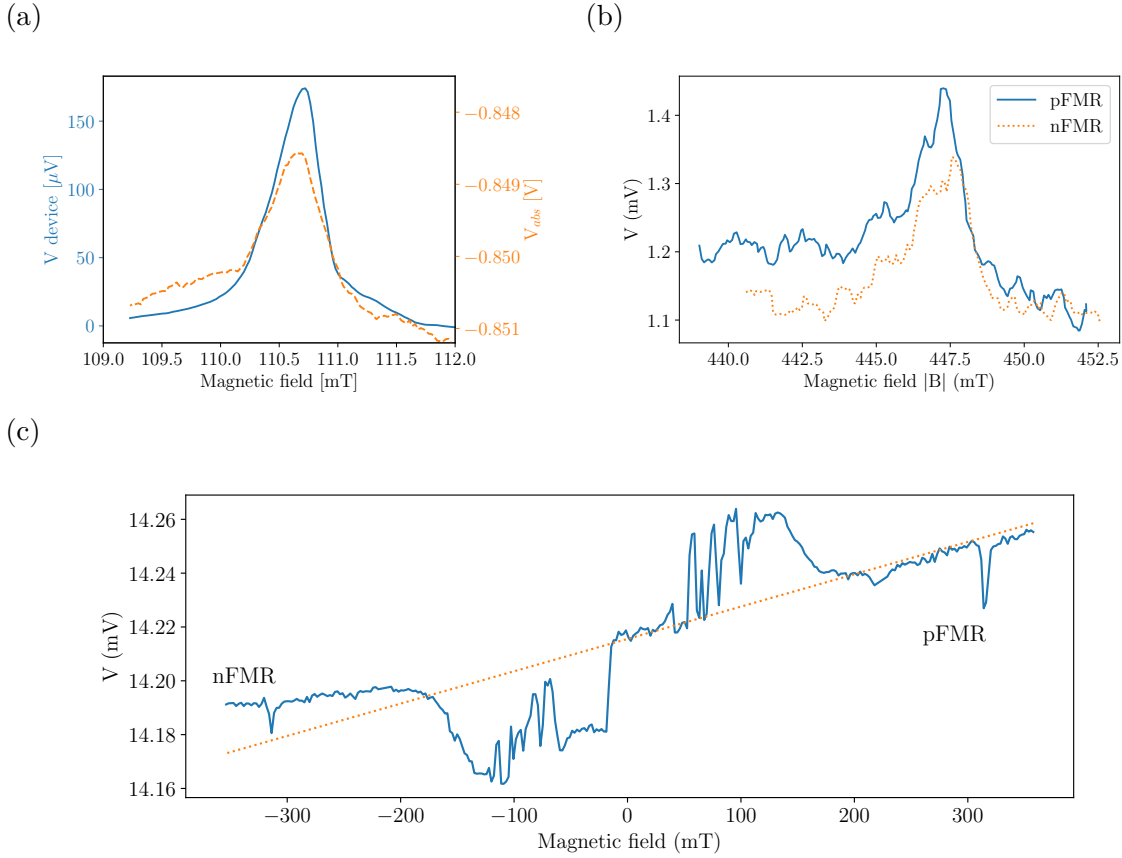


Fig. 7.9 (a) ISHE voltage at FMR in YIG/Pt in the standard configuration with in-plane magnetic field. (b) First harmonic voltage signal in AHE-like measurement configuration with respect to modulation of the driving current of 2.5 mA at 57 Hz in positive (solid blue line) and negative (dotted orange line) out-of-plane magnetic field around FMR for a YIG/Pt sample. (c) Voltage sweep (solid blue line) from negative to positive magnetic field for a YIG/Ru/Pt sample with DC driving current of 10 mA. The orange dotted line serves as a guide to the eye for the contribution from the conventional Hall effect in the metallic layer and FMR peaks at positive and negative field are annotated.

in literature [39]. Therefore, we can conclude that the interface allows efficient spin pumping and platinum serves as a reliable spin-to-charge conversion layer.

The sample was then rotated to out-of-plane magnetic field. A driving current of 2.5 mA was applied along the Hall bar with modulation at 57 Hz. The microwave frequency was set to 8 GHz at a power of 630 mW. The offset voltage perpendicular to the current direction was minimised using a potentiometer.

The first harmonic voltage signal as a function of positive (solid blue line, pFMR) and negative (dotted orange line, nFMR) magnetic field is shown in figure 7.9b. The peak

in voltage is approximately $250 \mu\text{V}$ in magnitude for both pFMR and nFMR and does not depend on the polarity of the magnetic field. This implies that the measured signal at FMR is not due to any spin-related phenomenon.

This experiment is very sensitive towards changes in resistance in the metallic layer as the potentiometer minimises the voltage by accounting for any asymmetry in the geometry and current flow by adjusting the relative resistance. The temperature of YIG increases significantly at FMR inducing a change of resistance in platinum, which might result in the signal we observed. Another potential explanation for the unexpected sign of the voltage signal with respect to the polarity of the magnetic field is that out-of-plane spin polarisation is unfavourable at the YIG/Pt interface due to magnetisation anisotropy of YIG or interfacial effects.

In order to exclude the latter, we have also investigated a sample with an additional Ruthenium (Ru) interlayer. The 2 nm thin layer decouples the platinum detection layer from YIG while transmitting the injected spin. Figure 7.9c shows the voltage signal when a direct current of 10 mA was applied to the Hall bar. In this measurement, the microwave frequency was 4.6 GHz at a power of 1 W. Similarly to before, we can see peaks in voltage at FMR at negative and positive external magnetic field. However, the sign of the peaks does not depend on the polarity of the field. The S-shaped signal around zero field can be ascribed to the tilting of the magnetisation into the plane of the sample (see section 7.2.1), giving rise to a conventional SSE signal due to current induced Joule heating in the Hall bar. In addition to the two features just described, there is also a linear increase in voltage with magnetic field. This is highlighted in figure 7.9c with a dotted orange line and can be ascribed to the conventional Hall effect in the metallic layer.

These results imply that platinum might not be an ideal candidate for observing effects, which require an external driving force to induce ISHE for spin-to-charge conversion. The short spin diffusion length of platinum indicates that spin is randomised very quickly. This short time- and length-scale might not give enough time for the driving force to act efficiently on the spin to create a spin current, which is required for the ISHE. Therefore, in the quest of finding a suitable material system, we have to balance the spin-to-charge conversion efficiency, which we want to be as large as possible, with the spin lifetime, which needs to be long enough for creating a spin current with the driving force in order to create a spin-dependent voltage signal via the ISHE. Indeed, current driven ISHE has been observed recently in Au in a similar

structure [104], implying that a very high spin Hall angle might not be favourable in these experiments.

7.2.4 Conclusions

In summary, several routes towards observing thermal spin-to-charge conversion via the proposed inverse spin Nernst effect have been investigated. The experiments, where the spin polarisation is injected into the detector via spin pumping, showed a signal at FMR, which depends on the orientation of the external magnetic field. However, the linear dependence on the heater current, as opposed to the heater power, as well as the unexpectedly sensitive dependence on the out-of-plane angle of the external magnetic field did not agree with the theoretical predictions of the ISNE.

The signal measured in the optical injection experiments was dominated by the leakage of the heaters due to poor electrical insulation from the substrate. This could be circumvented by choosing a more stable and reliable insulating layer. A suitable candidate would be Parylene, as it covers the substrate uniformly and exhibits excellent electrical insulation properties even in very thin layers [154].

Moreover, we have not been successful in detecting out-of-plane spin polarisation created from spin pumping from YIG in platinum via the electrically modulated ISHE. As this effect has been reported in gold previously in literature, this could imply that a sufficiently long spin diffusion length and time are necessary for observing spin-dependent effects, which rely on accelerating spins with an external force to induce ISHE-like spin detection. The electrically modulated ISHE can serve as a straightforward experiment to find more promising candidates for the detection of the ISNE. Seeing that the electrically modulated ISHE has been demonstrated successfully in GaAs, which is a high charge carrier mobility material with long spin diffusion length and high thermal conductivity, it would be promising to investigate the ISNE directly in GaAs.

Chapter 8

Conclusions and Outlook

The first part of this work mainly focuses on linewidth broadening experiments on organic semiconductors. In chapter 4, we present the procedure, which we have carefully developed, allowing us to quantify spin injection by spin pumping at ferromagnetic resonance from a ferromagnet into an adjacent non-magnetic material by measuring the increase in linewidth of the microwave absorption caused by the change in effective Gilbert damping due to loss of spin angular momentum. We have demonstrated that this method of determining the linewidth broadening is a direct and sensitive measure of spin injection efficiency $g_{eff}^{\uparrow\downarrow}$. The simple device architecture and non-invasive probing make this a clean experiment for unambiguous measurement of spin injection into organic semiconductors.

In chapter 5 and 6, we report the first direct observation of spin injection into organic small molecules and conjugated polymers. Especially for polymers, the extracted spin mixing conductance is surprisingly high and on the same order of magnitude as for the standard reference of permalloy/platinum. This is an auspicious result, as efficient spin injection is of paramount importance for further studies and developments towards technological applications in the field of organic spintronics.

The experimental results indicate the importance of structural properties of the organic semiconductor at the interface to permalloy. This is highlighted in the significant suppression of linewidth broadening in small molecules due to alkyl side-chains.

The main limitation in the choice of materials for the LWB experiments so far was the sensitivity of the Py substrates to processing. Therefore, it is crucial to find a way to circumvent this problem. Recently, it has been shown that a single layer of graphene can act as an efficient barrier against oxidation and protect the underlying material [155]. Py films covered with a graphene protection layer would be a promising candidate for more robust substrates for studying spin injection into a wider range of

OSCs, especially since the spin relaxation in graphene is not expected to reduce the spin injection significantly.

Following on from the LWB measurements on P3EHS, it would be interesting to study the role of SOC on spin injection efficiency and spin diffusion length systematically. In order to ensure comparability of the results, we have compared spin pumping into P3EHT, the analogue to P3HT with branched side-chains, and P3EHS. Indeed, preliminary results (see figure 8.1a) show that the LWB is larger for P3EHS, implying that SOC enhances the spin injection efficiency. However, further structural and energetic characterisation is necessary to link the increase in spin mixing conductance directly to the increase in SOC.

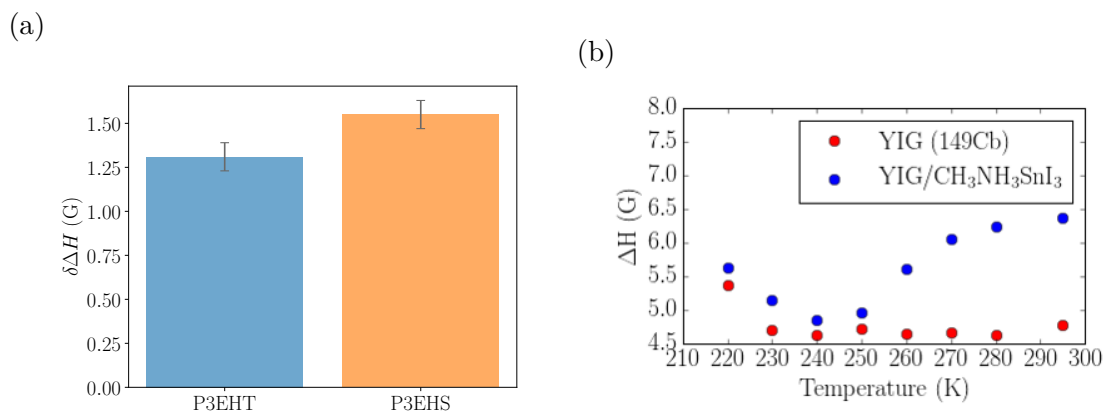


Fig. 8.1 (a) Bar diagram of LWB in Py/P3EHT and Py/P3EHS. (b) Temperature dependence of linewidth of a bare YIG substrate (red) and the same YIG substrate with MASnI₃ (blue).

The experiments exploring the effects of doping on linewidth broadening imply a very sensitive dependence of spin injection efficiency on charge carrier density and hence on spin density at the interface to the ferromagnet within a certain range of doping level. However, quantitative determination of the charge carrier concentration at the interface between permalloy and the OSC films is necessary in future to address this crucial question in the field.

For this, we propose modulation of the charge carrier density by gating. By including a top-gate in the presented device structure for linewidth broadening experiments, the bulk charge carrier concentration can be tuned by applying a gate voltage. Measuring the microwave absorption spectra at ferromagnetic resonance as a function of gate voltage would, therefore, give a deeper and more precisely controlled insight into the dependence of spin injection on charge density.

Another exciting area in organic spintronics, which we have not touched on in this work so far, is the concept of chirality induced spin selectivity (CISS) [156]. This effect was first reported in a self-assembled monolayer of DNA, which is acting as an electron spin filter [157]. Given the high sensitivity, LWB is a promising technique for studying spin polarisation dependent spin injection efficiency in chiral molecules.

Moreover, it would be interesting to study spin injection into different hybrid organic/inorganic material systems, such as perovskites. Metal halide hybrid perovskites have gained considerable attention in recent years and are promising candidates for photovoltaic and spintronic applications [158, 159]. These materials adopt an ABX_3 structure, in which A is commonly given by methylammonium ($CH_3NH_3SnI_3$, MA), B is a metal and X an anion. For the preliminary LWB experiments, we have chosen $MASnI_3$, a widely studied perovskite [160]. Here, we used YIG substrates, as they are less prone to effects of oxydation and processing. We have measured the linewidth of the same YIG substrate before and after deposition of $MASnI_3$ as a function of temperature. The results are shown in figure 8.1b. The change in linewidth is comparably large at room temperature but decreases to a minimum at 240 K. Interestingly, this temperature coincides with the activation temperature of the ionic movement in the perovskite, implying a close link between spin and ions. These preliminary results encourage further investigations into this promising area.

The second part of this work discusses the experiments towards thermal spin injection into organic semiconductors by spin Seebeck effect and thermal spin detection via inverse spin Nernst effect. We demonstrate that we have successfully built a setup for spin Seebeck effect measurements. However, due to limitations set by material properties, we have not been able to detect thermally injected spins in organic semiconductors. The novel technique of high-pressure sputtering might alleviate fabrication of suitable samples.

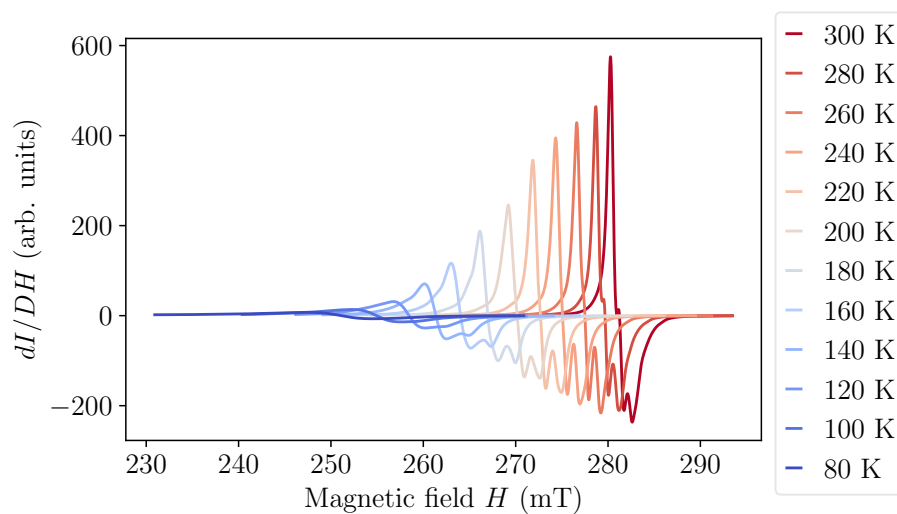
The experiments towards observation of the inverse spin Nernst effect have given valuable insight into the material and device requirements for successful detection of the proposed effect. The results suggest that the short spin diffusion length of platinum impedes efficient acceleration of spins perpendicular to the direction of injection, hindering the detection of an in-plane electrical thermal spin signal. The electrically modulated inverse spin Hall effect experiment can be used to verify a suitable material system, such as GaAs, which is a promising candidate for thermal spin detection for future explorations.

Appendix A

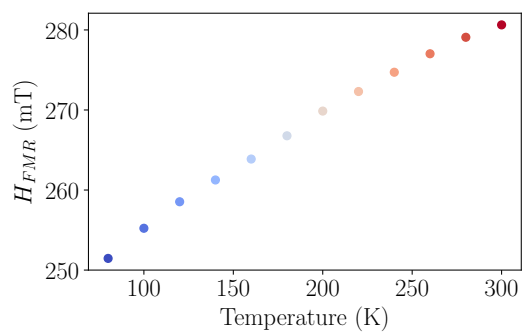
Temperature Dependence of Ferromagnetic Resonance in YIG

We have measured the microwave absorption of a thin film of (38 nm) YIG as a function of temperature. The absorption spectra are shown in figure A.1a on the following page for a temperature range from room temperature down to 80 K. The extracted resonance field H_{FMR} linearly increases with temperature as shown in figure A.1b. Moreover, the linewidth ΔH increases considerably at low temperatures. This effect has previously been observed in literature. However, its origin remains under debate.

(a)



(b)



(c)

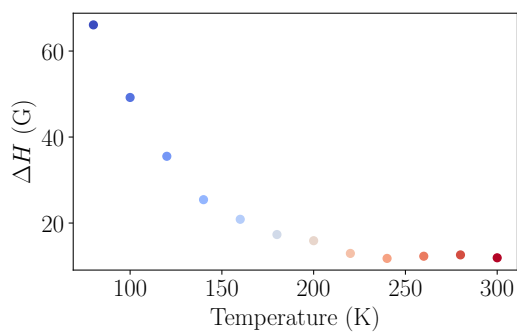


Fig. A.1 (a) FMR spectra of a thin YIG film as a function of temperature. (b) Temperature dependence of the resonance field H_{FMR} and (c) linewidth ΔH .

Appendix B

GIWAXS Analysis of Polymer Films

The details of the crystallographic information extracted from the GIWAXS measurements on P3HT, d-P3HT and IDT-BT are summarised in table B.1 on the following page.

Table B.1 Summary of crystallographic information of three polymers

Crystallographic parameters	P3HT/Si		P3HT/Py		d-P3HT/Py		IDT-BT/Py	
	q (\AA^{-1})		q (\AA^{-1})		q (\AA^{-1})		q (\AA^{-1})	
Lamella stacking	d -spacing (\AA)	0.35837	0.35794	0.35164	0.47699			
	FWHM (\AA^{-1})	17.5	17.6	17.9	26.3			
	Coherence length (\AA)	0.05283	0.05022	0.07105				
	Paracrystallinity, g (%)	214.2	225.3	159.3				
	N_{avg}^{diff}	2.12	2.18	1.84				
$\pi - \pi$ stacking	q (\AA^{-1})	225	213	299				
	d -spacing (\AA)	1.65247	1.65503	1.65203	1.51233			
	FWHM (\AA^{-1})	3.8	3.8	3.8	4.15			
	Coherence length (\AA)	0.08991	0.09289	0.08847	0.46062			
Backbone ordering		127.2	123.1	129.2	24.8			
					0.40043			
					15.7			
					0.04753			
					238.1			

References

- [1] M. Mas, J. Fernández De Guevara Radoselovics, J. Robledo, M. Cardona, M. Lopez Cobo, R. Righi, S. Samoili, and G. De Prato. *An Analysis of ICT R&D in the EU and Beyond*. Tech. rep. 2018, p. 112019. DOI: 10.2760/984658 (cit. on p. 1).
- [2] M. M. Waldrop. “The chips are down for Moore’s law”. In: *Nature* 530.7589 (Feb. 2016), pp. 144–147. DOI: 10.1038/530144a (cit. on p. 1).
- [3] H. Sirringhaus, P. J. Brown, R. H. Friend, M. M. Nielsen, K. Bechgaard, B. M. W. Langeveld-Voss, A. J. H. Spiering, R. A. J. Janssen, E. W. Meijer, P. Herwig, and D. M. de Leeuw. “Two-dimensional charge transport in self-organized, high-mobility conjugated polymers”. In: *Nature* 401.6754 (Oct. 1999), pp. 685–688. DOI: 10.1038/44359 (cit. on pp. 2, 39, 87).
- [4] R. H. Friend, R. W. Gymer, A. B. Holmes, J. H. Burroughes, R. N. Marks, C. Taliani, D. D. C. Bradley, D. A. D. Santos, J. L. Brédas, M. Lögdlund, and W. R. Salaneck. “Electroluminescence in conjugated polymers”. In: *Nature* 397.6715 (Jan. 1999), pp. 121–128. DOI: 10.1038/16393 (cit. on p. 2).
- [5] M. Granström, K. Petritsch, A. C. Arias, A. Lux, M. R. Andersson, and R. H. Friend. “Laminated fabrication of polymeric photovoltaic diodes”. In: *Nature* 395.6699 (Sept. 1998), pp. 257–260. DOI: 10.1038/26183 (cit. on p. 2).
- [6] D. Venkateshvaran, M. Nikolka, A. Sadhanala, V. Lemaury, M. Zelazny, M. Kepa, M. Hurhangee, A. J. Kronemeijer, V. Pecunia, I. Nasrallah, I. Romanov, K. Broch, I. McCulloch, D. Emin, Y. Olivier, J. Cornil, D. Beljonne, and H. Sirringhaus. “Approaching disorder-free transport in high-mobility conjugated polymers”. In: *Nature* 515.7527 (Nov. 2014), pp. 384–388. DOI: 10.1038/nature13854 (cit. on pp. 2, 40).
- [7] G. Szulczewski, S. Sanvito, and M. Coey. “A spin of their own.” In: *Nature materials* 8.9 (2009), pp. 693–695. DOI: 10.1038/nmat2518 (cit. on pp. 2, 3).
- [8] T. L. Francis, Ö. Mermer, G. Veeraraghavan, and M. Wohlgenannt. “Large magnetoresistance at room temperature in semiconducting polymer sandwich devices”. In: *New Journal of Physics* 6 (Dec. 2004), pp. 185–185. DOI: 10.1088/1367-2630/6/1/185 (cit. on p. 2).
- [9] V. Dediu, M. Murgia, F. Maticcotta, C. Taliani, and S. Barbanera. “Room temperature spin polarized injection in organic semiconductor”. In: *Solid State Communications* 122.3-4 (Apr. 2002), pp. 181–184. DOI: 10.1016/S0038-1098(02)00090-X (cit. on p. 2).

- [10] Z. H. Xiong, D. Wu, Z. Valy Vardeny, and J. Shi. “Giant magnetoresistance in organic spin-valves”. In: *Nature* 427.6977 (Feb. 2004), pp. 821–824. DOI: 10.1038/nature02325 (cit. on p. 2).
- [11] M. Grünewald, M. Wahler, F. Schumann, M. Michelfeit, C. Gould, R. Schmidt, F. Würthner, G. Schmidt, and L. W. Molenkamp. “Tunneling anisotropic magnetoresistance in organic spin valves”. In: *Physical Review B* 84.12 (Sept. 2011), p. 125208. DOI: 10.1103/PhysRevB.84.125208 (cit. on p. 2).
- [12] S. Watanabe, K. Ando, K. Kang, S. Mooser, Y. Vaynzof, H. Kurebayashi, E. Saitoh, and H. Sirringhaus. “Polaron spin current transport in organic semiconductors”. In: *Nature Physics* 10.4 (Mar. 2014), pp. 308–313. DOI: 10.1038/nphys2901 (cit. on pp. 3, 4, 40, 49, 69, 93).
- [13] M. Cinchetti, V. A. Dediu, and L. E. Hueso. “Activating the molecular spin-interface”. In: *Nature Materials* 16.5 (Apr. 2017), pp. 507–515. DOI: 10.1038/nmat4902 (cit. on p. 3).
- [14] F. A. Ma’Mari, T. Moorsom, G. Teobaldi, W. Deacon, T. Prokscha, H. Luetkens, S. Lee, G. E. Sterbinsky, D. a. Arena, D. a. MacLaren, M. Flokstra, M. Ali, M. C. Wheeler, G. Burnell, B. J. Hickey, and O. Cespedes. “Beating the Stoner criterion using molecular interfaces”. In: *Nature* 524.7563 (Aug. 2015), pp. 69–73. DOI: 10.1038/nature14621 (cit. on p. 3).
- [15] S.-J. Wang, D. Venkateshvaran, M. R. Mahani, U. Chopra, E. R. McNellis, R. Di Pietro, S. Schott, A. Wittmann, G. Schweicher, M. Cubukcu, K. Kang, R. Carey, T. J. Wagner, J. Siebrecht, D. Wong, I. Jacobs, R. Aboljadayel, A. Ionescu, S. Egorov, S. Mueller, O. Zadvorna, P. Skalski, C. Jellett, M. Little, A. Marks, I. McCulloch, J. Wunderlich, J. Sinova, and H. Sirringhaus. “Long-range and fast exchange-enhanced lateral spin transport in doped conjugated polymers”. In: *Under Review* (2018) (cit. on pp. 4, 85).
- [16] M. Weiler, M. Althammer, M. Schreier, J. Lotze, M. Pernpeintner, S. Meyer, H. Huebl, R. Gross, A. Kamra, J. Xiao, Y. T. Chen, H. Jiao, G. E. W. Bauer, and S. T. B. Goennenwein. “Experimental test of the spin mixing interface conductivity concept”. In: *Physical Review Letters* 111.17 (2013), pp. 1–5. DOI: 10.1103/PhysRevLett.111.176601 (cit. on pp. 5, 20).
- [17] J. Sinova, S. O. Valenzuela, J. Wunderlich, C. H. Back, and T. Jungwirth. “Spin Hall effects”. In: *Reviews of Modern Physics* 87.4 (Oct. 2015), pp. 1213–1260. DOI: 10.1103/RevModPhys.87.1213 (cit. on pp. 5, 29).
- [18] M. Qaid, T. Richter, A. Müller, C. Hauser, and G. Schmidt. “Spin Pumping And Inverse Spin-Hall Effect In PEDOT:PSS”. 2016 (cit. on p. 5).
- [19] S. Meyer, Y.-t. Chen, S. Wimmer, M. Althammer, T. Wimmer, R. Schlitz, S. Geprägs, H. Huebl, D. Ködderitzsch, H. Ebert, G. E. W. Bauer, R. Gross, and S. T. B. Goennenwein. “Observation of the spin Nernst effect”. In: *Nature Materials* 16.10 (Sept. 2017), pp. 977–981. DOI: 10.1038/nmat4964 (cit. on pp. 5, 32, 61, 101).
- [20] J. Clayden, N. Greeves, S. Warren, and P. Wothers. *Organic Chemistry*. Oxford University Press, 2001. DOI: 10.1086/278635 (cit. on pp. 7, 8).

- [21] A. Köhler and H. Bässler. “The Electronic Structure of Organic Semiconductors”. In: *Electronic Processes in Organic Semiconductors*. Weinheim, Germany: Wiley-VCH Verlag GmbH & Co. KGaA, Mar. 2015, pp. 1–86. DOI: 10.1002/9783527685172.ch1 (cit. on p. 8).
- [22] S. Fratini, D. Mayou, and S. Ciuchi. “The Transient Localization Scenario for Charge Transport in Crystalline Organic Materials”. In: *Advanced Functional Materials* 26.14 (Apr. 2016), pp. 2292–2315. DOI: 10.1002/adfm.201502386 (cit. on p. 8).
- [23] T. Sakanoue and H. Sirringhaus. “Band-like temperature dependence of mobility in a solution-processed organic semiconductor”. In: *Nature Materials* 9.9 (Sept. 2010), pp. 736–740. DOI: 10.1038/nmat2825 (cit. on p. 9).
- [24] J.-F. Chang, T. Sakanoue, Y. Olivier, T. Uemura, M.-B. Dufourg-Madec, S. G. Yeates, J. Cornil, J. Takeya, A. Troisi, and H. Sirringhaus. “Hall-Effect Measurements Probing the Degree of Charge-Carrier Delocalization in Solution-Processed Crystalline Molecular Semiconductors”. In: *Physical Review Letters* 107.6 (Aug. 2011), p. 066601. DOI: 10.1103/PhysRevLett.107.066601 (cit. on p. 9).
- [25] S. Fratini, S. Ciuchi, and D. Mayou. “Phenomenological model for charge dynamics and optical response of disordered systems: Application to organic semiconductors”. In: *Physical Review B* 89.23 (June 2014), p. 235201. DOI: 10.1103/PhysRevB.89.235201 (cit. on p. 9).
- [26] S. Illig, A. S. Eggeman, A. Troisi, L. Jiang, C. Warwick, M. Nikolka, G. Schweicher, S. G. Yeates, Y. Henri Geerts, J. E. Anthony, and H. Sirringhaus. “Reducing dynamic disorder in small-molecule organic semiconductors by suppressing large-amplitude thermal motions”. In: *Nature Communications* 7 (Feb. 2016), p. 10736. DOI: 10.1038/ncomms10736 (cit. on pp. 9, 39).
- [27] P. J. Brown, H. Sirringhaus, M. Harrison, M. Shkunov, and R. H. Friend. “Optical spectroscopy of field-induced charge in self-organized high mobility poly(3-hexylthiophene)”. In: *Physical Review B* 63.12 (Mar. 2001), p. 125204. DOI: 10.1103/PhysRevB.63.125204 (cit. on p. 9).
- [28] M. C. J. M. Vissenberg and M. Matters. “Theory of the field-effect mobility in amorphous organic transistors”. In: *Physical Review B* 57.20 (May 1998), pp. 12964–12967. DOI: 10.1103/PhysRevB.57.12964 (cit. on p. 9).
- [29] J. J. Brondijk, W. S. C. Roelofs, S. G. J. Mathijssen, A. Shehu, T. Cramer, F. Biscarini, P. W. M. Blom, and D. M. de Leeuw. “Two-Dimensional Charge Transport in Disordered Organic Semiconductors”. In: *Physical Review Letters* 109.5 (Aug. 2012), p. 056601. DOI: 10.1103/PhysRevLett.109.056601 (cit. on p. 9).
- [30] R. P. Fornari, P. W. M. Blom, and A. Troisi. “How Many Parameters Actually Affect the Mobility of Conjugated Polymers?” In: *Physical Review Letters* 118.8 (Feb. 2017), p. 086601. DOI: 10.1103/PhysRevLett.118.086601 (cit. on p. 9).
- [31] F. Pulizzi. “Spintronics”. In: *Nature Materials* 11.5 (May 2012), pp. 367–367. DOI: 10.1038/nmat3327 (cit. on p. 10).
- [32] P. A. M. (A. M. Dirac. *The principles of quantum mechanics*. Clarendon Press, 1981, p. 314 (cit. on p. 10).

- [33] J. D. Jackson. *Classical electrodynamics*. Wiley, 2012, p. 808 (cit. on p. 10).
- [34] A. Altland and B. (D. Simons. *Condensed matter field theory*. Cambridge University Press, 2006, p. 624 (cit. on pp. 11, 12).
- [35] L. Landau. “On the theory of the dispersion of magnetic permeability in ferromagnetic bodies”. In: *Collected Papers of L.D. Landau*. Elsevier, Jan. 1965, pp. 101–114. DOI: 10.1016/B978-0-08-010586-4.50023-7 (cit. on p. 13).
- [36] T. Gilbert. “Classics in Magnetism A Phenomenological Theory of Damping in Ferromagnetic Materials”. In: *IEEE Transactions on Magnetics* 40.6 (Nov. 2004), pp. 3443–3449. DOI: 10.1109/TMAG.2004.836740 (cit. on p. 13).
- [37] L. Frangou. *PhD Thesis: Spin injection, transmission and detection in antiferromagnets*. 2017 (cit. on p. 14).
- [38] K. Ando, Y. Kajiwara, S. Takahashi, S. Maekawa, K. Takemoto, M. Takatsu, and E. Saitoh. “Angular dependence of inverse spin–Hall effect induced by spin pumping investigated in a NiFe/Pt thin film”. In: *Physical Review B* 78.1 (July 2008), p. 014413. DOI: 10.1103/PhysRevB.78.014413 (cit. on p. 14).
- [39] E. Saitoh, M. Ueda, H. Miyajima, and G. Tatara. “Conversion of spin current into charge current at room temperature: Inverse spin-Hall effect”. In: *Applied Physics Letters* 88.18 (May 2006), p. 182509. DOI: 10.1063/1.2199473 (cit. on pp. 15, 31, 108).
- [40] T. D. Rossing. “Resonance Linewidth and Anisotropy Variation in Thin Films”. In: *Journal of Applied Physics* 34.4 (Apr. 1963), pp. 995–995. DOI: 10.1063/1.1729582 (cit. on p. 15).
- [41] M. B. Jungfleisch, A. V. Chumak, A. Kehlberger, V. Lauer, D. H. Kim, M. C. Onbasli, C. A. Ross, M. Kläui, and B. Hillebrands. “Thickness and power dependence of the spin-pumping effect in YIG/Pt heterostructures measured by the inverse spin Hall effect”. In: *Physical Review B* 91.13 (Apr. 2015), p. 134407. DOI: 10.1103/PhysRevB.91.134407 (cit. on pp. 15, 20).
- [42] S. Mizukami, Y. Ando, and T. Miyazaki. “The Study on Ferromagnetic Resonance Linewidth for NM/80NiFe/NM (NM=Cu, Ta, Pd and Pt) Films”. In: *Japanese Journal of Applied Physics* 40.Part 1, No. 2A (Feb. 2001), pp. 580–585. DOI: 10.1143/JJAP.40.580 (cit. on pp. 15, 20).
- [43] B. Heinrich, G. Woltersdorf, R. Urban, and E. Simanek. “Role of dynamic exchange coupling in magnetic relaxations of metallic multilayer films”. In: *Journal of Applied Physics* 93.10 (May 2003), pp. 7545–7550. DOI: 10.1063/1.1543852 (cit. on p. 15).
- [44] X. Joyeux, T. Devolder, J.-V. Kim, Y. Gomez de la Torre, S. Eimer, and C. Chappert. “Configuration and temperature dependence of magnetic damping in spin valves”. In: *Journal of Applied Physics* 110.6 (Sept. 2011), p. 063915. DOI: 10.1063/1.3638055 (cit. on p. 15).
- [45] B. Heinrich, D. Fraitová, and V. Kamberský. “The Influence of s-d Exchange on Relaxation of Magnons in Metals”. In: *physica status solidi (b)* 23.2 (1967), pp. 501–507. DOI: 10.1002/pssb.19670230209 (cit. on p. 16).

- [46] S. Zhang and Z. Li. “Roles of Nonequilibrium Conduction Electrons on the Magnetization Dynamics of Ferromagnets”. In: *Physical Review Letters* 93.12 (Sept. 2004), p. 127204. DOI: 10.1103/PhysRevLett.93.127204 (cit. on p. 16).
- [47] V. Kamberský. “On the Landau–Lifshitz relaxation in ferromagnetic metals”. In: *Canadian Journal of Physics* 48.24 (Dec. 1970), pp. 2906–2911. DOI: 10.1139/p70-361 (cit. on p. 16).
- [48] H. Suhl. “Theory of the magnetic damping constant”. In: *IEEE Transactions on Magnetics* 34.4 (July 1998), pp. 1834–1838. DOI: 10.1109/20.706720 (cit. on p. 16).
- [49] J. A. C. Bland and B. Heinrich. *Ultrathin Magnetic Structures III : Fundamentals of Nanomagnetism*. Springer-Verlag Berlin Heidelberg, 2005 (cit. on p. 16).
- [50] R. A. Lukaszew. *Handbook of nanomagnetism : applications and tools*. CRC Press, 2015 (cit. on p. 16).
- [51] M. J. Hurben and C. E. Patton. “Theory of two magnon scattering microwave relaxation and ferromagnetic resonance linewidth in magnetic thin films”. In: *Journal of Applied Physics* 83.8 (Apr. 1998), pp. 4344–4365. DOI: 10.1063/1.367194 (cit. on p. 16).
- [52] R. Arias and D. L. Mills. “Extrinsic contributions to the ferromagnetic resonance response of ultrathin films”. In: *Physical Review B* 60.10 (Sept. 1999), pp. 7395–7409. DOI: 10.1103/PhysRevB.60.7395 (cit. on p. 17).
- [53] K. Lenz, H. Wende, W. Kuch, K. Baberschke, K. Nagy, and A. Jánossy. “Two-magnon scattering and viscous Gilbert damping in ultrathin ferromagnets”. In: *Physical Review B* 73.14 (Apr. 2006), p. 144424. DOI: 10.1103/PhysRevB.73.144424 (cit. on p. 17).
- [54] J. H. Van Vleck and R. Orbach. “Ferrimagnetic Resonance of Dilute Rare-Earth Doped Iron Garnets”. In: *Physical Review Letters* 11.2 (July 1963), pp. 65–67. DOI: 10.1103/PhysRevLett.11.65 (cit. on p. 17).
- [55] J. Dubowik, F. Stobiecki, I. Gościańska, Y. P. Lee, A. Paetzold, and K. Röhl. “Temperature dependence of ferromagnetic resonance in permalloy/NiO exchange-biased films”. In: *The European Physical Journal B* 45.2 (May 2005), pp. 283–288. DOI: 10.1140/epjb/e2005-00174-7 (cit. on p. 17).
- [56] G. Woltersdorf, M. Kiessling, G. Meyer, J.-U. Thiele, and C. H. Back. “Damping by Slow Relaxing Rare Earth Impurities in NiFe”. In: *Physical Review Letters* 102.25 (June 2009), p. 257602. DOI: 10.1103/PhysRevLett.102.257602 (cit. on p. 17).
- [57] S. P. Dash, S. Sharma, J. C. Le Breton, J. Peiro, H. Jaffrès, J.-M. George, A. Lemaître, and R. Jansen. “Spin precession and inverted Hanle effect in a semiconductor near a finite-roughness ferromagnetic interface”. In: *Physical Review B* 84.5 (Aug. 2011), p. 054410. DOI: 10.1103/PhysRevB.84.054410 (cit. on p. 17).
- [58] V. Flovik, F. Macià, A. D. Kent, and E. Wahlström. “Eddy current interactions in a ferromagnet-normal metal bilayer structure, and its impact on ferromagnetic resonance lineshapes”. In: *Journal of Applied Physics* 117.14 (Apr. 2015), p. 143902. DOI: 10.1063/1.4917285 (cit. on p. 17).

- [59] Y. Tserkovnyak, A. Brataas, and G. E. W. Bauer. “Spin pumping and magnetization dynamics in metallic multilayers”. In: *Physical Review B* 66.22 (Dec. 2002), p. 224403. DOI: 10.1103/PhysRevB.66.224403 (cit. on pp. 18, 92).
- [60] A. Brataas, Y. Tserkovnyak, G. E. W. Bauer, and B. I. Halperin. “Spin battery operated by ferromagnetic resonance”. In: *Physical Review B* 66.6 (Aug. 2002), p. 060404. DOI: 10.1103/PhysRevB.66.060404 (cit. on pp. 18, 19).
- [61] Y. Tserkovnyak, A. Brataas, G. E. W. Bauer, and B. I. Halperin. “Nonlocal magnetization dynamics in ferromagnetic heterostructures”. In: *Reviews of Modern Physics* 77.4 (Dec. 2005), pp. 1375–1421. DOI: 10.1103/RevModPhys.77.1375 (cit. on p. 18).
- [62] Y. Tserkovnyak, A. Brataas, and G. E. W. Bauer. “Enhanced Gilbert Damping in Thin Ferromagnetic Films”. In: *Physical Review Letters* 88.11 (Feb. 2002), p. 117601. DOI: 10.1103/PhysRevLett.88.117601 (cit. on pp. 18, 92).
- [63] P. W. Brouwer. “Scattering approach to parametric pumping”. In: *Physical Review B* 58.16 (Oct. 1998), R10135–R10138. DOI: 10.1103/PhysRevB.58.R10135 (cit. on p. 18).
- [64] S. Schott. *PhD Thesis: Spin Dynamics in Organic Semiconductors*. 2018 (cit. on p. 19).
- [65] F. D. Czeschka, L. Dreher, M. S. Brandt, M. Weiler, M. Althammer, I.-M. Imort, G. Reiss, A. Thomas, W. Schoch, W. Limmer, H. Huebl, R. Gross, and S. T. B. Goennenwein. “Scaling Behavior of the Spin Pumping Effect in Ferromagnet-Platinum Bilayers”. In: *Physical Review Letters* 107.4 (July 2011), p. 046601. DOI: 10.1103/PhysRevLett.107.046601 (cit. on pp. 20, 34, 70).
- [66] P. Deorani and H. Yang. “Role of spin mixing conductance in spin pumping: Enhancement of spin pumping efficiency in Ta/Cu/Py structures”. In: *Applied Physics Letters* 103.23 (Dec. 2013), p. 232408. DOI: 10.1063/1.4839475 (cit. on p. 20).
- [67] A. Ruiz-Calaforra, T. Brächer, V. Lauer, P. Pirro, B. Heinz, M. Geilen, A. V. Chumak, A. Conca, B. Leven, and B. Hillebrands. “The role of the non-magnetic material in spin pumping and magnetization dynamics in NiFe and CoFeB multilayer systems”. In: *Journal of Applied Physics* 117.16 (Apr. 2015), p. 163901. DOI: 10.1063/1.4918909 (cit. on p. 20).
- [68] M. Haertinger, C. H. Back, J. Lotze, M. Weiler, S. Geprägs, H. Huebl, S. T. B. Goennenwein, and G. Woltersdorf. “Spin pumping in YIG/Pt bilayers as a function of layer thickness”. In: *Physical Review B* 92.5 (Aug. 2015), p. 054437. DOI: 10.1103/PhysRevB.92.054437 (cit. on p. 20).
- [69] S. M. Rezende, R. L. Rodríguez-Suárez, R. O. Cunha, a. R. Rodrigues, F. L. a. Machado, G. a. Fonseca Guerra, J. C. Lopez Ortiz, and a. Azevedo. “Magnon spin-current theory for the longitudinal spin-Seebeck effect”. In: *Physical Review B - Condensed Matter and Materials Physics* 89.1 (2014), pp. 1–10. DOI: 10.1103/PhysRevB.89.014416 (cit. on pp. 20, 21).
- [70] J. Xiao, G. E. W. Bauer, K. C. Uchida, E. Saitoh, and S. Maekawa. “Theory of magnon-driven spin Seebeck effect”. In: *Physical Review B - Condensed Matter and Materials Physics* 81.21 (2010), pp. 1–8. DOI: 10.1103/PhysRevB.81.214418 (cit. on pp. 20, 22).

- [71] K. Uchida, T. Ota, H. Adachi, J. Xiao, T. Nonaka, Y. Kajiwara, G. E. W. Bauer, S. Maekawa, and E. Saitoh. “Thermal spin pumping and magnon-phonon-mediated spin-Seebeck effect”. In: *Journal of Applied Physics* 111.10 (2012), p. 103903. DOI: 10.1063/1.4716012 (cit. on pp. 21, 22, 51, 52).
- [72] H. Adachi, K.-i. Uchida, E. Saitoh, and S. Maekawa. “Theory of the spin Seebeck effect.” In: *Reports on progress in physics. Physical Society (Great Britain)* 76.3 (Mar. 2013), p. 036501. DOI: 10.1088/0034-4885/76/3/036501 (cit. on p. 23).
- [73] K. Uchida, S. Takahashi, K. Harii, J. Ieda, W. Koshibae, K. Ando, S. Maekawa, and E. Saitoh. “Observation of the spin Seebeck effect.” In: *Nature* 455.7214 (Oct. 2008), pp. 778–81. DOI: 10.1038/nature07321 (cit. on p. 23).
- [74] K.-i. Uchida, H. Adachi, T. Ota, H. Nakayama, S. Maekawa, and E. Saitoh. “Observation of longitudinal spin-Seebeck effect in magnetic insulators”. In: *Applied Physics Letters* 97.17 (2010), p. 172505. DOI: 10.1063/1.3507386 (cit. on p. 23).
- [75] M. Schreier, G. E. W. Bauer, V. Vasyuchka, J. Flipse, K.-i. Uchida, V. Lauer, A. Chumak, A. Serga, S. Daimon, T. Kikkawa, B. J. V. Wees, B. Hillebrands, R. Gross, and S. T. B. Goennenwein. “Sign of inverse spin Hall voltages generated by ferromagnetic resonance and temperature gradients in yttrium iron garnet | platinum bilayers”. In: *Journal of Physics D: Applied Physics* 48.2 (Apr. 2015), pp. 1–5. DOI: 10.1088/0022-3727/48/2/025001 (cit. on pp. 23, 51).
- [76] S. Y. Huang, X. Fan, D. Qu, Y. P. Chen, W. G. Wang, J. Wu, T. Y. Chen, J. Q. Xiao, and C. L. Chien. “Transport Magnetic Proximity Effects in Platinum”. In: *Physical Review Letters* 109.10 (Sept. 2012), p. 107204. DOI: 10.1103/PhysRevLett.109.107204 (cit. on pp. 23, 97).
- [77] H. Jin, S. R. Boona, Z. Yang, R. C. Myers, and J. P. Heremans. “The effect of the magnon dispersion on the longitudinal spin Seebeck effect in yttrium iron garnets (YIG)”. In: *Arxiv preprint* (2014), pp. 1–26 (cit. on p. 23).
- [78] F. (Meier and B. P. Zakharchenya. *Optical orientation*. North-Holland, 1984, p. 523 (cit. on pp. 23, 24).
- [79] S. Maekawa, S. O. Valenzuela, E. Saitoh, and T. Kimura. *Spin Current*. Ed. by S. Maekawa, S. O. Valenzuela, E. Saitoh, and T. Kimura. Vol. 1. Oxford University Press, Dec. 2017. DOI: 10.1093/oso/9780198787075.001.0001 (cit. on pp. 23, 24, 30).
- [80] S. Adachi. *GaAs and Related Materials*. WORLD SCIENTIFIC, Oct. 1994, p. 696. DOI: 10.1142/2508 (cit. on p. 23).
- [81] D. T. Pierce and F. Meier. “Photoemission of spin-polarized electrons from GaAs”. In: *Physical Review B* 13.12 (June 1976), pp. 5484–5500. DOI: 10.1103/PhysRevB.13.5484 (cit. on p. 24).
- [82] I. Zutic, J. Fabian, and S. D. Sarma. “Spintronics : Fundamentals and applications”. In: *Reviews of Modern Physics* 76. April (2004) (cit. on p. 24).
- [83] F. Bloch. “Nuclear Induction”. In: *Physical Review* 70.7-8 (Oct. 1946), pp. 460–474. DOI: 10.1103/PhysRev.70.460 (cit. on p. 25).
- [84] H. C. Torrey. “Bloch Equations with Diffusion Terms”. In: *Physical Review* 104.3 (Nov. 1956), pp. 563–565. DOI: 10.1103/PhysRev.104.563 (cit. on p. 25).

- [85] K. M. Alam and S. Pramanik. “Spin Transport in Organic Semiconductors: A Brief Overview of the First Eight Years”. In: *Nano-Semiconductors, Devices and Technology*. CRC Press, May 2010. DOI: 10.1201/B11388 (cit. on pp. 26, 27).
- [86] R. J. Elliott. “Theory of the Effect of Spin-Orbit Coupling on Magnetic Resonance in Some Semiconductors”. In: *Physical Review* 96.2 (Oct. 1954), pp. 266–279. DOI: 10.1103/PhysRev.96.266 (cit. on p. 25).
- [87] Y. Yafet. “g Factors and Spin-Lattice Relaxation of Conduction Electrons”. In: *Solid State Physics*. Vol. 14. Academic Press, Jan. 1963, pp. 1–98. DOI: 10.1016/S0081-1947(08)60259-3 (cit. on p. 25).
- [88] M. I. D’yakonov and V. I. Perel’. “Spin relaxation of conduction electrons in noncentrosymmetric semiconductors”. In: *Sov. Phys. Solid State* 13 (1972), pp. 3023–3026. DOI: 10.1016/0038-1098(76)90531-7 (cit. on p. 26).
- [89] G. L. Bir, A. G. Aronov, and G. E. Pikus. “Spin relaxation of electrons due to scattering by holes”. In: *Zh. Eksp. Teor. Fiz* 69 (1975), pp. 1382–1397 (cit. on p. 27).
- [90] M. I. D’yakonov and V. I. Perel’. “Optical orientation in a system of electrons and lattice nuclei in semiconductors. Theory”. In: *Zh. Eksp. Teor. Fiz.* 65 (1973), pp. 362–375 (cit. on p. 27).
- [91] P. A. Bobbert, W. Wagemans, F. W. A. van Oost, B. Koopmans, and M. Wohlgenannt. “Theory for Spin Diffusion in Disordered Organic Semiconductors”. In: *Physical Review Letters* 102.15 (Apr. 2009), p. 156604. DOI: 10.1103/PhysRevLett.102.156604 (cit. on p. 27).
- [92] N. J. Harmon and M. E. Flatté. “Distinguishing Spin Relaxation Mechanisms in Organic Semiconductors”. In: *Physical Review Letters* 110.17 (Apr. 2013), p. 176602. DOI: 10.1103/PhysRevLett.110.176602 (cit. on p. 27).
- [93] N. J. Harmon and M. E. Flatté. “Spin relaxation in materials lacking coherent charge transport”. In: *Physical Review B* 90.11 (Sept. 2014), p. 115203. DOI: 10.1103/PhysRevB.90.115203 (cit. on p. 27).
- [94] Z. G. Yu, F. Ding, and H. Wang. “Hyperfine interaction and its effects on spin dynamics in organic solids”. In: *Physical Review B* 87.20 (May 2013), p. 205446. DOI: 10.1103/PhysRevB.87.205446 (cit. on p. 27).
- [95] Z. G. Yu. “Microscopic theory of electron spin relaxation in N@ C60”. In: *Physical Review B* 77.20 (May 2008), p. 205439. DOI: 10.1103/PhysRevB.77.205439 (cit. on p. 28).
- [96] Z. G. Yu. “Spin-orbit coupling and its effects in organic solids”. In: *Physical Review B* 85.11 (Mar. 2012), p. 115201. DOI: 10.1103/PhysRevB.85.115201 (cit. on p. 28).
- [97] C. L. Chien and C. R. Westgate. *The Hall Effect and Its Applications*. Ed. by C. L. Chien and C. R. Westgate. Boston, MA: Springer US, 1980. DOI: 10.1007/978-1-4757-1367-1 (cit. on p. 29).
- [98] N. Nagaosa, J. Sinova, S. Onoda, A. H. MacDonald, and N. P. Ong. “Anomalous Hall effect”. In: *Reviews of Modern Physics* 82.2 (May 2010), pp. 1539–1592. DOI: 10.1103/RevModPhys.82.1539 (cit. on p. 29).

- [99] C.-Z. Chang and M. Li. “Quantum anomalous Hall effect in time-reversal-symmetry breaking topological insulators”. In: *Journal of Physics: Condensed Matter* 28.12 (Mar. 2016), p. 123002. DOI: 10.1088/0953-8984/28/12/123002 (cit. on p. 29).
- [100] M. I. D’yakonov, V. I. Perel’, A. F. Ioffe, M. I. Dyakonov, and V. I. Perel. “Possibility of Orienting Electron Spins with Current”. In: *JETP Letters* 13 (1971), p. 467 (cit. on p. 29).
- [101] J. E. Hirsch. “Spin Hall Effect”. In: *Physical Review Letters* 83.9 (Aug. 1999), pp. 1834–1837. DOI: 10.1103/PhysRevLett.83.1834 (cit. on p. 29).
- [102] Y. K. Kato, R. C. Myers, A. C. Gossard, and D. D. Awschalom. “Observation of the Spin Hall Effect in Semiconductors”. In: *Science* 306.5703 (Dec. 2004), pp. 1910–1913. DOI: 10.1126/science.1105514 (cit. on p. 30).
- [103] J. Wunderlich, B. Kaestner, J. Sinova, and T. Jungwirth. “Experimental Observation of the Spin-Hall Effect in a Two-Dimensional Spin-Orbit Coupled Semiconductor System”. In: *Physical Review Letters* 94.4 (Feb. 2005), pp. 1–4. DOI: 10.1103/PhysRevLett.94.047204 (cit. on p. 30).
- [104] D. Hou, Z. Qiu, R. Iguchi, K. Sato, E. K. Vehstedt, K. Uchida, G. E. W. Bauer, and E. Saitoh. “Observation of temperature-gradient-induced magnetization”. In: *Nature Communications* 7 (July 2016), p. 12265. DOI: 10.1038/ncomms12265 (cit. on pp. 31, 32, 107, 110).
- [105] K. Olejník, J. Wunderlich, A. C. Irvine, R. P. Campion, V. P. Amin, J. Sinova, and T. Jungwirth. “Detection of Electrically Modulated Inverse Spin Hall Effect in an Fe/GaAs Microdevice”. In: *Physical Review Letters* 109.7 (Aug. 2012), p. 076601. DOI: 10.1103/PhysRevLett.109.076601 (cit. on pp. 31, 107).
- [106] O. Song. “No TitleMagnetoelastic Coupling in Thin Films”. PhD thesis. Massachusetts Institute of Technology, 1994 (cit. on p. 34).
- [107] M. J. Kang, I. Doi, H. Mori, E. Miyazaki, K. Takimiya, M. Ikeda, and H. Kuwabara. “Alkylated Dinaphtho[2,3-b:2,3-f]Thieno[3,2-b]Thiophenes (Cn-DNTTs): Organic Semiconductors for High-Performance Thin-Film Transistors”. In: *Advanced Materials* 23.10 (Mar. 2011), pp. 1222–1225. DOI: 10.1002/adma.201001283 (cit. on p. 35).
- [108] M. J. Kang, E. Miyazaki, I. Osaka, K. Takimiya, and A. Nakao. “Diphenyl Derivatives of Dinaphtho[2,3-b:2,3-f]thieno[3,2-b]thiophene: Organic Semiconductors for Thermally Stable Thin-Film Transistors”. In: *ACS Applied Materials & Interfaces* 5.7 (Apr. 2013), pp. 2331–2336. DOI: 10.1021/am3026163 (cit. on p. 35).
- [109] M. Alkan and I. Yavuz. “Intrinsic charge-mobility in benzothieno[3,2-b][1]benzothiophene (BTBT) organic semiconductors is enhanced with long alkyl side-chains”. In: *Physical Chemistry Chemical Physics* 20.23 (2018), pp. 15970–15979. DOI: 10.1039/C8CP01640B (cit. on p. 36).
- [110] H. Minemawari, M. Tanaka, S. Tsuzuki, S. Inoue, T. Yamada, R. Kumai, Y. Shimoi, and T. Hasegawa. “Enhanced Layered-Herringbone Packing due to Long Alkyl Chain Substitution in Solution-Processable Organic Semiconductors”. In: *Chemistry of Materials* 29.3 (Feb. 2017), pp. 1245–1254. DOI: 10.1021/acs.chemmater.6b04628 (cit. on p. 36).

- [111] K. Kamada, K. Ohta, A. Shimizu, T. Kubo, R. Kishi, H. Takahashi, E. Botek, B. Champagne, and M. Nakano. “Singlet Diradical Character from Experiment”. In: *The Journal of Physical Chemistry Letters* 1.6 (Mar. 2010), pp. 937–940. DOI: 10.1021/jz100155s (cit. on p. 37).
- [112] J. Ma, J. Liu, M. Baumgarten, Y. Fu, Y.-Z. Tan, K. S. Schellhammer, F. Ortman, G. Cuniberti, H. Komber, R. Berger, K. Müllen, and X. Feng. “A Stable Saddle-Shaped Polycyclic Hydrocarbon with an Open-Shell Singlet Ground State”. In: *Angewandte Chemie International Edition* 56.12 (Mar. 2017), pp. 3280–3284. DOI: 10.1002/anie.201611689 (cit. on p. 38).
- [113] D. T. Chase, A. G. Fix, S. J. Kang, B. D. Rose, C. D. Weber, Y. Zhong, L. N. Zakharov, M. C. Lonergan, C. Nuckolls, and M. M. Haley. “6,12-Diarylindeno[1,2-b]fluorenes: Syntheses, Photophysics, and Ambipolar OFETs”. In: *Journal of the American Chemical Society* 134.25 (June 2012), pp. 10349–10352. DOI: 10.1021/ja303402p (cit. on p. 38).
- [114] S. Ito, T. Minami, and M. Nakano. “Diradical Character Based Design for Singlet Fission of Condensed-Ring Systems with $4n\pi$ Electrons”. In: *The Journal of Physical Chemistry C* 116.37 (Sept. 2012), pp. 19729–19736. DOI: 10.1021/jp3072684 (cit. on p. 38).
- [115] G. E. Rudebusch, J. L. Zafra, K. Jorner, K. Fukuda, J. L. Marshall, I. Arrechea-Marcos, G. L. Espejo, R. Ponce Ortiz, C. J. Gómez-García, L. N. Zakharov, M. Nakano, H. Ottosson, J. Casado, and M. M. Haley. “Diindeno-fusion of an anthracene as a design strategy for stable organic biradicals”. In: *Nature Chemistry* 8.8 (Aug. 2016), pp. 753–759. DOI: 10.1038/nchem.2518 (cit. on p. 38).
- [116] J. Wade, F. Steiner, D. Niedzialek, D. T. James, Y. Jung, D.-J. Yun, D. D. C. Bradley, J. Nelson, and J.-S. Kim. “Charge mobility anisotropy of functionalized pentacenes in organic field effect transistors fabricated by solution processing”. In: *J. Mater. Chem. C* 2.47 (Oct. 2014), pp. 10110–10115. DOI: 10.1039/C4TC01353K (cit. on p. 39).
- [117] M. Heeney, W. Zhang, D. J. Crouch, M. L. Chabinye, S. Gordeyev, R. Hamilton, S. J. Higgins, I. McCulloch, P. J. Skabara, D. Sparrowe, and S. Tierney. “Regioregular poly(3-hexyl)selenophene: a low band gap organic hole transporting polymer”. In: *Chemical Communications* 47 (2007), p. 5061. DOI: 10.1039/b712398a (cit. on pp. 39, 88).
- [118] H. Hintz, H. Peisert, H.-J. Egelhaaf, and T. Chassé. “Reversible and Irreversible Light-Induced p-Doping of P3HT by Oxygen Studied by Photoelectron Spectroscopy (XPS/UPS)”. In: *The Journal of Physical Chemistry C* 115.27 (July 2011), pp. 13373–13376. DOI: 10.1021/jp2032737 (cit. on pp. 39, 88).
- [119] C. Wang, L. H. Jimison, L. Goris, I. McCulloch, M. Heeney, A. Ziegler, and A. Salleo. “Microstructural Origin of High Mobility in High-Performance Poly(thieno-thiophene) Thin-Film Transistors”. In: *Advanced Materials* 22.6 (Feb. 2010), pp. 697–701. DOI: 10.1002/adma.200902303 (cit. on p. 40).

- [120] D. J. Harkin, K. Broch, M. Schreck, H. Ceymann, A. Stoy, C.-K. Yong, M. Nikolka, I. McCulloch, N. Stingelin, C. Lambert, and H. Sirringhaus. “Decoupling Charge Transport and Electroluminescence in a High Mobility Polymer Semiconductor”. In: *Advanced Materials* 28.30 (Aug. 2016), pp. 6378–6385. DOI: 10.1002/adma.201600851 (cit. on p. 40).
- [121] P. Pingel and D. Neher. “Comprehensive picture of p-type doping of P3HT with the molecular acceptor F4TCNQ”. In: *Physical Review B* 87.11 (Mar. 2013), p. 115209. DOI: 10.1103/PhysRevB.87.115209 (cit. on p. 41).
- [122] R. Fujimoto, Y. Yamashita, S. Kumagai, J. Tsurumi, A. Hinderhofer, K. Broch, F. Schreiber, S. Watanabe, and J. Takeya. “Molecular doping in organic semiconductors: fully solution-processed, vacuum-free doping with metal–organic complexes in an orthogonal solvent”. In: *Journal of Materials Chemistry C* 5.46 (2017), pp. 12023–12030. DOI: 10.1039/C7TC03905K (cit. on p. 41).
- [123] H. L. Wang, C. H. Du, Y. Pu, R. Adur, P. C. Hammel, and F. Y. Yang. “Scaling of Spin Hall Angle in 3d, 4d, and 5d Metals from YIG/Metal Spin Pumping”. In: *Physical Review Letters* 112.19 (May 2014), p. 197201. DOI: 10.1103/PhysRevLett.112.197201 (cit. on p. 42).
- [124] K. Ando and E. Saitoh. “Inverse spin-Hall effect in palladium at room temperature”. In: *Journal of Applied Physics* 108.11 (Dec. 2010), p. 113925. DOI: 10.1063/1.3517131 (cit. on p. 42).
- [125] C. Du, H. Wang, F. Yang, and P. C. Hammel. “Systematic variation of spin-orbit coupling with d-orbital filling: Large inverse spin Hall effect in 3d transition metals”. In: *Physical Review B* 90.14 (Oct. 2014), p. 140407. DOI: 10.1103/PhysRevB.90.140407 (cit. on pp. 42, 98).
- [126] G. Gbabode, N. Dumont, F. Quist, G. Schweicher, A. Moser, P. Viville, R. Lazzaroni, and Y. H. Geerts. “Substrate-Induced Crystal Plastic Phase of a Discotic Liquid Crystal”. In: *Advanced Materials* 24.5 (Feb. 2012), pp. 658–662. DOI: 10.1002/adma.201103739 (cit. on p. 46).
- [127] N. Vlietstra, J. Shan, B. J. van Wees, M. Isasa, F. Casanova, and J. Ben Youssef. “Simultaneous detection of the spin-Hall magnetoresistance and the spin-Seebeck effect in platinum and tantalum on yttrium iron garnet”. In: *Physical Review B* 90.17 (Nov. 2014), p. 174436. DOI: 10.1103/PhysRevB.90.174436 (cit. on pp. 48, 51, 52).
- [128] Z. Qiu, K. Ando, K. Uchida, Y. Kajiwara, R. Takahashi, H. Nakayama, T. An, Y. Fujikawa, and E. Saitoh. “Spin mixing conductance at a well-controlled platinum/yttrium iron garnet interface”. In: *Applied Physics Letters* 103.9 (2013), p. 092404. DOI: 10.1063/1.4819460 (cit. on p. 48).
- [129] M. B. Jungfleisch, V. Lauer, R. Neb, a. V. Chumak, and B. Hillebrands. “Improvement of the yttrium iron garnet/platinum interface for spin pumping-based applications”. In: *Applied Physics Letters* 103.2 (2013), pp. 2011–2015. DOI: 10.1063/1.4813315 (cit. on p. 48).
- [130] A. Aqeel, I. J. Vera-Marun, B. J. van Wees, and T. T. M. Palstra. “Surface sensitivity of the spin Seebeck effect”. In: *Journal of Applied Physics* 116.15 (2014), p. 153705. DOI: 10.1063/1.4897933 (cit. on p. 49).

- [131] K. Kang. *PhD Thesis: Pure spin current and charge transport in conjugated polymers*. 2017 (cit. on pp. 49, 59).
- [132] M. Schreier, N. Roschewsky, E. Dobler, S. Meyer, H. Huebl, R. Gross, and S. T. B. Goennenwein. “Current heating induced spin Seebeck effect”. In: *Applied Physics Letters* 103.24 (2013), p. 242404. DOI: 10.1063/1.4839395 (cit. on pp. 51, 52).
- [133] M. Weiler, M. Althammer, F. D. Czeschka, H. Huebl, M. S. Wagner, M. Opel, I. M. Imort, G. Reiss, A. Thomas, R. Gross, and S. T. B. Goennenwein. “Local charge and spin currents in magnetothermal landscapes”. In: *Physical Review Letters* 108.March (2012), pp. 1–5. DOI: 10.1103/PhysRevLett.108.106602 (cit. on pp. 51, 52).
- [134] M. Cubukcu, D. Venkateshvaran, A. Wittmann, S.-J. Wang, R. Di Pietro, S. Auffret, L. Vila, J. Wunderlich, and H. Sirringhaus. “Electrical nucleation and detection of single 360° homochiral Néel domain walls measured using the anomalous Nernst effect”. In: *Applied Physics Letters* 112.26 (June 2018), p. 262409. DOI: 10.1063/1.5040321 (cit. on p. 56).
- [135] G. Matthaei, L. Young, and E. Jones. “Microwave filters, impedance-matching networks, and coupling structures”. In: *Artech House* (1980). DOI: 10.1109/PROC.1965.4048 (cit. on p. 60).
- [136] S. Schott, E. R. McNellis, C. B. Nielsen, H.-Y. Chen, S. Watanabe, H. Tanaka, I. McCulloch, K. Takimiya, J. Sinova, and H. Sirringhaus. “Tuning the effective spin-orbit coupling in molecular semiconductors”. In: *Nature Communications* 8 (May 2017), p. 15200. DOI: 10.1038/ncomms15200 (cit. on p. 78).
- [137] K. Kang, S. Watanabe, K. Broch, A. Sepe, A. Brown, I. Nasrallah, M. Nikolka, Z. Fei, M. Heeney, D. Matsumoto, K. Marumoto, H. Tanaka, S.-i. Kuroda, and H. Sirringhaus. “2D coherent charge transport in highly ordered conducting polymers doped by solid state diffusion”. In: *Nature Materials* 15.8 (Aug. 2016), pp. 896–902. DOI: 10.1038/nmat4634 (cit. on p. 81).
- [138] M. Shao, J. Keum, J. Chen, Y. He, W. Chen, J. F. Browning, J. Jakowski, B. G. Sumpter, I. N. Ivanov, Y.-Z. Ma, C. M. Rouleau, S. C. Smith, D. B. Geohegan, K. Hong, and K. Xiao. “The isotopic effects of deuteration on optoelectronic properties of conducting polymers”. In: *Nature Communications* 5.1 (Dec. 2014), p. 3180. DOI: 10.1038/ncomms4180 (cit. on p. 89).
- [139] N. Shida, D. Okazaki, T. Kurioka, H. Nishiyama, D. S. Seferos, I. Tomita, and S. Inagi. “Anodic Chlorination of Selenophene-Containing Polymers: Reaction Efficiency and Selective Reaction of Single Segment in Rod-Rod Diblockcopolymer”. In: *ChemElectroChem* 4.8 (Aug. 2017), pp. 1824–1827. DOI: 10.1002/celec.201700205 (cit. on p. 90).
- [140] J. Hollinger and D. S. Seferos. “Morphology Control of Selenophene-Thiophene Block Copolymers through Side Chain Engineering”. In: *Macromolecules* 47.15 (Aug. 2014), pp. 5002–5009. DOI: 10.1021/ma501231d (cit. on p. 90).
- [141] S.-J. Wang. *PhD Thesis: Spin Pumping in Polymers*. 2018 (cit. on p. 93).
- [142] A. Kiriwara, K.-i. Uchida, Y. Kajiwara, M. Ishida, Y. Nakamura, T. Manako, E. Saitoh, and S. Yorozu. “Spin-current-driven thermoelectric coating”. In: *Nature Materials* 11.8 (June 2012), pp. 686–689. DOI: 10.1038/nmat3360 (cit. on p. 96).

- [143] T. Kikkawa, K. Uchida, Y. Shiomi, Z. Qiu, D. Hou, D. Tian, H. Nakayama, X.-F. Jin, and E. Saitoh. “Longitudinal Spin Seebeck Effect Free from the Proximity Nernst Effect”. In: *Physical Review Letters* 110.6 (Feb. 2013), pp. 1–5. DOI: 10.1103/PhysRevLett.110.067207 (cit. on p. 97).
- [144] T. Kikkawa, K. Uchida, S. Daimon, Y. Shiomi, H. Adachi, Z. Qiu, D. Hou, X.-F. Jin, S. Maekawa, and E. Saitoh. “Separation of longitudinal spin Seebeck effect from anomalous Nernst effect: Determination of origin of transverse thermoelectric voltage in metal/insulator junctions”. In: *Physical Review B* 88.21 (Dec. 2013), p. 214403. DOI: 10.1103/PhysRevB.88.214403 (cit. on p. 97).
- [145] K. Uchida, M. Ishida, T. Kikkawa, A. Kirihara, T. Murakami, and E. Saitoh. “Longitudinal spin Seebeck effect: from fundamentals to applications (2014 J. Phys.: Condens. Matter 26 343202)”. In: *Journal of Physics: Condensed Matter* 26.38 (Sept. 2014), p. 389601. DOI: 10.1088/0953-8984/26/38/389601 (cit. on pp. 98, 100).
- [146] V. Vlaminck, J. E. Pearson, S. D. Bader, and a. Hoffmann. “Dependence of spin-pumping spin Hall effect measurements on layer thicknesses and stacking order”. In: *Physical Review B* 88.6 (Aug. 2013), p. 064414. DOI: 10.1103/PhysRevB.88.064414 (cit. on p. 98).
- [147] M. Morota, Y. Niimi, K. Ohnishi, D. H. Wei, T. Tanaka, H. Kontani, T. Kimura, and Y. Otani. “Indication of intrinsic spin Hall effect in 4d and 5d transition metals”. In: *Physical Review B - Condensed Matter and Materials Physics* 83.17 (2011), pp. 1–5. DOI: 10.1103/PhysRevB.83.174405 (cit. on p. 98).
- [148] J. M. D. Coey and M. Venkatesan. “Half-metallic ferromagnetism: Example of CrO₂ (invited)”. In: *Journal of Applied Physics* 91.10 (2002), p. 8345. DOI: 10.1063/1.1447879 (cit. on p. 99).
- [149] Y. Harima, H. Okazaki, Y. Kunugi, K. Yamashita, H. Ishii, and K. Seki. “Formation of Schottky barriers at interfaces between metals and molecular semiconductors of p- and n-type conductances”. In: *Applied Physics Letters* 69.8 (1996), pp. 1059–1061. DOI: 10.1063/1.116930 (cit. on p. 99).
- [150] T. K. Djidjou, D. A. Bevans, S. Li, and A. Rogachev. “Observation of Shot Noise in Phosphorescent Organic Light-Emitting Diodes”. In: *IEEE Transactions on Electron Devices* 61.9 (2014), pp. 3252–3257. DOI: 10.1109/TED.2014.2339856 (cit. on p. 99).
- [151] O. Wid, J. Bauer, A. Müller, O. Breitenstein, S. S. P. Parkin, and G. Schmidt. “Investigation of the unidirectional spin heat conveyer effect in a 200nm thin Yttrium Iron Garnet film”. In: *Nature Publishing Group* February (2016), p. 8. DOI: 10.1038/srep28233 (cit. on p. 104).
- [152] L. J. Cornelissen, J. Liu, R. A. Duine, J. B. Youssef, and B. J. van Wees. “Long-distance transport of magnon spin information in a magnetic insulator at room temperature”. In: *Nature Physics* 11.12 (Dec. 2015), pp. 1022–1026. DOI: 10.1038/nphys3465 (cit. on p. 104).

- [153] J. Shan, L. J. Cornelissen, N. Vlietstra, J. Ben Youssef, T. Kuschel, R. A. Duine, and B. J. van Wees. “Influence of yttrium iron garnet thickness and heater opacity on the nonlocal transport of electrically and thermally excited magnons”. In: *Physical Review B* 94.17 (Nov. 2016), p. 174437. DOI: 10.1103/PhysRevB.94.174437 (cit. on p. 104).
- [154] G. E. Loeb, M. J. Bak, M. Salcman, and E. M. Schmidt. “Parylene as a Chronically Stable, Reproducible Microelectrode Insulator”. In: *IEEE Transactions on Biomedical Engineering* BME-24.2 (Mar. 1977), pp. 121–128. DOI: 10.1109/TBME.1977.326115 (cit. on p. 110).
- [155] J. S. Bunch, S. S. Verbridge, J. S. Alden, A. M. van der Zande, J. M. Parpia, H. G. Craighead, and P. L. McEuen. “Impermeable Atomic Membranes from Graphene Sheets”. In: *Nano Letters* 8.8 (Aug. 2008), pp. 2458–2462. DOI: 10.1021/nl801457b (cit. on p. 111).
- [156] R. Naaman and D. H. Waldeck. “Chiral-Induced Spin Selectivity Effect”. In: *The Journal of Physical Chemistry Letters* 3.16 (Aug. 2012), pp. 2178–2187. DOI: 10.1021/jz300793y (cit. on p. 113).
- [157] B. Gohler, V. Hamelbeck, T. Z. Markus, M. Kettner, G. F. Hanne, Z. Vager, R. Naaman, and H. Zacharias. “Spin Selectivity in Electron Transmission Through Self-Assembled Monolayers of Double-Stranded DNA”. In: *Science* 331.6019 (Feb. 2011), pp. 894–897. DOI: 10.1126/science.1199339 (cit. on p. 113).
- [158] W. Li, Z. Wang, F. Deschler, S. Gao, R. H. Friend, and A. K. Cheetham. “Chemically diverse and multifunctional hybrid organic–inorganic perovskites”. In: *Nature Reviews Materials* 2.3 (Mar. 2017), p. 16099. DOI: 10.1038/natrevmats.2016.99 (cit. on p. 113).
- [159] D. Sun, C. Zhang, M. Kavand, K. J. van Schooten, H. Malissa, M. Groesbeck, R. McLaughlin, C. Boehme, and Z. V. Vardeny. “Spintronics of Organometal Trihalide Perovskites”. In: 3 (Aug. 2016) (cit. on p. 113).
- [160] T. Fujihara, S. Terakawa, T. Matsushima, C. Qin, M. Yahiro, and C. Adachi. “Fabrication of high coverage MASnI₃ perovskite films for stable, planar heterojunction solar cells”. In: *Journal of Materials Chemistry C* 5.5 (2017), pp. 1121–1127. DOI: 10.1039/C6TC05069G (cit. on p. 113).